MECHANICS OF FLOWING GRANULAR MEDIA

Thesis by

James Charles Pearce

In Partial Fulfillment of the Requirements

For the Degree of

Doctor of Philosophy

California Institute of Technology

Pasadena, California

1975

(Submitted October 10, 1975)

ACKNOWLEDGMENTS

ABSTRACT

The flow of a frictional, cohesive solid through plane conver-ging channels with Coulomb friction acting along the channel walls is investigated. The constitutive postulates used in the development of the solution are discussed and the solution is compared with those obtained by earlier investigators. Velocity profiles, mass flow rates, and mean stress distributions along the channel walls predicted by the analysis are compared with experimental results. The solution correctly predicts the trend of the mass flow rate as a function of the channel opening angle as well as the magnitude of the mass flow rate in terms of the flow parameters. The solution also gives an accurate measure of the mean stress acting along the channel walls.

The problem of predicting the size of the cavity formed below a cylinder in the transverse flow of a frictional, cohesionless material is investigated experimentally. A correlation which gives the lower separation angle as a function of the flow parameters is determined.

Finally, the temperature distribution in the wake of a heated cylinder in the transverse flow of a granular material is investigated experimentally and spanwise temperature profiles are given as a function of downstream location.

The information gained from the experimental investigation is intended to be of use in the design of heat exchanger equipment for granular media.

LIST OF FIGURES

TABLE OF CONTENTS

- 1 -

CHAPTER I — INTRODUCTION

The general problem to which this investigation is directed concerns the flow of a frictional, cohesive solid through plane converging channels with Coulomb friction acting along the channel walls. Because of the large quantities of frictional, cohesive solids, such as coal, ores, grains, sand, etc., transported each year, this problem has received considerable theoretical and experimental attention in the past.

Solutions have been presented [87, 92, 99][*] for the flow of a perfectly plastic, non-frictional material but these solutions have only limited applicability since the shear stresses acting along the walls are assumed constant. A more useful solution for the flow of a frictional, cohesive solid, obeying the Jenike-Shield yield condition [4], was presented by Jenike [42]. The inertial terms in the equations of motion were neglected, however, and as discussed in detail later, a unique velocity field could not be found. Sullivan [95] derived an exact solution for a frictional, cohesionless material, obeying the Jenike-Shield yield condition, for the particular case of radial gravity and frictionless channel walls. A unique velocity field was determined but the corresponding mass flow rate was larger than that observed in

---

[*]Numbers in brackets indicate References listed at the end of the paper.

practice as a result of the assumption of frictionless channel walls.

Chapter 2 deals specifically with the problem of the flow of a frictional cohesive solid through converging channels. A brief description of the constitutive relations used in the development of the proposed solution is given in Chapter 2, Section 1. The implications of assuming that the flow of a frictional material is perfectly plastic are discussed. The complete system of governing equations and appropriate boundary conditions for the problem are also given.

The solutions developed by Jenike [42] and Sullivan [95] are discussed in Chapter 2, Section 2. An approximate solution to the complete system of equations and boundary conditions is developed in Chapter 2, Section 3. Mass flow rates and velocity profiles given by the approximate solution for the flow of a frictional, cohesionless material through plane converging channels with Coulomb friction along the walls are compared with experimental results [14, 15, 95]. In addition to predicting the correct trend of the mass flow rate channel opening angle, the solution also gives a very accurate prediction of the magnitude of the mass flow rate in terms of the flow parameters. The mean stress acting along the channel walls given by the approximate solution is compared with experimental results [20, 38, 51]. Again the approximate solution gives an accurate prediction of the trend and magnitude of the experimental data.

Chapters 3 and 4 deal specifically with problems related to the design of a granular heat exchanger in a contact-dominated flow. Heat transfer in a contact-dominated flow where the pore fluid is transported, passively, along with the particles has wide industrial application where it is desired to heat, cool, or dry such materials. This problem differs greatly from the more familiar fluidized bed problem in which the solid particles are suspended in the fluid. Only a few investigators in the past have considered heat transfer in contact-dominated flows.

The principal studies include a theoretical and experimental investigation by Brinn, et al, [105] of the heat transfer to granular material flowing through long heated tubes, and experimental work conducted by Kurochkin [107] and Donskov [106, 127] concerned with the heat transfer from blunt bodies in the transverse flow of quartz sand. Even though in each of these studies the characteristic length associated with the heated solid surface was large compared to the mean particle size, contradictory results as to the effect of particle size were observed. Brinn, et al, [105] found that for purposes of heat transfer the material could be treated as a one-component continuum independent of particle size, while Kurochkin [107] and Donskov [106, 127] found that average heat transfer increased for decreasing particle size.

In a recent study by Sullivan [95], concerned with the heat transfer from a flat plate in uniform flow, it was found that the influence of a particle size is determined by the size of a single parameter which may be interpreted physically as the ratio of the thermal boundary layer thickness to mean particle size. For large values of this parameter, as in the case of a granular flow through a long heated tube, the distance over which a non-negligible temperature changes may occur is large compared to the particle size and hence the material may be treated as a continuum. However, for granular flow over heated blunt bodies this parameter is generally not large and thus non-negligible temperature changes may occur over distances comparable to the mean particle size.

Qualitative observations of the flow around a cylinder have revealed that a stagnant region ahead of the cylinder and a cavity below the cylinder are formed. Surface temperature measurements taken by Kurochkin [107] for a heated cylinder show that substantially higher temperatures are reached in the stagnant and cavity regions than in the area of the cylinder that is "washed" by the flowing material. Since the stagnant and cavity regions affect the velocity distribution around the cylinder as well as reduce the "effective" heat transfer surface, the average heat transfer from a cylinder must be a function of the size of these regions.

It has been shown that for flow over a blunt body the size of the stagnant and cavity regions may be greatly reduced by choosing a more streamlined tube shape [107]. For example, for the flow of a granular material over a double wedge, shown in Fig. 3.1.1, both the stagnant and cavity regions are absent. However, the added difficulty and cost in manufacturing non-circular heat exchanger tubes usually makes this approach unattractive.

Chapter 3 deals specifically with the problem of predicting the size of the cavity formed below a cylindrical section in transverse flow as a function of the flow parameters.

This information will be helpful in the design of granular heat exchangers. Furthermore, any knowledge of the size and location of the stagnant and cavity regions will be of importance for further analytical studies on the velocity and temperature fields around a cylinder.

An additional experimental study was undertaken to determine the size and character of the wake of a heated cylinder as a function of the flow parameters. A complete description of this study as well as the experimental results is given in Chapter 4.

CHAPTER II — GRAVITY FLOW OF A FRICTIONAL, COHESIVE SOLID

1. Constitutive Relations

The problem to be considered is that of the gravity flow of a frictional cohesive solid through plane converging channels with Coulomb friction acting along the channel walls. A principal part of the problem concerns the particular constitutive postulates which relate the stresses and strain rates. The purpose of this section is to discuss the constitutive postulates for the continuous failure of a Coulomb solid proposed by Jenike and Shield [4], and then to develop the necessary system of equations that follow from these postulates for the above mentioned problem. In Section 2 of this Chapter two approximate solutions which were obtained by earlier investigators for this particular system of equations will be presented. In Section 3 a perturbation solution which was obtained in the course of the present study will be developed. The results are in good agreement with reported mass flow rates and mean stress data for frictional materials.

The plane strain plastic flow of a non-work hardening isotropic material in which the yield stress is independent of mean pressure is described by the system of equations given by Hill [92]. The equations of equilibrium, neglecting body forces for this discussion, are

$$\frac{\partial \sigma_x}{\partial x} + \frac{\partial \tau_{xy}}{\partial y} = 0 \qquad \text{in the } x \text{ direction} \qquad (2.1.1)$$

and

$$\frac{\partial \tau_{xy}}{\partial x} + \frac{\partial \sigma_y}{\partial y} = 0 \qquad \text{in the y direction} \qquad (2.1.2)$$

where compressive stresses are taken as positive. The condition of isotropy which requires the axes of principal stress and strain rate to coincide is just

$$\frac{\sigma_x - \sigma_y}{\tau_{xy}} = \frac{\mathring{\epsilon}_x - \mathring{\epsilon}_y}{\mathring{\epsilon}_{xy}}$$

where $\mathring{\epsilon}_x = \frac{\partial u}{\partial x}$; $\mathring{\epsilon}_y = \frac{\partial v}{\partial y}$; $\mathring{\epsilon}_{xy} = \frac{1}{2}\left(\frac{\partial u}{\partial y} + \frac{\partial v}{\partial x}\right)$ are the components of the strain rate tensor given here in terms of the Eulerian velocity components u and v in the +x and +y directions, respectively. It has been assumed that the material is rigid-plastic, i.e., a material that is rigid below the yield point, so that the total strain rate is equal to the plastic strain rate. The yield condition, for the case where the yield stress does not depend on mean pressure, is

$$\left(\frac{\sigma_x - \sigma_y}{2}\right)^2 + \tau_{xy}^2 = K^2 \qquad (2.1.4)$$

where

$$K = \frac{Y}{\sqrt{3}} \qquad \text{for the Von Mises yield criterion and}$$

$$K = \frac{Y}{2} \qquad \text{for the Tresca yield criterion and Y is}$$

the yield stress in simple compression. The condition of zero volume change is expressed by a continuity equation, namely,

$$\frac{\partial u}{\partial x} + \frac{\partial v}{\partial y} = 0 \quad . \qquad (2.1.5)$$

In principal stress space with the principal stresses σ_1, σ_2, σ_3

(where $\sigma_1 > \sigma_2 > \sigma_3$) along the three coordinate axes,[*] the yield condition Eq. 2.1.4 describes a regular hexagonal prism for the Tresca yield criterion and a right circular cylinder for the yield criterion of Von Mises. Both the prism of Tresca and the cylinder of Von Mises are centered about the hydrostatic axis $\sigma_1 = \sigma_2 = \sigma_3$. By the principle of normality the incremental strain rate vector for plastic flow must be normal to the yield surface. Hence it becomes obvious that for the above condition the strain rate vector must be perpendicular to the hydrostatic axis and, from isotropy, perpendicular to the axis $\dot{\epsilon}_1 = \dot{\epsilon}_2 = \dot{\epsilon}_3$ so that plastic flow involves zero volume change.

The above ideas developed for the flow of a perfectly plastic material, that is, a non-work hardening material, may be extended to a Coulomb solid by replacing the yield condition, Eq. 2.1.4, by a Mohr-Coulomb relation, for example,

$$\sqrt{\left(\frac{\sigma_x - \sigma_y}{2}\right)^2 + \tau_{xy}^2} = \left(\frac{\sigma_x + \sigma_y}{2}\right)\sin\varphi_1 - c\,\cos\varphi_1 \qquad (2.1.6)$$

where φ_1 is the angle of internal friction and c is the cohesion. Drucker [98] suggested that the Coulomb condition could be interpreted as either a generalization of the Tresca or Von Mises yield criteria in three dimensions. Such generalization transforms the yield surface described by the prism of Tresca into a regular hexagonal pyramid or the cylinder of Von Mises into a cone both centered along the hydrostatic axis with

---

[*]Since the material is assumed isotropic the principal axes of stress and strain rate coincide so that the axes of principal strain rate $\dot{\epsilon}_1$, $\dot{\epsilon}_2$, and $\dot{\epsilon}_3$ may be superimposed, for the purpose of discussion, along the σ_1, σ_2, σ_3 axes.

vertex at $\sigma_1 = \sigma_2 = \sigma_3 = -c \cot\varphi_1$.

The material is assumed to be isotropic so that in the principal stress diagram the axes of principal strain rate may still be taken to lie along the axes of principal stress. The principle of normality, requiring the incremental plastic strain rate vector to be perpendicular to the yield surface, still applies. It is seen that now however the incremental strain rate vector is no longer perpendicular to the hydrostatic axis and hence no longer perpendicular to the axis $\dot{\epsilon}_1 = \dot{\epsilon}_2 = \dot{\epsilon}_3$. Therefore, plastic flow must be accompanied by continuous volume change.

Since continuous dilation during plastic straining of a Coulomb solid is not observed in practice, the treatment of a Coulomb solid as a perfectly plastic material satisfying a generalized Tresca or Von Mises criterion does not seem adequate. As a possible means of rectifying the problem of continuous volume change, Drucker, Henkel, and Gibson [3] suggested the treatment of a Coulomb solid as a work-hardening material.

Drucker, Henkel, and Gibson [3] made the following physical observations. First, for a drained-triaxial test of a fully saturated clay, yielding occurs for a stress state on the hydrostatic axis. This suggests that the generalization of either the Tresca or Von Mises criteria for a non-work hardening material, which would extend without bound along the hydrostatic axis, to describe the yielding of a Coulomb material is perhaps inaccurate. Second, for a material loaded to point A, on the pressure-volume change curve in Fig. 2.1.1, and then unloaded to point R, reloading, to first order will follow the unloading path back to point A and then continue along the initial

pressure-volume change curve. This too suggests a work-hardening type behavior.

Considering [3], but extending the interpretation to three dimensions, the Coulomb condition may be interpreted as a generalization of the Tresca or Von Mises criterion in three dimensions but "cut-off" at some point along the hydrostatic axis, by as yet an unspecified surface,[*] so that the instantaneous yield surface is described by either a pyramid or cone, respectively, but of finite size. An increase in mean stress will result in an expansion of the yield surface about, and along, the hydrostatic axis.

The vertex of the yield surface will lie along the hydrostatic axis at the point $\sigma_1 = \sigma_2 = \sigma_3 = -c \cot\varphi_1$. Since the cohesion, c, is a function of mean pressure, the above expansion will result in a motion of the vertex of the yield surface along the hydrostatic axis in the tension direction.

From the theory of plasticity, the plastic strain increment vector is normal to the yield surface at a smooth point, i.e., a regular point, and within the directions of adjacent normals at a corner, i.e., a singular point. Thus, if the point on the yield surface describing the stress state at failure is located on the end cap of the yield surface, plastic flow could be accompanied by a decrease, increase, or no change in volume depending on the direction of the strain increment

_____

[*]From the theory of plasticity, the fundamental definition of work hardening and perfect plasticity lead to the requirement that all yield surfaces must be convex. Hence, while the yield surface used to "cut-off" the prism of Tresca of the cone of Von Mises is unspecified, it must be convex.

vector relative to the hydrostatic axis.

Shield [5] presents an alternate interpretation for the shape of the yield surface, as opposed to the pyramid of Tresca or the cone of Von Mises, describing the Coulomb condition in three dimensions. Shield describes the yield surface as a right irregular hexagonal pyramid centered about the hydrostatic axis, again with the vertex of the yield surface located on the hydrostatic axis at $\sigma_1 = \sigma_2 = \sigma_3 = - c \cot\varphi_1$.

Jenike and Shield [4] adopt the work hardening postulate of Drucker, et al, [3], however, the yield surface is taken to be the pyramid of Shield [5] closed off with a base defined by the plane $\sigma = \frac{1}{3}(\sigma_1 + \sigma_2 + \sigma_3)$ as shown in Fig. 2.1.2.

Yielding can only occur for a stress point on the yield surface. For a point, D, on the pyramid base (Fig. 2.1.3), the strain rate vector, from the principle of normality, is perpendicular to the base resulting in an expansion of the yield pyramid giving an increase in mean stress and a decrease in volume.[*] Jenike refers to this process as consolidation. Since cohesion, c, is a function of mean stress, the expansion of the pyramid also involves a motion of the pyramid vertex along the hydrostatic axis in the tension direction. At a point, F, on the pyramid face, the strain rate vector, again normal to the surface, represents a shrinking of the yield pyramid accompanied by a decrease in mean stress and an increase in volume. Jenike refers to this process as expansion. For a point, E, a unique direction for strain rate vector is not defined but from the theory of plasticity the vector must

---

[*]For a fixed mass, a volume decrease represents merely an increase in bulk density.

lie between adjacent normals to the pyramid face and pyramid base. Depending on the particular orientation of the strain rate vector for a stress state at, E, yielding may be accompanied by an increase, decrease or no change in volume.

Again following Jenike and Shield [4], the open pyramid in two dimensions is represented by the Coulomb yield condition, namely,

$$-\frac{1}{2}(\sigma_x + \sigma_y) + \frac{1}{\sin\varphi_1}\sqrt{\left(\frac{\sigma_x - \sigma_y}{2}\right)^2 + \tau_{xy}^2} - c\cot\varphi_1 = 0 \quad . \qquad (2.1.7)$$

If it is assumed that the cohesion term may be written

$$c \cot\varphi_1 = a(\sigma + \sigma_0)$$

where "a" and σ_0 are material constants, then the open pyramid may be closed off by writing

$$+\frac{1}{2}(\sigma_x + \sigma_y) + \frac{1}{\sin\varphi_1}\sqrt{\left(\frac{\sigma_x - \sigma_y}{2}\right)^2 + \tau_{xy}^2} - a(\sigma + \sigma_0) = 0 \qquad (2.1.8)$$

and

$$\left(\frac{\sigma_x + \sigma_y}{2}\right) \leq \sigma$$

where the inequality provides for the closing base of the pyramid.

The yield surface in (σ, τ) coordinates and the corresponding Mohr diagram are given in Fig. 2.1.4. The line A-E corresponds to the faces of the pyramid, and the Mohr circle through the point E to

the edge of the base of the pyramid. The angle between the τ axis and the vector, $\dot{\underline{\epsilon}}$, is φ_v. Jenike and Shield [4] determine expressions for upper and lower bounds for φ_v depending on whether the flow involves expansion or consolidation, respectively. The above expressions for the upper and lower bounds involve material properties relating to the variation of density with mean pressure. These properties were measured by Jenike, Elsey, and Woolley [30] to give the following bounds on φ_v, namely,

$$-2°14' < \varphi_v < 2°4'$$

for plane strain. Therefore, it seems justified to assume that $\varphi_v \sim 0$ so that the continuous failure of a Coulomb solid involves no volume change. This condition may be expressed by an equation of continuity, namely,

$$\dot{\epsilon}_1 + \dot{\epsilon}_2 = 0 \quad . \tag{2.1.9}$$

It is seen that the velocity field characteristics are located at $\pm(\pi/2)/2$ from the axis of major principal strain rate, and since the material is isotropic, $\pm(\pi/2)/2$ from the axis of major principal stress.

During the expansion stage of flow, the stresses are continuously at one of the points E, and the stresses are represented by a Mohr circle through points E. Substituting the following expressions

$$\frac{\sigma_x + \sigma_y}{2} = 0$$

$$\sin \varphi = (1+a)\sin\varphi_1$$

$$C \cot\varphi = \frac{a\sigma_0}{1+a}$$

into the yield condition given by Eq. 2.1.8, the effective yield condition

is obtained,

$$-\sigma + \frac{1}{\sin\varphi}\sqrt{\left(\frac{\sigma_x - \sigma_y}{2}\right)^2 + \tau_{xy}^2} \; -C\cot\varphi = 0$$

where φ is the effective angle of friction. Following Jenike [42] the material constant σ_0 may be taken equal to zero so that the above yield condition reduces to

$$\sqrt{\left(\frac{\sigma_x - \sigma_y}{2}\right)^2 + \tau_{xy}^2} - \left(\frac{\sigma_x + \sigma_y}{2}\right)\sin\varphi = 0 \quad . \qquad (2.1.10)$$

It should be noted that the effective friction angle φ coincides with the material internal friction angle, φ_1, for a cohesionless material.

It is seen that the characteristics associated with the stress field are located at $\pm 1/2(\pi/2 - \varphi)$ to the direction of major principal stress.

Thus the constitutive postulates proposed for the continuous failure of a frictional cohesive solid due to Jenike and Shield [4] and expressed in cylindrical coordinates as used in the present analysis may be summarized as follows. The condition of zero volume change is expressed by a continuity equation

$$\frac{\partial u}{\partial r} + \frac{u}{r} + \frac{1}{r}\frac{\partial v}{\partial \theta} = 0 \qquad (2.1.11)$$

where it has been assumed that the material is rigid-plastic so that the plastic strain rates are equal to the total strain rates. Since the material is isotropic the axes of principal stress and strain rate coincide which may be expressed by the equation of isotropy,

$$\frac{\sigma_r - \sigma_\theta}{\tau_{r\theta}} = \frac{\frac{\partial u}{\partial r} - \frac{1}{r}\frac{\partial v}{\partial \theta} - \frac{u}{r}}{\frac{1}{2}\left(\frac{\partial v}{\partial r} - \frac{v}{r} + \frac{1}{r}\frac{\partial u}{\partial \theta}\right)} \quad . \tag{2.1.12}$$

Finally, the yield condition is given by the effective yield condition derived earlier, namely,

$$\sqrt{\left(\frac{\sigma_r - \sigma_\theta}{2}\right)^2 + \tau_{r\theta}^2} = \left(\frac{\sigma_r + \sigma_\theta}{2}\right)\sin\varphi \tag{2.1.13}$$

where φ is the effective friction angle.

The equations of motion for the geometry of Fig. 2.3.1 given by Sullivan [95] are

$$\frac{\partial \sigma_r}{\partial r} + \frac{1}{r}\frac{\partial \tau_{r\theta}}{\partial \theta} + \frac{1}{r}(\sigma_r - \sigma_\theta) + \rho g \cos\theta = -\rho\left(u\frac{\partial u}{\partial r} + \frac{v}{r}\frac{\partial u}{\partial \theta} - \frac{v^2}{r}\right) \tag{2.1.14}$$

$$\frac{\partial \tau_{r\theta}}{\partial r} + \frac{1}{r}\frac{\partial \sigma_\theta}{\partial \theta} + \frac{2}{r}\tau_{r\theta} - \rho g \sin\theta = -\rho\left(u\frac{\partial v}{\partial r} + \frac{v}{r}\frac{\partial v}{\partial \theta} + \frac{uv}{r}\right) \tag{2.1.15}$$

in the r and θ directions, respectively. The density ρ is the bulk density of the material, g is the acceleration of gravity acting vertically, and u and v are the velocities in the r and θ directions, respectively.

The system of equations given by 2.1.11, 2.1.12, 2.1.13, 2.1.14, and 2.1.15 together with the appropriate boundary conditions properly define the problem for the determination of the three component stresses σ_r, σ_θ, and $\tau_{r\theta}$ and the two velocities u and v.

2. Solutions based on the Jenike-Shield Yield Criteria

In this section two approximate solutions to the system of equations developed in Chapter II, Section 1 will be presented. The flow

material is assumed to be a rigid-plastic, frictional solid obeying the Jenike-Shield yield condition [4]. The material is permitted to exhibit finite cohesion but non-steady state flow effects such as doming, arching, and piping are not permitted. Solutions are developed for steady gravity flow of these frictional materials. In general the bulk density is a function of mean pressure but in the present analysis it will be assumed constant.

The channel configuration is given in Fig. 2.3.1. For the analysis performed by Jenike the channel is not necessarily symmetric so that the channel walls are in general located at $+\theta_w^1$ and $-\theta_w^2$ with $|\theta_w^1|$ not necessarily equal to $|\theta_w^2|$. Also for the Jenike solution the problem is treated as an "initial value" problem and the boundary conditions at the upper and lower surfaces are not considered.

A. Jenike Solution

The solution developed by Jenike [42] will be briefly outlined. A discussion of the assumptions made in the development and their significance will follow.

The system of equations for the gravity flow of a frictional, cohesive solid through plane channels that was developed in Chapter II, Section 1 is given below

$$\frac{\partial \sigma_r}{\partial r} + \frac{1}{r}\frac{\partial \tau_{r\theta}}{\partial \theta} + \frac{1}{r}(\sigma_r - \sigma_\theta) + \rho g \cos\theta = -\rho\left(u\frac{\partial u}{\partial r} + \frac{v}{r}\frac{\partial u}{\partial \theta} - \frac{v^2}{r}\right) \quad (2.2.1)$$

$$\frac{\partial \tau_{r\theta}}{\partial r} + \frac{1}{r}\frac{\partial \sigma_\theta}{\partial \theta} + \frac{2}{r}\tau_{r\theta} - \rho g \sin\theta = -\rho\left(u\frac{\partial v}{\partial r} + \frac{v}{r}\frac{\partial v}{\partial \theta} + \frac{uv}{r}\right) \quad (2.2.2)$$

$$\sqrt{\left(\frac{\sigma_r - \sigma_\theta}{2}\right)^2 + \tau_{r\theta}^2} = \left(\frac{\sigma_r + \sigma_\theta}{2}\right) \sin\varphi \qquad (2.2.3)$$

$$\frac{\sigma_r - \sigma_\theta}{\tau_{r\theta}} = \frac{\frac{\partial u}{\partial r} - \frac{1}{r}\frac{\partial v}{\partial \theta} - \frac{u}{r}}{\frac{1}{2}\left(\frac{\partial v}{\partial r} - \frac{v}{r} + \frac{1}{r}\frac{\partial u}{\partial \theta}\right)} \qquad (2.2.4)$$

$$\frac{\partial u}{\partial r} + \frac{u}{r} + \frac{1}{r}\frac{\partial v}{\partial \theta} = 0 \quad . \qquad (2.2.5)$$

The bulk density has been assumed to be constant, independent of mean pressure and φ represents the "effective" friction angle to take into account the presence of cohesion.

Jenike assumes that the inertial terms in the r and θ equations of motion, Eqs. 2.2.1 and 2.2.2 respectively, are negligible compared to the stress terms so that these equations may be replaced with the equations of equilibrium. With this assumption the problem for the determination of the stress and velocity fields is separated, in that the stress field may be determined independently of the velocity field. The equations of equilibrium together with the Jenike-Shield yield condition, Eq. 2.2.3, and appropriate stress boundary conditions are sufficient for the determination of the stress field.

The equation of isotropy, Eq. 2.2.4, serves to relate the derived stress field and the unknown velocity field. Isotropy together with the condition of incompressibility expressed by the equation of continuity, Eq. 2.2.5, provide a sufficient set of equations for the determination of the velocity field. However, since the equation of isotropy is homogeneous in both the velocities and the stresses, the stress field will determine the velocity field only to within a multiplicative

constant. That is, the constitutive relations do not enforce uniqueness of the velocity field.

Following Sokolovski [87], the three component stresses are replaced by a mean stress, σ, and a stress angle, ψ, through the set of relations

$$\sigma_r = \sigma(1 + \sin\varphi\cos2\psi)$$

$$\sigma_\theta = \sigma(1 - \sin\varphi\cos2\psi) \qquad (2.2.6)$$

$$\tau_{r\theta} = \sigma\sin\varphi\sin2\psi \quad .$$

This system satisfies the Jenike-Shield yield condition identically. Substituting these relations into the equations of equilibrium, the problem for the determination of the stress field reduces to a set of two hyperbolic partial differential equations for the mean stress σ and the stress angle ψ.

Again following Sokolovski [87] the mean stress is assumed to vary linearly with r, so that σ may be written

$$\sigma = \gamma r s(\theta)$$

where γ is the bulk specific weight and $s(\theta)$ a function to describe the θ dependence of the mean stress. The stress angle, ψ, is assumed to be independent of r, that is,

$$\psi = \psi(\theta).$$

With these assumptions, the equations of equilibrium reduce to a set of ordinary, non-linear differential equations for the determination of $s(\theta)$ and $\psi(\theta)$. The stress fields defined by these equations are referred to as radial stress fields by Jenike [42]. These equations may be solved (algebraically) for the derivatives of s and ψ to give

$$\frac{d\psi}{d\theta} = F(\theta, \psi, s) = -1 - [ms \sin\varphi(1+\sin\varphi)(\cot\theta \sin2\psi + \cos2\psi - 1)$$

$$+ \cos\theta - \sin\varphi\cos(\theta+2\psi) + s\cos^2\varphi]/[2s \sin\varphi(\cos2\psi - \sin\varphi)]$$

$$\frac{ds}{d\theta} = G(\theta, \psi, s) =$$

(2.2.7)

$$\frac{s \sin2\psi + \sin(\theta+2\psi) + ms \sin\varphi[\cot\theta(1+\cos2\psi) - \sin2\psi]}{\cos2\psi - \sin\varphi}$$

where $m = 0$ for plane strain. Integrating these equations with respect to θ gives

$$\psi(\theta) = \psi(\theta^\circ) + \int_{\theta^\circ}^{\theta} F(t, \psi(t), s(t))dt$$

and

$$s(\theta) = s(\theta^\circ) + \int_{\theta^\circ}^{\theta} G(t, \psi(t), s(t))dt$$

where θ° is the initial ray.

As discussed earlier the equilibrium equations are two hyperbolic partial differential equations in r and θ for the two stress functions σ and ψ. For a real channel, boundary conditions exist for the stress functions at the entrance and exit planes of the channel. However, in this approach the problem is actually treated as an initial value type problem with initial values specified along the ray $\theta = \theta^\circ$ without considering boundary conditions at the upper and lower surfaces.

The material is assumed to satisfy a Coulomb condition along the walls, namely

$$\left.\frac{\tau_{r\theta}}{\sigma_\theta}\right|_{\theta=\theta_w^1} = -\tan\delta^1 \text{ along } \theta = \theta_w^1 \text{ and}$$

(2.2.8)

$$\left.\frac{\tau_{r\theta}}{\sigma_\theta}\right|_{\theta=\theta_w^2} = +\tan\delta^2 \text{ along } \theta = \theta_w^2 \quad.$$

The set of Eqs. 2.2.7 cannot be solved in closed form for ψ and s and then the above wall conditions Eq. 2.2.8 applied. Therefore, it is necessary for the equations for ψ and s to be integrated numerically for a particular set of initial conditions and the corresponding values of the solution at the walls determined. The process is continued until the correct initial set is found to give the desired Coulomb condition along the walls. The solution procedure is analogous to knowing the magnitude of the solution to a differential equation at some time $t = t_0$ and then choosing different initial values for the solution at time $t = 0$ until the particular initial value that gives the correct value at $t = t_0$ is found.

Plots of $\psi(\theta)$ and $s(\theta)$ versus θ are given by Jenike [45] for a variety of initial conditions. A complete set of these plots is given in references [20] and [22].

If it is assumed that the velocity field is of the form

$$u = \frac{f(\theta)}{r} \tag{2.2.9}$$

that is, that the velocity field is radial, then the equation of continuity is satisfied identically.[*] Substitution of the above radial velocity field into the equation of isotropy gives

$$\psi = \psi(\theta).$$

Hence, radial velocity fields and radial stress fields are "compatible."

Since $\psi = \psi(\theta)$ is determined from the solution to the stress

---

[*]For $u = \frac{f(\theta)}{r}$ the equation of continuity gives $V = v(r)$. However, since V must vanish at the walls, the solution must be $V \equiv 0$

problem, the equation of isotropy actually gives an ordinary differential equation for the determination of $f(\theta)$. From Jenike [42],

$$f(\theta) = A \, \exp[-(2+m)\int \tan 2\psi(\theta)d\theta] \qquad (2.2.10)$$

where $m = 0$ for plane strain and $\psi(\theta)$ is given by the solution to the stress problem.

By considering the partial differential equations of equilibrium in terms of σ and ψ it is seen that the choice of

$$\sigma = \gamma r s(\theta) \qquad \text{and}$$

$$\psi = \psi(\theta)$$

reduces the equations to ordinary differential equations for σ and ψ. The above scheme works because when the inertial terms are neglected all remaining terms that contain σ involve division by r or differentiation with respect to r, and the only term not containing σ, the body force term, is independent of r.

For the problem of the flow of a Newtonian fluid through converging channels a similar reduction is possible. A body force term is not present, and it is seen that for the pressure of the form

$$P = \frac{s(\theta)}{r^2}$$

and the radial velocity of the form

$$u = \frac{f(\theta)}{r}$$

the partial differential equations of motion reduce to ordinary

differential equations for $s(\theta)$ and $f(\theta)$.

In the Jenike analysis the inertial terms in the equation of motion are neglected. However, at the exit plane the radial velocity with a $\frac{1}{r}$ dependence must be at its maximum and for "reasonable" flow rates, hardly negligible. With a radial velocity of the form $\frac{f(\theta)}{r}$, the inertial terms in r equation of motion must be of the form $\frac{f^2(\theta)}{r^3}$ which is not compatible with the assumed radial stress field. Therefore, for non-negligible inertial terms associated with a radial velocity field, a stress term of the form

$$\sigma \sim \frac{s(\theta)}{r^2}$$ similar to the form of the mean

pressure in the Newtonian problem, is required to balance the inertial terms.

The Jenike solution, because of the linear variation of mean stress with position r, cannot be extended upward to a traction free boundary. But as discussed above, the solution is valid near the exit plane only for the case of "small" flow rates and the predicted velocities are not unique.* Thus, while the Jenike solution does represent a major step in the understanding of the gravity flow of frictional materials the solution has serious drawbacks. Alternative solutions retaining the inertial terms will now be discussed.

B. Sullivan Solution

An alternate approximate solution to the system of equation developed in Chapter II, Section 1 was proposed by Sullivan [95]. The

---

*The flow rate must be small enough that the inertial terms in the equations of motion are negligible.

material was assumed to obey the Jenike-Shield yield condition. The material was also assumed to be cohesionless so that the effective angle of friction in the Jenike-Shield yield condition is just the internal friction angle. Bulk density was taken as constant at the value of the material density at the critical void ratio.

The geometry of the channel is given in Fig. 2.3.1. The channel is symmetric with straight walls at $+\theta_w$ and $-\theta_w$. In general, the material will satisfy a Coulomb condition along the walls, namely

$$\frac{\tau_{r\theta}}{\sigma_\theta}\bigg|_{\theta = \theta_w} = -\tan\delta.$$

However, the analysis described below will be valid only for the case of frictionless channel walls where $\delta = 0$. The entrance and exit planes at $r = R$ and $r = r_0$ are assumed to be traction free surfaces with $\tau_{r\theta} = \sigma_\theta = \sigma_r = 0$. It is also assumed that the channel walls are "sufficiently steep" that the body force acts in a purely radial direction. The resultant solution is referred to by Sullivan as the radial body force solution.

Following Sokolovski [87], the component stresses are expressed in terms of a mean stress σ and a stress angle ψ through the following relations

$$\tau_{r\theta} = \sigma \sin\varphi \sin 2\psi$$

$$\sigma_\theta = \sigma(1 - \sin\varphi \cos 2\psi)$$

$$\sigma_r = \sigma(1 + \sin\varphi \cos 2\psi)$$

These relations satisfy the yield condition identically so that the system of Eqs. 2.2.1 to 2.2.5 reduce to a set of four partial differential

equations for the stress functions σ and ψ and the radial and tangential velocities u and v.

A solution of the following form, valid for the case of steep, frictionless walls, is assumed.

$$\sigma = S(r)$$
$$\psi = \frac{\pi}{2}$$
$$u = u(r)$$
$$v = 0.^*$$

(2.2.11)

From continuity it is seen that $u(r)$ must be of the form

$$u(r) = \bar{u}\frac{r_0}{r}$$

(2.2.12)

where $\bar{u}$ is the constant, and as yet undetermined, exit velocity. The isotropy equation and the θ equation of motion reduce to identities. The r equation of motion reduces to the following ordinary differential equation for the determination of the mean stress $S(r)$,

$$\frac{dS}{dr}(1-\sin\varphi) - \frac{2}{r}S\sin\varphi + \rho g = \rho\frac{(r_0\bar{u})^2}{r^3}$$

(2.2.13)

with the homogenous solution

$$S_H = c_1 r^{\frac{2\sin\varphi}{1-\sin\varphi}}$$

where c_1 is an arbitrary constant, and a particular solution

---

*With the assumption that $\psi \to \frac{\pi}{2}$, the $r - \theta$ axes become principal axes and thus $\tau_{r\theta} \equiv 0$. Thus this solution represents the case where the shear is identically zero along the walls.

$$S_P = \frac{\rho g r}{3 \sin\varphi - 1} - \rho \frac{\overline{u}^2}{2} \left(\frac{r_0}{r}\right)^2 \quad \text{for } \sin\varphi \neq \frac{1}{3}$$

and

$$S_P = \frac{3}{2} \rho g r \log r - \rho \left(\frac{r_0}{r}\right)^2 \frac{\overline{u}^2}{2} \quad \text{for } \sin\varphi = \frac{1}{3}.$$

Considering the case where $\sin\varphi \neq \frac{1}{3}$, the expression for the mean stress becomes

$$S(r) = S_H + S_P = c_1 r^{\frac{2\sin\varphi}{1-\sin\varphi}} + \frac{\rho g r}{3\sin\varphi - 1} - \rho \frac{\overline{u}^2}{2} \left(\frac{r_0}{r}\right)^2. \quad (2.2.14)$$

Applying the homogenous stress boundary condition at the upper surface $r = R$ determines the constant c_1 so that $S(r)$ may be written

$$S(r) = \frac{\rho g r}{3\sin\varphi - 1} \left[1 - \left(\frac{r}{R}\right)^{\frac{3\sin\varphi - 1}{1-\sin\varphi}}\right] - \rho \frac{\overline{u}^2}{2} \left(\frac{r_0}{r}\right)^2 \left[1 - \left(\frac{r}{R}\right)^{\frac{2}{1-\sin\varphi}}\right] ;$$
$$(2.2.15)$$

applying the homogenous stress boundary condition at the lower surface $r = r_0$ determines a unique value of the exit velocity $\overline{u}$, namely,

$$\frac{\overline{u}^2}{r_0 g} = \frac{2}{3\sin\varphi - 1} \left[\frac{1 - \left(\frac{r_0}{R}\right)^{\frac{3\sin\varphi - 1}{1-\sin\varphi}}}{1 - \left(\frac{r_0}{R}\right)^{\frac{2}{1-\sin\varphi}}}\right] \quad (2.2.16)$$

For the particular case where $\sin\varphi = \frac{1}{3}$ the exit velocity becomes

$$\frac{\overline{u}^2}{r_0 g} = \frac{3 \log\left(\frac{R}{r_0}\right)}{1 - \left(\frac{r_0}{R}\right)^3} \quad (2.2.17)$$

The dimensionless exit velocity $\dfrac{\bar{u}^2}{gr_0}$, is plotted versus dimensionless head, $\dfrac{R}{r_0}$, in Fig. 2.2.1 for various values of internal friction angle φ. For $\sin\varphi > \dfrac{1}{3}$ the exit velocity becomes independent of head for large $\dfrac{R}{r_0}$, the limiting value being given by

$$\frac{\bar{u}^2}{gr_0} = \frac{2}{3\sin\varphi-1} \quad \text{for} \quad \sin\varphi > \frac{1}{3} \quad \text{and} \quad \frac{R}{r_0} \text{ large} . \qquad (2.2.18)$$

for $\sin\varphi \leq \dfrac{1}{3}$ the exit velocity continuously increases with increasing head analogous to fluid-like behavior. For $\varphi \to 0$, the exit velocity becomes

$$\frac{\bar{u}^2}{r_0 g} = \frac{\dfrac{R}{r_0} - 1}{1 - \dfrac{r_0}{R}^2} \qquad (2.2.19)$$

the result identical with that given by Bernoulli equation for a perfect fluid.

For the limiting case where $\sin\varphi > \dfrac{1}{3}$ and $\dfrac{R}{r_0}$ is large and with the dimensionless exit velocity given by Eq. 2.2.18 above, exit velocity is plotted versus opening angle for $\varphi = 35°$ in Fig. 2.2.2[*]. Also shown is flow rate data collected by Sullivan [95]. It is seen that the radial body force solution predicts the correct trend in the data in regard to the dependence of dimensionless exit velocity on opening angle. However, the magnitude of the predicted flow rate for a given value of opening angle θ_w is substantially above the experimental data.

The radial body force solution could be considered an exact solution for the case of radial gravity and frictionless walls. The assumption

---

[*]The dimensionless exit velocity in Fig. 2.2.2 is based on the channel opening at the exit, D, which may be expressed in terms of the exit radius r_0 as

$$D = 2r_0 \tan\theta_w .$$

that the $\psi \to \frac{\pi}{2}$ makes the $r - \theta$ axes principal axes and $\tau_{r\theta} \equiv 0$. Thus, this solution represents the case where the shear stress is identically zero along the walls. The fact that the predicted flow rate is greater than that experienced in real channels is perhaps due to the retardation of the flow in real channels by the Coulomb shear stress acting along the walls.

The Sullivan solution does represent a significant advancement from the work of Jenike in that (1) it does determine a unique velocity field coupled with the stress field, (2) the mean stress includes terms associated with body and inertial forces, and (3) the solution does satisfy boundary conditions at the entrance and exit to the channel. The addition of the Coulomb condition along the wall to account for wall shear and the addition of non-radial gravity would represent a significant advancement beyond the Sullivan solution.

3. Perturbation Solution

A. Complete Solution — Variable Wall Friction Angle

An approximate solution, developed in the course of the present investigation, for the gravity flow of a frictional, cohesive solid through plane converging channels will now be presented. The system of equations developed in Section 1, along with a brief description, is given below.

$$\frac{\partial \sigma_r}{\partial r} + \frac{1}{r}\frac{\partial \tau_{r\theta}}{\partial \theta} + \frac{1}{r}(\sigma_r - \sigma_\theta) + \rho g \cos\theta = -\rho\left(u\frac{\partial u}{\partial r} + \frac{v}{r}\frac{\partial u}{\partial \theta} - \frac{v^2}{r}\right) \qquad (2.3.1)$$

$$\frac{\partial \tau_{r\theta}}{\partial r} + \frac{1}{r}\frac{\partial \sigma_\theta}{\partial \theta} + \frac{2}{r}\tau_{r\theta} - \rho g \sin\theta = -\rho\left(u\frac{\partial v}{\partial r} + \frac{v}{r}\frac{\partial v}{\partial \theta} + \frac{uv}{r}\right) \qquad (2.3.2)$$

$$\sqrt{\left(\frac{\sigma_r-\sigma_\theta}{2}\right)^2 + \tau_{r\theta}^2} = \left(\frac{\sigma_r+\sigma_\theta}{2}\right)\sin\varphi \qquad (2.3.3)$$

$$\frac{\sigma_r-\sigma_\theta}{\tau_{r\theta}} = \frac{\dfrac{\partial u}{\partial r} - \dfrac{1}{r}\dfrac{\partial v}{\partial\theta} - \dfrac{u}{r}}{\dfrac{1}{2}\left(\dfrac{\partial v}{\partial r} - \dfrac{v}{r} + \dfrac{1}{r}\dfrac{\partial u}{\partial\theta}\right)} \qquad (2.3.4)$$

$$\frac{\partial u}{\partial r} + \frac{u}{r} + \frac{1}{r}\frac{\partial v}{\partial\theta} = 0 \quad . \qquad (2.3.5)$$

Equations 2.3.1 and 2.3.2 are the r direction and θ direction equations of motion, respectively. Equation 2.3.3 is the assumed Jenike-Shield yield condition, where φ is the effective angle of friction. For a cohesionless material the effective angle of friction proposed by Jenike and Shield [4] is equal to the internal friction angle defined in Appendix B.

The material is assumed to be isotropic such that the directions of principal stress and strain rate coincide. The assumption is expressed by the isotropy condition, Eq. 2.3.4.

Using the work-hardening model for a Coulomb solid proposed by Jenike and Shield [4] and discussed in Section 1 of this chapter, continuous failure is permitted with negligible volume change. This condition is expressed by the equation of continuity Eq. 2.3.5.

The channel configuration and boundary conditions are given in Fig. 2.3.1. The channel centerline is along the $\theta = 0$ line with the walls located at $\pm\theta_w$. Traction-free surfaces exist at $r = R$, the upper surface, and $r = r_0$, the lower surface. Along the walls the tangential and normal stresses are related by the Coulomb condition

$$\left.\frac{\tau_{r\theta}}{\sigma_\theta}\right|_{\theta=\theta_w} = (-\tan\delta)\,f(r)$$

where δ is the wall friction angle. A function $f(r)$ is included for generality so that the friction condition may vary as a function of position along the wall. The significance of variable wall friction angle will be discussed in detail later.

The solution proposed by Sullivan [95] and discussed in detail in Section 2 was of the following form

$$\sigma = \sigma(r), \quad \psi = \frac{\pi}{2}, \quad u = \frac{A}{r}, \quad v \equiv 0 \quad .$$

The condition that $\psi \to \frac{\pi}{2}$ makes the $r - \theta$ directions principal directions, and thus along any ray (the walls of the channel for instance) the shear stress must be identically zero. The Sullivan solution could be considered an "exact" solution for the case of radial gravity and frictionless walls. A perturbation to Sullivan's solution is given in Appendix A. A perturbation approach in which the solution to the zeroth order equation is a solution to the complete system of equations only to order, ϵ, where ϵ is the perturbation parameter will be taken here.

Following Sokolovski [87], the three component stresses are replaced by a mean stress, σ, and a stress angle, ψ, through the relations

$$\tau_{r\theta} = \sigma\sin\varphi\sin2\psi, \quad \sigma_\theta = \sigma(1-\sin\varphi\cos2\psi), \quad \sigma_r = \sigma(1+\sin\varphi\cos2\psi) \quad . \qquad (2.3.6)$$

The system Eq. 2.3.6 satisfies the Jenike-Shield yield condition, Eq. 2.3.4, identically. The meaning of the functions σ and ψ is best seen from a Mohr diagram, Fig. 2.3.2. The Mohr Envelope is inclined at an angle of $\pm\varphi$ to the σ axis. The Mohr Circle for a material at yield is

tangent to the Mohr Envelope. The mean stress, σ, gives the location of the center of the Mohr Circle and the stress angle ψ gives the location of the particular stress state, in r-θ coordinates, relative to the principal axes. For $\psi \to \pi/2$, $\sigma_\theta \to \sigma_1$, $\sigma_r \to \sigma_2$ and the r-θ axes become principal axes.

An expansion of the system variables σ, ψ, u, v of the following form is assumed.

$$u \sim U_0(r) + \beta_{11}(\epsilon)u_1 + \beta_{12}(\epsilon)u_2 + \cdots$$

$$v \sim 0 + \beta_{21}(\epsilon)v_1 + \beta_{22}(\epsilon)v_2 + : \cdots$$

$$\psi \sim \frac{\pi}{2} + \beta_{31}(\epsilon)\psi_1 + \beta_{32}(\epsilon)\psi_2 + \cdots$$

$$\sigma \sim \sigma_0 + \beta_{41}(\epsilon)\sigma_1 + \beta_{42}(\epsilon)\sigma_2 + \cdots$$

(2.3.7)

In the analysis performed by Sullivan [95] for the case of steep frictionless channel walls, the stress angle ψ is constant at the value $\frac{\pi}{2}$. Intuitively, for small deviations from this idealized case it seems reasonable that the perturbation in the value of the stress angle from $\frac{\pi}{2}$ should be small. For this reason the coefficient β_{ij} is assigned the value ϵ. The size of the coefficients β_{ij} may then be determined in terms of ϵ by substituting the relations given in Eq. 2.3.7 into the complete system of partial differential equations. It will be shown by direct substitution that the values of the coefficients that result from this prodecure are just

$$\beta_{11} \sim \epsilon^2, \ \beta_{21} \sim \epsilon^3, \ \beta_{31} \sim \epsilon, \ \beta_{41} \sim \epsilon^2, \ \beta_{12} \sim \epsilon^4, \ \beta_{32} \sim \epsilon^3, \ \beta_{42} \sim \epsilon^4$$

where $\epsilon \sim \dfrac{h}{r_0}$ and r_0 is taken as the reference length to be used in reducing the system of equations to dimensionless form. The half channel opening, h, is of order $r_0\theta_w$ so that $\dfrac{h}{r_0} \sim \dfrac{r_0\theta_w}{r_0} \sim \theta_w$.

The radial velocity is just

$$u \sim U_0(r) + \epsilon^2 u_1 + \epsilon^4 u_2 \ldots$$

Choose as a reference velocity, U*, the average zeroth order exit velocity (the material velocity at the channel exit plane). The dimensionless radial velocity then becomes

$$\frac{u}{U*} \sim \frac{U_0(r)}{U*} + \epsilon^2 \frac{u_1}{U*} + \epsilon^4 \frac{u_2}{U*} + \ldots$$

which may also be written

$$\frac{u}{U*} \sim \frac{U_0}{U*} \left(1 + \epsilon^2 \frac{u_1}{U_0} + \epsilon^4 \frac{u_2}{U_0} + \ldots\right) .$$

In the discussion that follows, a function enclosed in double brackets will be taken to indicate the order of magnitude of that function and a bar over a function will be taken to indicate the dimensionless form of that function. Now $\left\{\!\!\left\{\frac{u_1}{u_0}\right\}\!\!\right\} = 1$ so that $\left\{\!\!\left\{\epsilon^2 \frac{u_1}{u_0}\right\}\!\!\right\} = \epsilon^2 \ll 1$. The dimensionless radial velocity, $\overline{u}$, may be written

$$\overline{u} = \overline{U}_0 + \epsilon^2 \overline{u}_1 + \epsilon^4 \overline{u}_2 + \ldots \qquad (2.3.8)$$

In a similar fashion the dimensionless circumferential velocity, $\overline{v}$, becomes

$$\overline{v} = 0 + \epsilon^3 \overline{v}_1 + \beta_{22}(\epsilon)\overline{v}_2 \qquad (2.3.9)$$

where $\beta_{22}(\epsilon)$ has not yet been determined.

The stress angle, ψ, is given in Eq. 2.3.7. Choose, $\frac{\pi}{2}$, as the reference value of ψ so that the dimensionless ψ may be written

$$\overline{\Psi} = 1 + \epsilon\overline{\Psi}_1 + \epsilon^3\overline{\Psi}_2 + \ldots \tag{2.3.10}$$

where $\left\{\!\!\left\{\overline{\Psi}_1\right\}\!\!\right\} = 1$ and $\left\{\!\!\left\{\epsilon\overline{\Psi}_1\right\}\!\!\right\} = \epsilon.$

The second stress function, σ, which is just the mean stress, is also given in Eq. 2.3.7. Choose $\rho g r_0$, where ρ is the bulk density, g the local acceleration of gravity, and r_0 the reference length described earlier, as the reference stress, so that the dimensionless mean stress may be written

$$\overline{\sigma} = \overline{\sigma}_0 + \epsilon^2\overline{\sigma}_1 + \epsilon^4\overline{\sigma}_2 + \ldots \tag{2.3.11}$$

In summary, the dimensionless form of the proposed perturbation solution is just

$$\overline{u} = \overline{U}_0(r) + \epsilon^2\overline{u}_1 + \epsilon^4\overline{u}_2 + \ldots$$

$$\overline{v} = 0 + \epsilon^3\overline{v}_1 + \beta_{22}(\epsilon)\overline{v}_2 + \ldots$$

$$\overline{\Psi} = 1 + \epsilon\overline{\Psi}_1 + \epsilon^3\overline{\Psi}_2 + \ldots \tag{2.3.12}$$

$$\overline{\sigma} = \overline{\sigma}_0 + \epsilon^2\overline{\sigma}_1 + \epsilon^4\overline{\sigma}_2 + \ldots$$

Let $\overline{r} = \dfrac{r}{r_0}$ and $\overline{\theta} = \dfrac{\theta}{\theta_w}$ so that the equation of continuity, Eq. 2.3.5 given earlier, may be written in dimensionless form as

$$\frac{\partial\overline{u}}{\partial\overline{r}} + \frac{\overline{u}}{\overline{r}} + \frac{1}{\epsilon}\frac{1}{\overline{r}}\frac{\partial\overline{v}}{\partial\overline{\theta}} = 0 \tag{2.3.13}$$

Substitute for $\overline{u}$ and $\overline{v}$ from Eq. 2.3.12 into Eq. 2.3.13 to obtain

$$\frac{d\overline{U}_0}{d\overline{r}} + \frac{\overline{U}_0}{\overline{r}} + \epsilon^2 \left[\frac{\partial\overline{u}_1}{\partial\overline{r}} + \frac{\overline{u}_1}{\overline{r}} + \frac{1}{\overline{r}}\frac{\partial\overline{u}_1}{\partial\overline{\theta}} \right] + \ldots = 0 \quad .$$

Thus, the zeroth order and ϵ^2 order equations of continuity are

zeroth order
$$\frac{d\overline{U}_0}{d\overline{r}} + \frac{\overline{U}_0}{\overline{r}} = 0$$

$$(2.3.14)$$

and ϵ^2 order
$$\frac{\partial\overline{u}_1}{\partial\overline{r}} + \frac{\overline{u}_1}{\overline{r}} + \frac{1}{\overline{r}}\frac{\partial\overline{v}_1}{\partial\overline{\theta}} = 0$$

respectively. Higher order equations may be obtained in a similar fashion but for the present analysis the perturbation will only be carried out to order ϵ^2.

The equation of isotropy as given in Eq. 2.3.4 is

$$\frac{\sigma_r - \sigma_\theta}{\tau_{r\theta}} = \frac{\dfrac{\partial u}{\partial r} - \dfrac{1}{r}\dfrac{\partial v}{\partial \theta} - \dfrac{u}{r}}{\dfrac{1}{2}\left(\dfrac{\partial v}{\partial r} - \dfrac{v}{r} + \dfrac{1}{r}\dfrac{\partial u}{\partial \theta}\right)} \quad .$$

Using the expressions for σ_r, σ_θ and $\tau_{r\theta}$, Eq. 2.3.6, the LHS of the above equation becomes $\dfrac{2}{\tan(2\psi)}$, independent of the mean stress. With an additional substitution from continuity, Eq. 2.3.5, the equation of isotropy reduces to

$$\frac{2\dfrac{\partial u}{\partial r}}{\dfrac{\partial v}{\partial r} - \dfrac{v}{r} + \dfrac{1}{r}\dfrac{\partial u}{\partial \theta}} = \frac{1}{\tan(2\psi)} \quad .$$

$$(2.3.15)$$

Writing the isotropy equation in dimensionless form and substituting for $\overline{u}$, $\overline{v}$, $\overline{\psi}$ in terms of the perturbation variables, Eq. 2.3.15 becomes

$$\epsilon^3 \left(\frac{\partial \overline{v}_1}{\partial \overline{r}} - \frac{\overline{v}_1}{\overline{r}} \right) + \epsilon \frac{1}{\overline{r}} \frac{\partial \overline{u}_1}{\partial \overline{\theta}} + \beta_{22} \frac{\partial v_2}{\partial \overline{r}} - \frac{\overline{v}_2}{\overline{r}} + \epsilon^3 \frac{1}{\overline{r}} \frac{\partial \overline{u}_2}{\partial \overline{\theta}} + 0(\epsilon^5)$$

$$= \epsilon \left[\frac{d\overline{U}_0}{d\overline{r}} + \epsilon^2 \frac{\partial \overline{u}_1}{\partial \overline{r}} + \epsilon^4 \frac{\partial \overline{u}_2}{\partial \overline{r}} + 0(\epsilon^6) \right] \cdot 2\pi \left(\epsilon \overline{\Psi}_1 + \epsilon^3 \overline{\Psi}_2 + 0(\epsilon^5) \right) \quad .$$

Equating terms with like powers of ϵ, the zeroth order, ϵ^1 and ϵ^3 order equations of isotropy are obtained

zeroth order $0 = 0$

ϵ^1 order

$$\frac{1}{\overline{r}} \frac{\partial \overline{u}_1}{\partial \overline{\theta}} - 2\pi \overline{\Psi}_1 \frac{d\overline{U}_0}{d\overline{r}} = 0 \qquad (2.3.16)$$

ϵ^3 order

$$\frac{\partial \overline{v}_1}{\partial \overline{r}} - \frac{\overline{v}_1}{\overline{r}} + \frac{1}{\overline{r}} \frac{\partial \overline{u}_2}{\partial \overline{\theta}} - 2\pi \frac{d\overline{U}_0}{d\overline{r}} \overline{\Psi}_2 + \overline{\Psi}_1 \frac{\partial \overline{u}_1}{\partial \overline{r}} = 0$$

The stresses σ_r, σ_θ and $\tau_{r\theta}$ may be written in terms of the perturbation variables by substituting for σ and ψ in the Sokolovski relations Eq. 2.3.6. Thus,

$$\overline{\sigma}_r = (\overline{\sigma}_0 + \epsilon^2 \overline{\sigma}_1 + \epsilon^4 \overline{\sigma}_2)(1 - \sin\varphi \cos(\pi\epsilon\overline{\Psi}_1 + \pi\epsilon^3\overline{\Psi}_2))$$

$$\overline{\sigma}_\theta = (\overline{\sigma}_0 + \epsilon^2 \overline{\sigma}_1 + \epsilon^4 \overline{\sigma}_2)(1 + \sin\varphi \cos(\pi\epsilon\overline{\Psi}_1 + \pi\epsilon^3\overline{\Psi}_2)) \qquad (2.3.17)$$

$$\overline{\tau}_{r\theta} = -(\overline{\sigma}_0 + \epsilon^2 \overline{\sigma}_1 + \epsilon^4 \overline{\sigma}_2) \sin\varphi \sin(\pi\epsilon\overline{\Psi}_1 + \pi\epsilon^3\overline{\Psi}_2)$$

with terms of order ϵ^5 for $\overline{\psi}$ and ϵ^6 for $\overline{\sigma}$ suppressed.[*]

---

[*]Note: Use has been made of the following trigonometric identities
$$\cos(\pi + \theta) = -\cos\theta$$
and $\sin(\pi + \theta) = -\sin\theta$ so that
$$\cos(2\psi) = \cos(2\pi + 2\epsilon\psi_1 + 2\epsilon^3\psi_2 + \cdots) = -\cos(2\epsilon\psi_1 + 2\epsilon^3\psi_2 + \cdots)$$
$$\sin(2\psi) = \sin(2\pi + 2\epsilon\psi_1 + 2\epsilon^3\psi_2 + \cdots) = -\sin(2\epsilon\psi_1 + 2\epsilon^3\psi_2 + \cdots)$$

Writing the θ-equation of motion, Eq. 2.3.2, in dimensionless form and substituting for the dimensionless stresses the above expressions, the θ equation of motion becomes

$$\frac{1}{\epsilon}\left\{\frac{\partial\overline{\sigma}_0}{\partial\overline{\theta}}(1+\sin\varphi)\right\}+\epsilon\left\{-\pi\sin\varphi\frac{\partial\overline{\sigma}_0}{\partial\overline{r}}\overline{\psi}_1-\pi\sin\varphi\overline{\sigma}_0\frac{\partial\overline{\psi}_1}{\partial\overline{r}}+\frac{1}{\overline{r}}\frac{\partial\overline{\sigma}_1}{\partial\overline{\theta}}(1+\sin\varphi)\right.$$

$$\left.-\pi^2\sin\varphi\frac{\overline{\sigma}_0}{\overline{r}}\overline{\psi}_1\frac{\partial\overline{\psi}_1}{\partial\overline{\theta}}-2\pi\sin\varphi\frac{\overline{\sigma}_0\overline{\psi}_1}{\overline{r}}-\overline{\theta}-\left(\frac{1+\sin\varphi}{2}\right)\pi^2\frac{\partial\overline{\sigma}_0}{\partial\overline{\theta}}\overline{\psi}_1^2\right\}+$$

$$\epsilon^3\left\{-\pi\sin\varphi\left(\frac{\partial\overline{\sigma}_0}{\partial\overline{r}}\overline{\psi}_2+\frac{\partial\overline{\sigma}_1}{\partial\overline{r}}\overline{\psi}_1\right)-\pi\sin\varphi\left(\overline{\sigma}_0\frac{\partial\overline{\psi}_2}{\partial\overline{r}}+\overline{\sigma}_1\frac{\partial\overline{\psi}_1}{\partial\overline{r}}\right)+\frac{1}{\overline{r}}\frac{\partial\overline{\sigma}_2}{\partial\overline{\theta}}\left(1+\sin\varphi\right)\right.$$

$$-\pi^2\sin\varphi\left(\frac{\overline{\sigma}_0}{\overline{r}}\left[\overline{\psi}_1\frac{\partial\overline{\psi}_2}{\partial\overline{\theta}}+\overline{\psi}_2\frac{\partial\overline{\psi}_1}{\partial\overline{\theta}}\right]+\frac{\overline{\sigma}_1}{\overline{r}}\overline{\psi}_1\frac{\partial\overline{\psi}_1}{\partial\overline{\theta}}\right)-2\pi\sin\varphi\left(\frac{\overline{\sigma}_0\overline{\psi}_2}{\overline{r}}+\frac{\overline{\sigma}_1\overline{\psi}_1}{\overline{r}}\right)+\frac{1}{6}\overline{\theta}^3+$$

$$\left[-\pi^2(1+\sin\varphi)\frac{\partial\overline{\sigma}_0}{\partial\overline{\theta}}\overline{\psi}_1\overline{\psi}_2-\frac{1+\sin\varphi}{2}\pi^2\frac{\partial\overline{\sigma}_1}{\partial\overline{\theta}}\overline{\psi}_1^2\right]$$

$$\left.+\left[\overline{U}_0\frac{\partial\overline{v}_1}{\partial\overline{r}}+\frac{\overline{U}_0\overline{v}_1}{\overline{r}}\right]F_r^2\right\}+0(\epsilon^5)=0 \qquad **$$

where F_r is the Froude number defined as $F_r=\dfrac{U*}{\sqrt{gr_0}}$. Before separating the θ equation of motion into equations of increasing order in ϵ , the r equation of motion will be considered. Following the same procedure outlined above for the θ equation of motion, the r equation

---

** Both sine and cosine of the perturbation variables have been expanded in a Taylor's series about the origin. Thus,

$$\sin(2\epsilon\psi_1+2\epsilon^3\psi_2+\cdots)=2\epsilon\psi_1+2\epsilon^3\psi_2+\cdots-\frac{(2\epsilon\psi_1+2\epsilon^3\psi_2+\cdots)^3}{3!}+\cdots$$

$$\cos(2\epsilon\psi_1+2\epsilon^3\psi_2+\cdots)=1-\frac{(2\epsilon\psi_1+2\epsilon^3\psi_2+\cdots)^2}{2!}+\cdots+$$

becomes

$$\epsilon^0\left\{\frac{\partial\bar{\sigma}_0}{\partial\bar{r}}(1-\sin\varphi)-\pi\sin\varphi\frac{\bar{\sigma}_0}{\bar{r}}\frac{\partial\bar{\Psi}_1}{\partial\bar{\theta}}-2\sin\varphi\frac{\bar{\sigma}_0}{\bar{r}}+1+F_r^2\bar{U}_0\frac{d\bar{U}_0}{d\bar{r}}-\pi\sin\varphi\frac{\partial\bar{\sigma}_0}{\partial\bar{\theta}}\frac{\bar{\Psi}_1}{\bar{r}}\right\}+$$

$$\epsilon^2\left\{\frac{\partial\bar{\sigma}_1}{\partial\bar{r}}(1-\sin\varphi)+\pi^2\sin\varphi\,\bar{\sigma}_0\bar{\Psi}_1\frac{\partial\bar{\Psi}_1}{\partial\bar{r}}-\pi\sin\varphi\frac{1}{\bar{r}}\frac{\partial\bar{\sigma}_1}{\partial\bar{\theta}}\bar{\Psi}_1-\pi\frac{\sin\varphi}{\bar{r}}\bar{\sigma}_1\frac{\partial\bar{\Psi}_1}{\partial\bar{\theta}}\right.$$

$$-\frac{2\bar{\sigma}_1}{\bar{r}}\sin\varphi-\frac{\bar{\theta}^2}{2}+F_r^2\left(\bar{U}_0\frac{\partial\bar{u}_1}{\partial\bar{r}}+\bar{u}_1\frac{d\bar{U}_0}{d\bar{r}}\right)-\pi\frac{\sin\varphi}{\bar{r}}\bar{\sigma}_0\frac{\partial\bar{\Psi}_2}{\partial\bar{\theta}}$$

$$\left.+\left[\frac{\pi\sin\varphi}{6}\frac{\partial\bar{\sigma}_0}{\partial\theta}\bar{\Psi}_1^3\right]\right\}=0$$

Consider the Coulomb friction condition along the walls,

$$\left.\frac{\tau_{r\theta}}{\sigma_\theta}\right|_{\theta=\theta_w}=(-\tan\delta)f(r) \qquad (2.3.18)$$

where δ is the wall friction angle and $f(r)$ is a prescribed function of r. Substituting the expressions for $\tau_{r\theta}$ and σ_θ in terms of σ and ψ in Eq. 2.3.18 the wall condition becomes

$$\left.\frac{+\sin\varphi\cos2\Psi}{1-\sin\varphi\cos2\Psi}\right|_{\theta=\theta_w}=-\tan\delta\,f(r)$$

(handwritten above: $\sin2\psi$)

independent of the mean stress, σ. In terms of the perturbation variables ψ_1 and ψ_2 the wall condition is just

$$-\sin\varphi\sin(\pi\epsilon\bar{\Psi}_1(\bar{r},\theta_w)+\pi\epsilon^3\bar{\Psi}_2(\bar{r},\theta_w))$$

$$=(-\tan\delta)f(r)\left[1+\sin\varphi\cos(\pi\epsilon\bar{\Psi}_1(\bar{r},\theta_w)+\pi\epsilon^3\bar{\Psi}_2(\bar{r},\theta_w))\right]$$

where $\overline{\psi}_1 \big|_{\theta = \theta_w} = \overline{\psi}_1(\overline{r}, \theta_w)$. Expanding the sine and cosine functions in Taylor's series about the origin and considering the first order terms above, the boundary value for $\overline{\psi}_1 \big|_{\theta = \theta_w}$ is found to be

$$\overline{\psi}_1(\overline{r}, \theta_w) = \frac{2}{\pi} \left(\frac{\tan\delta}{\epsilon}\right) f(r) \left(\frac{1 + \sin\varphi}{2\sin\varphi}\right) .$$

$\overline{\psi}_1$, then, is a prescribed function of r along the wall.

For the particular channel geometry considered, the $\theta = 0$ line is an axis of symmetry so that the shear stress must vanish along $\theta = 0$. Using the Sokolovski relations the shear stress is just

$$\overline{\tau}_{r\theta} = + (\overline{\sigma}_0 + \epsilon^2 \overline{\sigma}_1 + \cdots)(\sin\varphi)\sin(\pi + \pi\epsilon\overline{\psi}_1 + \pi\epsilon^3\overline{\psi}_2 + \cdots)$$

or

$$\overline{\tau}_{r\theta} = - (\overline{\sigma}_0 + \epsilon^2 \overline{\sigma}_1 + \cdots)\sin\varphi\sin(\pi\epsilon\overline{\psi}_1 + \pi\epsilon^3\overline{\psi}_2 + \cdots) .$$

Again expanding the sine function in a Taylor's series, the shear stress to order ϵ^1 becomes

$$\overline{\tau}_{r\theta} = - \overline{\sigma}_0(\sin\varphi)\pi\epsilon\overline{\psi}_1$$

but $\overline{\sigma}_0$ is a function of $\overline{\sigma}$ alone.[*] Thus, in order for the shear stress to vanish along $\overline{\theta} = 0$ the boundary condition for $\overline{\psi}_1$ must become $\overline{\psi}_1(\overline{r}, 0) = 0$. In summary, the boundary conditions for $\overline{\psi}_1$ are

$$\overline{\psi}_1(\overline{r}, \theta_w) = \frac{2}{\pi} \left(\frac{\tan\delta}{\epsilon}\right) f(r) \frac{1 + \sin\varphi}{2\sin\varphi}$$

$$\overline{\psi}_1(\overline{r}, 0) = 0$$

at the wall and centerline, respectively.

---

[*]The point will be discussed in detail in the consideration of the equation of motion.

Now consider the zeroth order series of equations

$$\frac{d\overline{U}_0}{d\overline{r}} + \frac{\overline{U}_0}{\overline{r}} = 0 \qquad \text{continuity}$$

$$0 = 0 \qquad \text{isotropy}$$

$$\frac{\partial \overline{\sigma}_0}{\partial \overline{\theta}} = 0 \qquad \theta \quad \text{equation of motion}$$

$$\frac{\partial \overline{\sigma}_0}{\partial \overline{r}} (1 - \sin\varphi) - \pi \sin\varphi \frac{\overline{\sigma}_q}{\overline{r}} \frac{\partial \overline{\psi}_1}{\partial \overline{\theta}} - 2\sin\varphi \frac{\overline{\sigma}_0}{\overline{r}} + 1$$

$$\text{r} \quad \text{equation of motion}$$

$$+ F_r^2 \overline{U}_0 \frac{d\overline{U}_0}{d\overline{r}} - \pi \sin\varphi \frac{\partial \overline{\sigma}_0}{\partial \overline{\theta}} \frac{\overline{\psi}_1}{\overline{r}} = 0 \quad .$$

For the condition that $\dfrac{\partial \overline{\sigma}_0}{\partial \overline{\theta}} = 0$, $\overline{\sigma}_0$ must be independent of $\overline{\theta}$.
Since all terms in the r equation of motion are independent of
$\overline{\theta}$ with the exception of $\dfrac{\overline{\sigma}_0}{\overline{r}} \dfrac{\partial \overline{\psi}_1}{\partial \overline{\theta}}$, $\overline{\psi}_1$ must be at most a linear
function of $\overline{\theta}$. However, from the previous paragraph, $\overline{\psi}_1(\overset{+}{\overline{r}}, 0)$
and $\overline{\psi}_1 (\overline{r}, \theta_w)$ are known,

$$\overline{\psi}_1(\overline{r}, 0) = 0$$

$$\overline{\psi}_1(\overline{r}, \theta_w) = \frac{2}{\pi} \left(\frac{\tan\delta}{\varepsilon} \right) f(r) \frac{1 + \sin\varphi}{2\sin\varphi}$$

where $f(r)$ is a prescribed function of r. Therefore, $\overline{\psi}_1$ must be
of the form

$$\overline{\psi}_1 = \overline{\psi}_1(\overline{r}, \theta_w) \overline{\theta} \quad . \qquad (2.3.19)$$

Thus, the zeroth order problem becomes

$$\frac{\partial \overline{\sigma}_0}{\partial \overline{\theta}} = 0$$

$$\overline{\psi}_1 = \overline{\psi}_1(\overline{r}, \theta_w) \overline{\theta}$$

(2.3.20)

$$\frac{d\overline{U}_0}{d\overline{r}} + \frac{\overline{U}_0}{\overline{r}} = 0$$

$$\frac{d\sigma_0}{d\overline{r}} (1 - \sin\varphi) - \pi \sin\varphi \frac{\overline{\sigma}_0}{\overline{r}} \overline{\psi}_1(\overline{r}, \theta_w) - 2\sin\varphi \frac{\overline{\sigma}_0}{\overline{r}} + 1 + F_r^2 \overline{U}_0 \frac{d\overline{U}_0}{d\overline{r}} = 0$$

with boundary conditions

$$\overline{\sigma}_0\left(\frac{R}{r_0}\right) = 0$$

and

$$\overline{\sigma}_0(1) = 0$$

for the upper and lower traction-free surfaces, respectively. It should be noted that the first order term ψ_1 appears in the zeroth order system of equations since, as seen from the complete r equation of motion, it influences both the zeroth order mean stress and the zeroth order radial velocity.

Before discussing the solution to the zeroth order system of equations, the equation for higher orders in ε will be listed. For order ε^1, the system becomes

$$\frac{1}{\overline{r}} \frac{\partial \overline{U}_1}{\partial \overline{\theta}} - 2\pi \Psi_1 \frac{d\overline{U}_0}{d\overline{r}} = 0 \qquad\qquad\qquad \text{isotropy}$$

$$-\pi\sin\varphi\left(\frac{d\overline{\sigma}_0}{d\overline{r}} + 2\,\frac{\overline{\sigma}_0}{\overline{r}}\right)\Psi_1 - \pi\sin\varphi\,\overline{\sigma}_0 \frac{\partial\overline{\Psi}_1}{\partial\overline{r}} \qquad\qquad (2.3.21)$$

$$-\pi^2\sin\varphi\,\frac{\overline{\sigma}_0}{\overline{r}}\,\overline{\Psi}_1 \frac{\partial\overline{\Psi}_1}{\partial\overline{\theta}}\,\overline{\theta} + \frac{1}{\overline{r}}\frac{\partial\overline{\sigma}_1}{\partial\overline{\theta}}(1+\sin\varphi) = 0 \qquad \begin{array}{l}\theta \quad \text{equation}\\ \quad \text{of motion}\end{array}$$

and for order ϵ^2

$$\frac{\partial\overline{u}_1}{\partial\overline{r}} + \frac{\overline{u}_1}{\overline{r}} + \frac{1}{\overline{r}}\frac{\partial\overline{v}_1}{\partial\overline{\theta}} = 0 \qquad\qquad\qquad \text{continuity}$$

$$\frac{\partial\overline{\sigma}_1}{\partial\overline{r}}(1-\sin\varphi) + \pi^2\sin\varphi\,\overline{\sigma}_0\overline{\Psi}_1\frac{\partial\overline{\Psi}_1}{\partial\overline{r}} - \pi\sin\varphi\frac{1}{\overline{r}}\overline{\Psi}_1\frac{\partial\overline{\sigma}_1}{\partial\overline{\theta}}$$

$$\qquad\qquad (2.3.22)$$

$$-\pi\sin\varphi\frac{\overline{\sigma}_1}{\overline{r}}\frac{\partial\overline{\Psi}_1}{\partial\overline{\theta}} - 2\frac{\overline{\sigma}_1}{\overline{r}}\sin\varphi - \frac{\overline{\theta}^2}{2} + F_r^2\left(\overline{U}_0\frac{\partial\overline{u}_1}{\partial\overline{r}} + \overline{u}_1\frac{d\overline{U}_0}{d\overline{r}}\right)$$

$$-\pi\sin\varphi\frac{\overline{\sigma}_0}{\overline{r}}\frac{\partial\overline{\Psi}_2}{\partial\overline{\theta}} = 0 \quad . \qquad\qquad \begin{array}{l}r \quad \text{equation}\\ \quad \text{of motion}\end{array}$$

The boundary condition for both the ϵ^1 and ϵ^2 order equation can only be discussed in a reasonable manner after considering the solution of the zeroth order system. The solution of the zeroth order system will now be considered.

$\overline{\Psi}_1(r, \theta_w)$ is a known function of r given by the Coulomb friction condition at the wall. Therefore, the zeroth order equations of continuity and r direction motion given in Eq. 2.3.20, represent a system of two equations for the determination of the radial velocity,

$\overline{U}_0$, and the mean stress, $\overline{\sigma}_0$. From continuity, the solution for the velocity must be of the form

$$\overline{U}_0 \propto \frac{1}{\overline{r}} \qquad (2.3.23)$$

Substituting this expression into the r- equation of motion, the equation for the mean stress becomes,

$$\frac{d\overline{\sigma}_0}{d\overline{r}} - \frac{2\sin\varphi}{1-\sin\varphi}\left(1+\frac{\pi}{2}\psi_1(\overline{r},\ \theta_w)\right)\frac{\overline{\sigma}_0}{\overline{r}} = \frac{1}{1-\sin\varphi}\left(\frac{F_r^2}{\overline{r}^3}-1\right)$$

The equation for $\overline{\sigma}_0$ is a first order, ordinary linear differential equation. An integrating factor, I, may be found as follows

$$I = \exp\left(\frac{-2\sin\varphi}{1-\sin\varphi}\right)\int\frac{1}{\overline{r}}\left(1+\frac{\pi}{2}\Psi_1(\overline{r},\ \theta_w)\right)d\overline{r}$$

Let

$$\omega(\overline{r},\ \varphi,\ \theta_w) = \frac{2\sin\varphi}{1-\sin\varphi}\int\frac{1}{\overline{r}}\left(1+\frac{\pi}{2}\Psi_1(\overline{r},\ \theta_w)\right)d\overline{r}\ \ ,$$

then $I = e^{-\omega}$. The equation for $\overline{\sigma}_0$ becomes

$$\frac{d}{d\overline{r}}(e^{-\omega}\overline{\sigma}_0) = \frac{1}{1-\sin\varphi}\left(Fr^2\frac{1}{\overline{r}^3}-1\right)e^{-\omega}$$

and the solution is written

$$\overline{\sigma}_0 = \frac{Fr^2}{1-\sin\varphi}e^{+\omega}\int e^{-\omega}\overline{r}^{-3}\,d\overline{r} - \frac{e^{+\omega}}{1-\sin\varphi}\int e^{-\omega}\,d\overline{r} + c_1e^{+\omega}$$

The Froude number, Fr, which contains the unknown average exit velocity and the integration constant, c_1, are evaluated by applying the homogenous boundary conditions at the upper and lower surfaces.

At the upper surface, $\overline{\sigma}\left(\dfrac{R}{r_0}\right) = 0$ leads to

$$c_1 = \frac{Fr^2}{1 - \sin\varphi} \int e^{-\omega-3} \, d\overline{r} \, \bigg|_{\overline{r} = \frac{R}{r_0}} - \frac{1}{1 - \sin\varphi} \int e^{-\omega} \, d\overline{r} \, \bigg|_{\overline{r} = \frac{R}{r_0}}$$

so that the solution may be written

$$\overline{\sigma}_0 = \frac{Fr^2}{1 - \sin\varphi} e^{+\omega} \int e^{-\omega-3} \, d\overline{r} \left[1 - \frac{\int e^{-\omega-3} \, d\overline{r} \big|_{\overline{r} = \frac{R}{r_0}}}{\int e^{-\omega-3} \, d\overline{r}} \right]$$

$$- \frac{e^{+\omega}}{1 - \sin\varphi} \int e^{-\omega} \, d\overline{r} \left[1 - \frac{\int e^{-\omega} \, d\overline{r} \big|_{\overline{r} = \frac{R}{r_0}}}{\int e^{-\omega} \, d\overline{r}} \right] \qquad (2.3.24)$$

The condition at the lower boundary leads to a unique value of the Froude number and hence a unique average exit velocity. Applying the lower boundary condition gives

$$Fr^2 = \frac{\int e^{-\omega} \, d\overline{r} \big|_{\overline{r} = 1} \left[1 - \dfrac{\int e^{-\omega} \, d\overline{r} \big|_{\overline{r} = \frac{R}{r_0}}}{\int e^{-\omega} \, d\overline{r} \big|_{\overline{r} = 1}} \right]}{\int e^{-\omega-3} \, d\overline{r} \big|_{\overline{r} = 1} \left[1 - \dfrac{\int e^{-\omega-3} \, d\overline{r} \big|_{\overline{r} = \frac{R}{r_0}}}{\int e^{-\omega-3} \, d\overline{r} \big|_{\overline{r} = 1}} \right]} \qquad (2.3.25)$$

and the average exit velocity is just

$$U^* = \sqrt{gr_0} \; Fr \qquad (2.3.26)$$

The mean stress is given by Eq. 2.3.24 with the Froude number given

by Eq. 2.3.25. The unique velocity field given by Eq. 2.3.23 and the stress field given by Eqs. 2.3.19, 2.3.24, and 2.3.25 represent a solution to the complete system of equations to order ϵ^0. It should be noted that the effects of cohesion, frictional channel walls, non-radial gravity, and traction-free upper and lower boundaries have been included.

Consider next the ϵ^1 order equations, namely

$$-\pi^2 \sin\varphi \left(\frac{d\overline{\sigma}_0}{d\overline{r}} + 2\frac{\overline{\sigma}_0}{\overline{r}} \right) \overline{\Psi}_1 - \pi\sin\varphi\overline{\sigma}_0 \frac{\partial\psi_1}{\partial\overline{r}}$$

$$-\pi^2 \sin\varphi \frac{\overline{\sigma}_0}{\overline{r}} \overline{\Psi}_1 \frac{\partial\overline{\Psi}_1}{\partial\overline{\theta}} + \overline{\theta} + \frac{1}{\overline{r}}\frac{\partial\overline{\sigma}_1}{\partial\overline{\theta}} (1 + \sin\varphi) = 0$$

and

$$\frac{1}{\overline{r}}\frac{\partial\overline{u}_1}{\partial\theta} - 2\pi\overline{\Psi}_1 \frac{d\overline{U}_0}{d\overline{r}} = 0$$

From the zeroth order set of equations,

$$\overline{\Psi}_1 = \overline{\Psi}_1(\overline{r}, \theta_w) \overline{\theta}$$

where $\overline{\Psi}_1(r, \theta_w)$ is a prescribed function of r,

$$\overline{U}_0 = \frac{1}{\overline{r}}$$

and

$$\overline{\sigma}_0 = S(\overline{r})$$

where $S(\overline{r})$ is the solution given by Eq. 2.3.24. From ϵ^1 order equation of isotropy

$$\frac{\partial \overline{u}_1}{\partial \overline{\theta}} = 2\pi \overline{\psi}_1(\overline{r}, \ \theta_w) \ \overline{\theta}\left(-\frac{1}{\overline{r}^2}\right)\overline{r}$$

and integrating with respect to $\overline{\theta}$ gives

$$\overline{u}_1 = -\pi \overline{\psi}_1(\overline{r}, \ \theta_w) \frac{\overline{\theta}^2}{\overline{r}} + K_1(\overline{r}) \qquad (2.3.27)$$

where $K_1(\overline{r})$ is an arbitrary function of $\overline{r}$.

The radial volumetric flow rate per unit depth, Q, at any location r is just

$$Q = 2 \int_0^{\theta_w} ru \, d\theta$$

or in dimensionless form

$$Q = 2\theta_w r_0 U* \int_0^1 \overline{ur} \, d\overline{\theta}$$

The problem considered above is for the steady flow of a frictional cohesionless solid through straight plane channels. Therefore the volumetric flow rate defined above must be independent of $\overline{r}$. For the zeroth order solution $\overline{U}_0 = \frac{1}{r}$, so that

$$Q_0 = 2\theta_w r_0 U* \int_0^1 \frac{1}{\overline{r}} \overline{r} \, d\overline{\theta} = 2\theta_w r_0 U* \qquad (2.3.28)$$

or in words, the constant zeroth order flow rate equals the product of the exit area and the average exit velocity.

The above argument can be used to evaluate the function $K_1(\overline{r})$. The perturbation volumetric flow rate, Q_1, associated with the perturbation radial velocity, $\overline{u}_1$, is just

$$Q_1 = \epsilon^2 Q_0 \int_0^1 \overline{u}_1 \overline{r} d\overline{\theta}$$

Substituting the expression for the perturbation velocity, $\overline{u}_1$, from Eq. 2.3.27 gives

$$Q_1 = \epsilon^2 Q_0 \left[\frac{-\pi}{3} \overline{\Psi}_1(\overline{r}, \ \theta_w) + \overline{r} \ K_1(\overline{r}) \right] \qquad (2.3.29)$$

The form of the function $\overline{\Psi}_1(\overline{r}, \ \theta_w)$ was determined from the Coulomb condition at the wall. Assume that the function $f(\overline{r})$ may be partitioned as follows

$$f(\overline{r}) = A + f_1(\overline{r})$$

where A is a constant independent of both $\overline{r}$ and $\overline{\theta}$. With this, the function $\overline{\Psi}_1(\overline{r}, \ \theta_w)$ may be written

$$\overline{\Psi}_1(\overline{r}, \ \theta_w) = \left(\frac{2}{\pi}\right) \frac{\tan\delta}{\epsilon} \left(\frac{1+\sin\varphi}{2\sin\varphi}\right)\left(A + f_1(\overline{r})\right)$$

Substituting this expression to Eq. 2.3.29, the perturbation flow rate becomes

$$Q_1 = \epsilon^2 Q_0 \left[\frac{-2}{3} \left(\frac{\tan\delta}{\epsilon}\right) \frac{1+\sin\varphi}{2\sin\varphi} \left(A + f_1(\overline{r})\right) + \overline{r} \ K_1(\overline{r}) \right] ,$$

In order for Q_1 to be independent of $\overline{r}$, $K_1(\overline{r})$ must be

$$K_1(\overline{r}) = \frac{2}{3} \left(\frac{\tan\delta}{\epsilon}\right) \frac{1+\sin\varphi}{2\sin\varphi} \frac{f_1(\overline{r})}{\overline{r}} \qquad *$$

so that the perturbation flow rate reduces to

---

*It has been assumed that terms of the form $\dfrac{\text{constant}}{\overline{r}}$ are not included in the function $K_1(\overline{r})$ since this represents the zeroth order solution.

$$Q_1 = -\frac{2}{3}\tan\delta(\epsilon)\frac{1+\sin\varphi}{2\sin\varphi}AQ_0 \tag{2.3.30}$$

Thus only the constant part of the function $\overline{\Psi}_1(\overline{r},\ \theta_w)$ along the wall affects the perturbation volumetric flow rate. The perturbation velocity, $\overline{u}_1$, becomes

$$\overline{u}_1 = -2(\frac{\tan\delta}{\epsilon})(\frac{1+\sin\varphi}{2\sin\varphi})(\frac{A}{\overline{r}}\ \overline{\theta}^2 + \frac{\overline{f}_1}{\overline{r}}(\overline{\theta}^2 - \frac{1}{3})) \tag{2.3.31}$$

The ϵ^1 order θ equation of motion can be solved for the partial derivative of $\overline{\sigma}_1$, with respect to $\overline{\theta}$,

$$\frac{\partial\overline{\sigma}_1}{\partial\overline{\theta}} = \frac{\pi\sin\varphi}{1+\sin\varphi}\left(\overline{r}\ \frac{d\overline{\sigma}_0}{d\overline{r}} + 2\overline{\sigma}_0\right)\overline{\Psi}_1 + \frac{\pi\sin\varphi}{1+\sin\varphi}\ \overline{\sigma}_0\overline{r}\ \frac{\partial\overline{\Psi}_1}{\partial\overline{r}}$$

$$+ \pi^2\frac{\sin\varphi}{1+\sin\varphi}\ \overline{\sigma}_0\overline{\Psi}_1\ \frac{\partial\overline{\Psi}_1}{\partial\overline{\theta}} + \frac{\overline{r}\ \overline{\theta}}{1+\sin\varphi}$$

Substituting the previously determined expressions for $\overline{\Psi}_1$ and $\overline{\sigma}_0$ into the θ equation of motion yields

$$\frac{\partial\overline{\sigma}_1}{\partial\overline{\theta}} = \frac{\pi\sin\varphi}{1+\sin\varphi}\left(\overline{r}\frac{d\overline{S}}{d\overline{r}} + 2\overline{S}\right)\overline{\Psi}_1(\overline{r},\ \theta_w)\ \overline{\theta} + \frac{\pi\sin\varphi}{1+\sin\varphi}\ \overline{S}\overline{r}\ \frac{d\overline{\Psi}_1(\overline{r},\ \theta_w)}{d\overline{r}}\ \overline{\theta}$$

$$+ \frac{\pi^2\sin\varphi}{1\sin\varphi}\overline{S}\overline{\Psi}_1^2(\overline{r},\ \theta_w)\ \overline{\theta} + \frac{\overline{r}\ \overline{\theta}}{1+\sin\varphi}$$

which may also be written

$$\frac{\partial \overline{\sigma}_1}{\partial \overline{\theta}} = \frac{\pi \sin\varphi}{1 + \sin\varphi} \left\{ \left(\overline{r} \frac{d\overline{S}}{d\overline{r}} + 2\overline{S} \right) \overline{\Psi}_1(\overline{r}, \theta_w) + \overline{S}\,\overline{r} \frac{d}{d\overline{r}} \overline{\Psi}_1(\overline{r}, \theta_w) \right.$$

$$\left. + \pi \overline{S} \overline{\Psi}_1^2(\overline{r}, \theta_w) + \frac{\overline{r}}{\pi \sin\varphi} \right\} \overline{\theta} \qquad (2.3.32)$$

Integrating the above expression with respect to θ gives

$$\overline{\sigma}_1 = \frac{\pi \sin\varphi}{1 + \sin\varphi} \left\{ \left(\overline{r} \frac{d\overline{S}}{d\overline{r}} + 2\overline{S} \right) \overline{\Psi}_1(\overline{r}, \theta_w) + \overline{S}\,\overline{r} \frac{d}{d\overline{r}} \overline{\Psi}_1(\overline{r}, \theta_w) \right.$$

$$\left. + \pi \overline{S} \overline{\Psi}_1^2(\overline{r}, \theta_w) + \frac{\overline{r}}{\pi \sin\varphi} \right\} \frac{\overline{\theta}^2}{2} + K_2(\overline{r})$$

where $K_2(\overline{r})$ is an arbitrary function of $\overline{r}$.

Consider the above expression for $\dfrac{\partial \overline{\sigma}_1}{\partial \overline{\theta}}$ along the upper, $\overline{r} = \dfrac{R}{r_0}$, and lower, $\overline{r} = 1$, surfaces. Along the upper surface Eq. 2.3.32 reduces to

$$\frac{\partial \overline{\sigma}_1}{\partial \overline{\theta}} \bigg|_{\overline{r} = \frac{R}{r_0}} = \frac{\pi}{1 + \sin\varphi} \left[\frac{d\overline{S}}{d\overline{r}} \bigg|_{\overline{r} = \frac{R}{r_0}} \Psi_1\left(\frac{R}{r_0}, \theta_w\right) + \frac{1}{\pi \sin\varphi} \right] \frac{R}{r_0} \qquad (2.3.33)$$

since $\overline{S}\left(\dfrac{R}{r_0}\right) = 0$. If it is desired to keep the upper surface a stress free surface, then choosing

$$\overline{\Psi}_1\left(\frac{R}{r_0}, \theta_w\right) = \frac{-1}{\pi \sin\varphi \dfrac{d\overline{S}}{d\overline{r}} \bigg|_{\overline{r} = \frac{R}{r_0}}} \qquad (2.3.34)$$

will ensure that the mean stress does not vary with $\overline{\theta}$ along the upper surface and choosing $K_2(\frac{R}{r_0}) = 0$ will keep the upper surface stress free. Since $S(\frac{R}{r_0}) = 0$ and S for $\overline{r} < \frac{R}{r_0}$ is positive, $\left. \frac{d\overline{S}}{d\overline{r}} \right|_{\overline{r} = \frac{R}{r_0}}$ must be less than zero. Therefore the condition given by Eq. 2.3.34 is for a positive value of $\overline{\Psi}_1(\frac{R}{r_0}, \theta_w)$.

Along the lower surface, however, Eq. 2.3.32 reduces to

$$\left. \frac{\partial \overline{\sigma}_1}{\partial \overline{\theta}} \right|_{\overline{r} = 1} = \frac{\pi}{1 + \sin\varphi} \left[\left. \frac{d\overline{S}}{d\overline{r}} \right|_{\overline{r} = 1} \overline{\Psi}_1(1, \theta_w) + \frac{1}{\pi \sin\varphi} \right]$$

where now $\left. \frac{d\overline{S}}{d\overline{r}} \right|_{\overline{r} = 1} > 0$. Thus, a positive value of $\overline{\Psi}_1(1, \theta_w)$ does not exist to make the lower surface a stress free surface. An alternate boundary condition might be attained by choosing

$$\overline{\Psi}_1(1, \theta_w) = 0 \qquad \text{i.o. } \sin 2\overline{\Psi} = 0 \qquad (2.3.35)$$
$$\qquad \qquad \qquad \qquad \tau_{r\theta} = 0$$

which ensures the lower surface to be shear stress free. Therefore choosing

$$\overline{\Psi}_1\left(\frac{R}{r_0}, \theta_w\right) = \frac{-1}{\pi \sin\varphi \left. \dfrac{d\overline{S}}{d\overline{r}} \right|_{\overline{r} = \frac{R}{r_0}}}$$

and

$$K_2\left(\frac{R}{r_0}\right) = 0$$

and

$$\overline{\Psi}_1(1, \theta_w) = 0$$

will keep the upper surface stress free and the lower surface shear

stress free to order ϵ^4.

B. Solution for Constant Wall Friction Angle

The ϵ^0 and ϵ^1 order equations for the particular case of constant wall friction angle will now be solved. For this case, $\overline{\Psi}_1(\overline{r}, \theta_w)$ becomes

$$\overline{\Psi}_1(\overline{r}, \theta_w) = \left(\frac{1 + \sin\varphi}{\pi \sin\varphi}\right)\left(\frac{\tan\delta}{\epsilon}\right) \neq \text{function of } \overline{r} \qquad (2.3.36)$$

with the boundary value of $\overline{\Psi}_1$ along the center line unchanged at

$$\overline{\Psi}_1(\overline{r}, 0) = 0 \qquad (2.3.37)$$

The solution to the continuity equation is unchanged; the velocity is just

$$\overline{U}_0 = \frac{1}{\overline{r}} \qquad (2.3.38)$$

Substituting this expression for the velocity into the zeroth order r equation of motion gives

$$\frac{d\overline{\sigma}_0}{d\overline{r}} - \frac{2\sin\varphi}{1 - \sin\varphi}\left(1 + \frac{\pi}{2}\overline{\Psi}(\overline{r}, \theta_w)\right)\frac{\overline{\sigma}_0}{\overline{r}} = \frac{1}{1 - \sin\varphi}\left(\frac{F_r^2}{\overline{r}^3} - 1\right) \qquad (2.3.39)$$

with $\overline{\Psi}_1(\overline{r}, \theta_w)$ given by Eq. 2.3.36. The integrating factor however now reduces to

$$I = \exp\left[-\frac{2\sin\varphi}{1 - \sin\varphi}\int\frac{1}{\overline{r}}\left(1 + \frac{\pi}{2}\frac{1 + \sin\varphi}{\pi\sin\varphi}\frac{\tan\delta}{\epsilon}\right)d\overline{r}\right]$$

or

$$I = \overline{r}^{\;\frac{-2\sin\varphi}{1 - \sin\varphi}\left(1 + \frac{\pi}{2}\frac{1 + \sin\varphi}{\pi\sin\varphi}\frac{\tan\delta}{\epsilon}\right)} \quad .$$

Define

$$\omega = \frac{2\sin\varphi}{1 - \sin\varphi} \left(1 + \frac{\pi}{2} \frac{1 + \sin\varphi}{\pi\sin\varphi} \frac{\tan\delta}{\epsilon}\right)$$

so that the r equation becomes, upon multiplication by the integrating factor,

$$\frac{d}{d\bar{r}} \left(\bar{r}^{-\omega}\bar{\sigma}_0\right) = \frac{1}{1 - \sin\varphi} \left(F_r^2 \frac{1}{\bar{r}^3} - 1\right) \bar{r}^{-\omega}$$

Integrating with respect to $\bar{r}$ gives

$$\bar{\sigma}_0 = \frac{F_r^2}{1 - \sin\varphi} \left(\frac{-1}{\omega + 2}\right) \frac{1}{\bar{r}^2} - \frac{\bar{r}}{1 - \sin\varphi} \left(\frac{1}{1 - \omega}\right) + c_1 \bar{r}^{+\omega}$$

The Froude number, F_r, which contains the unknown average exit velocity, and the integration constant, c_1, are evaluated by applying the homogenous boundary conditions at the upper and lower surfaces. At the upper surface, $\bar{\sigma}_0(\frac{R}{r_0}) = 0$ determines c_1,

$$c_1 = \frac{1}{1 - \sin\varphi} \left[\frac{F_r^2}{(\omega + 2)(\frac{R}{r_0})^2} + \frac{(\frac{R}{r_0})}{(1 - \omega)}\right] \left(\frac{R}{r_0}\right)^{-\omega}$$

so that the solution may be written

$$\bar{\sigma}_0 = \frac{-F_r^2}{(1 - \sin\varphi)(\omega + 2)\bar{r}^2} \left[1 - (\frac{r}{R})^{\omega + 2}\right] - \frac{\bar{r}}{(1 - \sin\varphi)(1 - \omega)} \left[1 - (\frac{r}{R})^{\omega - 1}\right] \quad (2.3.40)$$

The condition at the lower boundary leads to a unique value of the Froude number and hence a unique average exit velocity. Applying the

condition $\overline{\sigma}_0(1) = 0$ gives

$$F_r^2 = \frac{-(\omega+2)}{(1-\omega)} \left\{ \frac{1 - \left(\dfrac{r_0}{R}\right)^{\omega-1}}{1 - \left(\dfrac{r_0}{R}\right)^{\omega+2}} \right\} \qquad (2.3.41)$$

where

$$\omega = \frac{2\sin\varphi}{1 - \sin\varphi} \left[1 + \frac{\pi}{2} \frac{1 + \sin\varphi}{\pi\sin\varphi} \frac{\tan\delta}{\theta_w} \right] .$$

The average exit velocity for the ϵ^0 order system is determined by the Froude number

$$U* = \sqrt{gr_0} \ F_r \ . \qquad (2.3.42)$$

For the zeroth order solution, the mean stress, $\overline{\sigma}_0$ is given by Eq. 2.3.40 with the Froude number uniquely determined by Eq. 2.3.41. The mean stress vanishes at the upper and lower surfaces and its magnitude at any location, $\overline{r}$, is influenced by the following parameters; the effective angle of friction, φ, the wall friction angle, δ, the channel opening angle, θ_w, and the dimensionless material head ratio $\frac{R}{r_0}$.

Plots of mean stress versus position for an effective friction angle of $35°$ and a material head of 2 with wall friction angle treated as parameter are given in Fig. 2.3.3. The plot of mean stress versus position for $\delta = 0$ which corresponds to the "exact" solution given by Sullivan [95] for frictionless channel walls is also given. Similar plots for dimensionless head ratios of 5 and 10 are given in Figs. 2.3.4 and 2.3.5, respectively. Plots of mean stress versus position for an effective friction angle of $30°$ and material head ratios of 2, 5, and 10 with wall friction angle treated as parameter are given in Figs. 2.3.6, 2.3.7, and 2.3.8 respectively. Similar plots for an effective friction

angle of $25°$ are given in Figs. 2.3.9, 2.3.10, and 2.3.11.

For the channel geometry defined in Fig. 2.3.1, the channel opening at the exit, D, may be related to the exit radius, r_0, as follows

$$r_0 = \frac{D}{2\tan\theta_w} \quad .$$

The average zeroth exit velocity $U*$ given in Eq. 2.3.42 may be written

$$U* = \sqrt{gD} \; \frac{F_r}{\sqrt{2\tan\theta_w}}$$

or in dimensionless form

$$\frac{U*}{\sqrt{gD}} = \frac{F_r}{\sqrt{2\tan\theta_w}} \quad . \tag{2.3.43}$$

Thus, as in the case of the mean stress, the average dimensionless exit velocity depends on the parameters φ, δ, θ_w, and $\frac{R}{r_0}$. For an effective friction angle of $35°$ and a channel opening of $10°$, plots of average dimensionless exit velocity versus dimension head ratio with wall friction angle treated as parameter are given in Fig. 2.3.12. Similar plots for effective friction angles of $30°$ and $25°$ are given in Figs. 2.3.13 and 2.3.14, respectively. In all cases it is seen that for sufficiently large $\frac{R}{r_0}$, the average dimensionless exit velocity is independent of material head. This agrees with the well documented fact that exit velocity is independent of material head for sufficiently large $(\frac{R}{r_0})$.

For $(\frac{R}{r_0})$ large, the Froude number reduces to

$$F_r^2 = \frac{\omega + 2}{\omega - 1}$$

with

$$\omega = \frac{2\sin\varphi}{1 - \sin\varphi}\left[1 + \frac{\pi}{2}\frac{1 + \sin\varphi}{\pi\sin\varphi}\frac{\tan\delta}{\theta_w}\right].$$

Thus the dimensionless exit velocity in the head independent flow regime becomes

$$\frac{U^*}{\sqrt{gD}} = \sqrt{\frac{\omega + 2}{\omega - 1}}\ \frac{1}{\sqrt{2\tan\theta_w}}\ .$$

Plots of $\dfrac{U^*}{\sqrt{gD}}$ versus channel opening angle in the head independent flow regime for various values of wall friction angle are given in Fig. 2.3.15. The exit velocity derived analytically by Sullivan [95] is also shown. Similar plots for effective friction angles of $30°$ and $25°$ are given in Figs. 2.3.16 and 2.3.17, respectively.

Now consider the ϵ^1 order equation for the case of constant wall friction angle. From the zeroth order solution

$$\overline{\Psi}_1 = \left(\frac{1 + \sin\varphi}{\pi\sin\varphi}\right)\left(\frac{\tan\delta}{\theta_w}\right)\overline{\theta}$$

where $\overline{\Psi}_1$ is now independent of $\overline{r}$,

$$\overline{U}_0 = \frac{1}{\overline{r}}$$

and

$$\overline{\sigma}_0 = S(\overline{r})$$

with $S(\overline{r})$ the solution given in Eq. 2.3.40 to the zeroth order $\overline{r}$ equation of motion.

The ϵ^1 order θ equation of motion can be solved for the partial derivative of $\overline{\sigma}_1$ with respect to $\overline{\theta}$,

$$\frac{\partial \overline{\sigma}_1}{\partial \overline{\theta}} = \frac{\pi \sin\varphi}{1 + \sin\varphi} \left(\overline{r} \frac{d\overline{\sigma}_0}{d\overline{r}} + 2\overline{\sigma}_0 \right) \overline{\Psi}_1 + \frac{\pi \sin\varphi}{1 + \sin\varphi} \overline{\sigma}_0 \overline{r} \frac{\partial \overline{\Psi}_1}{\partial \overline{r}}$$

$$+ \frac{\pi^2 \sin\varphi}{1 + \sin\varphi} \frac{\overline{\sigma}_0}{\overline{r}} \overline{\Psi}_1 \frac{\partial \overline{\Psi}_1}{\partial \overline{\theta}} + \frac{\overline{r\theta}}{1 + \sin\varphi} \quad .$$

Substituting the previously determined expressions for $\overline{\Psi}_1$ and $\overline{\sigma}_0$ into the θ equation of motion yields

$$\frac{\partial \overline{\sigma}_1}{\partial \overline{\theta}} = \left(\overline{r} \frac{d\overline{S}}{d\overline{r}} + 2\overline{S} \right) \left(\frac{\tan\delta}{\theta_w} \right) \overline{\theta} + \frac{1 + \sin\varphi}{\sin\varphi} \overline{S} \left(\frac{\tan\delta}{\theta_w} \right)^2 \overline{\theta} + \frac{\overline{r\theta}}{1 + \sin\varphi}$$

which upon integrating with respect to $\overline{\theta}$ gives

$$\overline{\sigma}_1 = \left[\left(\overline{r} \frac{d\overline{S}}{d\overline{r}} + 2\overline{S} \right) \left(\frac{\tan\delta}{\theta_w} \right) + \left(\frac{1 + \sin\varphi}{\sin\varphi} \right) \overline{S} \left(\frac{\tan\delta}{\theta_w} \right)^2 + \frac{\overline{r}}{1 + \sin\varphi} \right] \frac{\overline{\theta}^2}{2} + K_2(\overline{r})$$

$K_2(\overline{r})$ will be taken as zero so that the perturbation mean stress along the θ axis will be zero. Thus, the perturbation stress becomes

$$\overline{\sigma}_1 = \left[\left(\overline{r} \frac{d\overline{S}}{d\overline{r}} + 2\overline{S} \right) \left(\frac{\tan\delta}{\theta_w} \right) + \left(\frac{1 + \sin\varphi}{\sin\varphi} \right) \overline{S} \left(\frac{\tan\delta}{\theta_w} \right)^2 + \frac{\overline{r}}{1 + \sin\varphi} \right] \frac{\overline{\theta}^2}{2} \qquad (2.3.44)$$

Define $\overline{S}_1(\overline{r}, \overline{\theta})$ as the solution to the ϵ^1 order θ equation of motion given in Eq. 2.3.44. Then the total dimensionless stress may be written

$$\overline{\sigma} = \overline{S}(\overline{r}) + \theta_w^2 \overline{S}_1(\overline{r}, \overline{\theta}) \qquad (2.3.45)$$

For a constant wall friction angle the perturbation stress $\overline{S}_1$, will not vanish at the upper and lower surfaces. Therefore the upper and lower surfaces for this case are free surfaces only to order ϵ^2. Along the upper surface the total stress becomes

$$\overline{\sigma}\left(\frac{R}{r_0}, \overline{\theta}\right) = \theta_w^2\, S_1\left(\frac{R}{r_0}, \overline{\theta}\right)$$

and along the lower surface the total stress becomes

$$\overline{\sigma}(1, \overline{\theta}) = \theta_w^2\, S_1(1, \overline{\theta})$$

The perturbation radial velocity which is obtained upon integrating the ϵ^1 order equation of isotropy is just

$$\overline{u}_1 = -\pi \left(\frac{1 + \sin\varphi}{\pi\sin\varphi}\right)\left(\frac{\tan\delta}{\theta_w}\right)\frac{\overline{\theta}^2}{r} + K_1(\overline{r}) \quad .$$

With the assumption of steady flow, $K_1(\overline{r}) = 0$ for the flow to be independent of $\overline{r}$ since $\overline{V}_1(\overline{r}, \theta_w)$ is independent of $\overline{r}^*$. Thus the perturbation radial velocity becomes

$$\overline{u}_1 = -\pi\left(\frac{1 + \sin\varphi}{\pi\sin\varphi}\right)\left(\frac{\tan\delta}{\theta_w}\right)\frac{\overline{\theta}^2}{r} \tag{2.3.46}$$

Substituting this velocity into the ϵ^2 order equation of continuity gives $\dfrac{\partial \overline{v}_1}{\partial \overline{\theta}} = 0$, which upon integrating with respect to $\overline{\theta}$ gives

$$\overline{v}_1 = K_3(\overline{r})$$

---

[*] It has been assumed that terms of the form $\dfrac{\text{constant}}{\overline{r}}$ are not included in $K_1(\overline{r})$ since this term represents the zeroth order solution.

However, $\overline{v}_1 \Big|_{\theta = \theta_w} = 0$ so that $K_3(\overline{r}) = 0$ and

$$\overline{v}_1 = 0 \quad . \tag{2.3.47}$$

Therefore, the perturbation velocity $\overline{u}$, gives rise to no perturbation circumferential velocity.

The total radial velocity, correct to order ϵ^2, may now be written

$$\overline{u} = \overline{U}_0 + \epsilon^2 \overline{u}_1$$

where

$$\overline{U}_0 = \frac{1}{\overline{r}}$$

and

$$\overline{u}_1 = -\pi \left(\frac{1 + \sin\varphi}{\pi \sin\varphi} \right) \left(\frac{\tan\delta}{\theta_w} \right) \frac{\overline{\theta}^2}{\overline{r}} \quad .$$

The dimensionless exit velocity is just

$$\overline{u} \Big|_{\overline{r} = 1} = 1 + \epsilon^2 (-\pi) \frac{1 + \sin\varphi}{\pi \sin\varphi} \frac{\tan\delta}{\theta_w} \overline{\theta}^2$$

and the average exit velocity just

$$\frac{1}{r_0 \theta_w} \int_0^{\theta_w} r_0 \left(\overline{u} \Big|_{\overline{r} = 1} \right) d\theta = \frac{\int_0^{\theta_w} r_0 d\theta}{r_0 \theta_w} - \epsilon^2 \frac{1 + \sin\varphi}{\sin\varphi} \frac{\tan\delta}{\theta_w} \frac{\int_0^{\theta_w} r_0 \overline{\theta}^2 d\theta}{r_0 \theta_w}$$

and performing the integration gives

$$\frac{1}{r_0 \theta_w} \int_0^{\theta_w} r_0 \left(\overline{u} \ \Big|_{\overline{r} = 1} \right) d\theta = 1 - \frac{2}{3} \frac{1 + \sin\varphi}{2\sin\varphi} \tan\delta \ \theta_w \quad .$$

Define the average total exit velocity, U^{**}, correct to order ϵ^2 as

$$U^{**} = \frac{U^*}{r_0 \theta_w} \int_0^{\theta_w} r_0 \left(\overline{u} \ \Big|_{\overline{r} = 1} \right) d\theta$$

so that

$$U^{**} = U^* \left[1 - \frac{2}{3} \frac{1 + \sin\varphi}{2\sin\varphi} (\tan\delta) \ \theta_w \right] \quad .$$

But

$$U^* = \sqrt{gD} \ \frac{F_r}{\sqrt{2\tan\theta_w}}$$

so that the total dimensionless exit velocity may be written

$$\frac{U^{**}}{\sqrt{gD}} = \frac{F_r}{\sqrt{2\tan\theta_w}} \left[1 - \frac{2}{3} \frac{1 + \sin\varphi}{2\sin\varphi} (\tan\delta) \ \theta_w \right] \quad . \qquad (2.3.48)$$

For $\dfrac{R}{r_0}$ large, the total dimensionless exit velocity reduces to the form

$$\frac{U^{**}}{\sqrt{gD}} = \sqrt{\frac{\omega + 2}{\omega - 1}} \frac{1}{\sqrt{2\tan\theta_w}} \left[1 - \frac{2}{3} \frac{1 + \sin\varphi}{2\sin\varphi} (\tan\delta) \ \theta_w \right] \quad . \qquad (2.3.49)$$

Plots of $\dfrac{U^{**}}{\sqrt{gD}}$ versus channel opening angle for an effective friction angle of $35°$ with wall friction angle treated as parameter are given in Fig. 2.3.18. Similar plots for effective friction angles of $30°$ and $25°$ are given in Figs. 2.3.19 and 2.3.20, respectively.

The effect of the first order solution on the results may be seen from Fig. 2.3.21. In this figure $\dfrac{U^*}{\sqrt{gD}}$ and $\dfrac{U^{**}}{\sqrt{gD}}$ are plotted versus opening angle for an effective friction angle of $35°$ with the wall friction

angle being treated as a parameter.

Velocity profiles at the exit plant, mass flow rate, and mean stress acting along the channel walls are compared with experimental results.

Bosley, et al, [32] conducted an experimental investigation of granular discharge from model hoppers. Photographic measurements were made of particle exit velocities at various angular locations across the exit plane. Experimental results in the form of measured particle velocity at various angular positions for sand with an effective friction angle of $35°$ and a hopper opening angle of $32\frac{1}{2}°$ are given in Fig. 2.3.22.[*] Also shown are plots of dimensionless exit velocity $\overline{u}_{r\,=\,1}$, given by the perturbation solution, versus angular position $\overline{\theta}$ for wall friction angles of $10°$ and $20°$. Also shown is the dimensionless velocity for the radial body force solution given by Sullivan [95] which corresponds to a wall friction angle of $0°$. It is seen that the perturbation solution predicts the correct trend in the exit velocity in regard to the variation of exit velocity with angular position. Also for $\delta = 15°$ which corresponds to measured values of wall friction angle for sand on plexiglass (see Appendix B,) the perturbation solution predicts the correct magnitude of the dimensionless exit velocity. Data collected by Bosley, et al, [32] for gravel with $\varphi = 40$ is presented in Fig. 2.3.23. Also shown is the dimensionless exit velocity for wall friction angles of $10°$ and $20°$, and the radial body force solution.

---

[*]The measured particle velocity is made dimensionless be dividing by $\sqrt{gD}$ where D is the experimental hopper opening taken from Bosley, et al, [32].

Several investigators [7, 8, 14, 15, 32, 95] have determined experimentally the variation in mass flow rate, expressed here as average dimensionless exit velocity, with channel opening angle. Experimental results for an effective friction angle of 35° are given in Fig. 2.3.24. Also shown are plots of average dimensionless exit velocity versus opening angle for various values of wall friction angle. Similar results for an effective friction angle of 25° are given in Fig. 2.3.25. Again it is seen that the perturbation solution predicts the correct trend in and the correct magnitude of the experimental data. Hence, the solution should prove useful in predicting mass flow rates of frictional, cohesive materials from plane channels as a function of the flow parameters and system geometry.

Measurements have been made of the mean stresses along the walls in converging channels [38, 51]. Experimental results in the form of mean pressure versus position from the hopper outlet are presented in Fig. 2.3.26 for a 25° channel opening angle. Also shown are plots of mean stress predicted by the perturbation solution as a function of position for various values of wall friction angle. In the region of the exit plane, the solution gives an accurate prediction of the trend in the mean stress, in regard to the variation in mean stress with position from the outlet, and the correct magnitude of the mean stress.

CHAPTER III – FLOW SEPARATION FOR A CYLINDRICAL SECTION

1. Introduction

Chapter 3 deals specifically with the problem of predicting the point of separation for the transverse flow of a granular material over a cylindrical section. Information on this separation point will be of importance in assessing the heat transfer from a cylinder and will also be required for any future work on analyzing the velocity and temperature fields around a cylinder.

As discussed in Chapter 1, the size of the stagnant and cavity regions may be greatly reduced by choosing more streamlined tube shapes [107], but the added difficulty and cost in manufacturing non-circular heat exchanger tubes does not usually make this an attractive solution. Therefore, the study of flow separation for circular cylinders is pertinent.

2. Dimensional Analysis

Prior to the start of any experiments, a brief dimensional analysis of the problem was made. This was done in order to determine what the pertinent parameters might be. These parameters are then to be used in planning the experiments as well as in interpreting the results.

The separation point is defined as the point of contact of the

last particle in contact with the cylinder. The separation angle, θ_S, is the angle between the longitudinal axis passing through the centroid of the cylinder and line passing through the cylinder centroid and the separation point. The particle diameter, the tube diameter, the channel opening, and the material head above the cylinder centroid are designated by D_P, D_T, D_G, and D_H, respectively.

In Chapter II it was shown that the material exit velocity for the flow of a cohesionless, frictional material from plane channels is independent of material head as long as the head is sufficiently large. For real channels with a wall friction angle of around 10 degrees, head independent flow is attained for a dimensionless head, $\dfrac{R}{r_o}$, of approximately 5, where R and r_o are the radii to the upper and lower free surfaces, respectively. For most industrial applications a large supply hopper, corresponding to a large material head, is located upstream of any heat exchanger so that the flow, in general, is head independent. Thus, for a proper experimental design, D_H should not affect the separation point and need not be considered in any proposed correlation.

The remaining quantities which are most likely to influence the separation angle may then be listed as follows

$$\theta_S = f_1(g, \rho, U, \ D_P, D_T, D_G, \varphi, \delta)$$

where φ is the internal friction angle and δ is the wall friction angle

between the granular material and the cylinder surface. From these quantities a set of dimensionless groups may be formed, and the separation angle may be expressed as a function of these groups by writing

$$\theta_S = f_2\left(\frac{\rho U^2}{\rho g D_T} , \frac{D_P}{D_T} , \frac{D_P}{D_G} , \varphi , \delta\right) \tag{3.2.1}$$

These parameters are to be used both in planning and in interpreting the experiments.

It should be mentioned that in the above development the void ratio was tacitly omitted from consideration. This quantity is defined as the ratio of the volume of the voids to the volume of the solids in a unit volume of material. For a random packing of spherical particles this ratio is independent of particle diameter. In addition, for the sand used in the present experiments the void ratio is approximately equal to that for the spherical particles. These conditions lead to the justification for excluding the void ratio from the list of variables.

3. Experimental Apparatus

The experimental apparatus, shown in Fig. 3.3.1, has three basic parts; (1) the supply hopper, (2) the test section, and (3) the gate valve.

The volume of the supply hopper is determined by two requirements. First, the volume of the supply hopper must be large compared

to the volume of the test section to ensure head independent flow.
Second, the volume of the supply hopper must be large enough to pro-
vide continuous, head-independent flow at a constant flow rate for a
time large compared to the time required in the measurement of the
separation angle. For the purpose of this investigation the supply hop-
per shown in Fig. 3.3.1 is entirely adequate.

The test section was constructed of plexiglass so that the flow
could be viewed during approach and departure from the cylinder.
The front and back plexiglass sections at the test section can be re-
moved to change the test cylinder. Plexiglass inserts were construct-
ed so that the channel opening could be varied independently. Channel
openings of 2.688, 1.98, and 1.44 inches are possible.

Five different diameter aluminum and lucite cylinders with
diameters of 1/2, 3/4, 1, 1 1/4, and 1 1/2 inches were constructed.
Both aluminum and lucite cylinders were constructed to represent
cylinders with different surface friction angles.

The gate valve consists of a moveable panel resting against a
rubber membrane. The position of the panel may be adjusted to pro-
duce the desired mass flow rate in the upstream channel. Velocities
of the order of .05 to 1.0 inches per second can be attained. The
lower limit is that value below which steady flow without clogging can-
not be maintained; the upper limit is that value above which

discontinuous flow may occur.

The separation angle is measured by taking a photograph of the lower half of the cylinder and the cavity. The photographic arrangement consists of a large optical bench, a support panel for the camera, and a single lens reflex camera equipped with an extension tube for high magnification. The camera support panel may be adjusted vertically to align the camera with the cavity below the cylinder. The cavity photograph is taken at 10X to aid in the measurement of the separation angle.

4. Measurement Technique

A photograph of the flow of 0.023 inch diameter glass beads (P-0280) over a 1 1/4 inch diameter lucite cylinder is shown in Fig. 3.4.1a. A close-up, high magnification photograph of the separation point is given in Fig. 3.4.1b. On each cylinder rays were very accurately inscribed at 10° intervals. These rays appear as heavy black lines in the photograph. Two additional lines have been drawn in on Fig. 3.4.1b. One line passes through the centroid of the cylinder and extends on the direction of the flow; one line passes through the centroid of the cylinder and the separation point.

For each condition defined by material, approach velocity, and system geometry, i.e., channel opening, tube diameter, etc., a single photograph is taken. The film is developed and an 8 inch X 10 inch print

made. The angle measurement technique consists of constructing the two lines discussed above and then determining the magnitude of the angle from 10° markings on the cylinder. The separation angle used in the correlation was the arithmetic mean of the left and right hand side separation angles on each photograph.

The gate valve used for controlling the mass flow rate in the channel is not calibrated. The mass flow rate for any setting is determined by weighing the net mass output in a fixed time. The mass flow rate is then converted to approach velocity by dividing by channel area and material bulk density. The error involved in using this technique for determining approach velocity is usually less than 10% [9]. It should be noted that for each flow condition two measurements of mass flow rate are made. The mass flow rate recorded is the mean value of the two measured flow rates.

5. Procedure

As discussed in Section 2, the separation angle may be expressed as a function of five dimensionless groups; the Froude number based on cylinder diameter $(U/\sqrt{gD_T})$, the particle to cylinder diameter ratio, the particle diameter to channel opening ratio, the internal friction angle, and the cylinder surface friction angle. The functional relation may be written

$$\theta_S = f_2\left(\frac{U}{\sqrt{gD_T}} \ , \ \frac{D_P}{D_T} \ , \ \frac{D_P}{D_G} \ , \ \varphi, \delta\right) \quad \text{as shown earlier.}$$

For a given granular medium, cylinder material (aluminum or lucite), cylinder diameter, and channel opening, all of the dimensionless groups in the above relation are fixed with the exception of the Froude number. Hence under these conditions, the variation of separation angle with approach velocity may be investigated.

The test procedure for this investigation may be described as follows. The gate valve is closed and the test section and supply hopper are filled with the granular material. The gate valve is then opened and a constant mass flow rate established. After approximately 5 minutes, the mass flow rate is determined as described in the previous Section. A photograph centered on the cavity below the cylinder is then taken. Next, the gate valve is adjusted to give a new flow rate, and after a second 5 minute interval, the above procedure of flow rate measurement and cavity photograph are repeated. For each material it is possible to take approximately 5 photographs at different, increasing flow rates before the supply hopper must be replenished.

In the actual test, a minimum of 20 and a maximum of 60 photographs were taken, each photograph at a different mass flow rate, for each combination of granular medium, cylinder material, cylinder diameter, and channel opening. Having completed this procedure

describing the effect of approach velocity on separation angle for one condition of material and geometry, the front Plexiglass panel on the flow apparatus is removed, a different diameter cylinder secured in the test section, the panel replaced, and a second set of 20 to 60 photographs, each at a different flow rate, are taken. This procedure is repeated in turn until a set of 20 to 60 photographs is obtained for each of the five cylinder diameters. Two sets of photographs were required at each diameter since both aluminum and lucite cylinders were used. This procedure which generates 10 sets of photographs for a given material was repeated for each of the granular materials investigated.

To investigate the effect of channel opening on separation angle the following procedure was adopted. The first set of Plexiglass inserts described in Section 3 which reduce the channel opening from 2.68 inches to 1.98 inches are installed in the test section, a test cylinder is secured in the test section, the front Plexiglass panel replaced, and the gate valve closed. The test section and supply hopper are then filled with the chosen granular material and the gate valve opened to produce a constant flow rate. A photograph centered on the cavity below the cylinder is taken.

In the actual test, 20 photographs were taken each at a different flow rate for each cylinder diameter for both the aluminum and

lucite cylinder. This procedure was repeated for each of the granular materials. The second set of Plexiglass inserts reducing the channel opening to 1.44 inches were installed and the entire procedure des- cribed above repeated. Prints (8" × 10") were made of each of the cavity photographs. The measurement technique for the separation angle described in Section 4 was followed. The information giving the value of each of the five dimensionless groups and the corresponding measured separation angle was recorded on computer data cards for analysis. Additional separation angle measurements were made for several arbitrary combinations of material and system geometry as a check on measurement repeatibility.

6. Granular Materials Investigated

As described in Section 2 the proposed expression relating separation angle and the dimensionless flow parameters, Eq. 3.2.1, is valid for particles with near the same critical void ratio.

A total of nine granular materials were used. Five of these consisted of different sizes of spherical glass beads ranging in dia- meter from 10.7 mils to 127.2 mils. Fine, medium and coarse grain quartz sand were also used. Mustard seed (hard, ellipsoidal-shaped particles) was chosen to represent a material with a low thermal

diffusivity[*].

For the experiments performed, certain physical and mechanical properties of these materials were required. The physical properties include bulk and particle specific gravity, void ratio, and particle size. The mechanical properties include internal and wall friction angle. The determination of these material properties is described in Appendix B. The physical and mechanical properties are summarized in Table B-1.

7. Results, Discussion of Results, Conclusions

From an initial analysis of the data on the separation angle, it was observed that the separation angle may be expressed by the following function of the dimensionless groups

$$\theta_S = a_1 \left(\frac{U}{\sqrt{g D_T}} \right)^{a_2} \left(\frac{D_P}{D_T} \right)^{a_3} \left(\frac{D_P}{D_G} \right)^{a_4} + a_5 \varphi \tag{3.7.1}$$

where the constants, a_i, are found to be

$$a_1 \cong -25. \ , \ a_2 \cong 1.0 \ , \ a_3 \cong -1.5 \ , \ a_4 \cong 1.0 \ , \ a_5 \cong 0.90 \ .$$

It is seen from the value of the exponents of the product terms, the above relation may be simplified to give

---

[*] A material with a low thermal diffusivity is important for the experiment described in Chapter IV.

$$\theta_S = b_1 \left(\frac{U}{\sqrt{gD_P}} \right)^{b_2} \left(\frac{D_T}{D_G} \right)^{b_3} + b_4 \varphi \quad . \qquad (3.7.2)$$

The values of the constants b_i that best describe the complete set of separation angle data for all materials investigated are

$$b_1 = -16.9 \ , \ b_2 = 1.43 \ , \ b_3 = 0.98 \, , \ b_4 = 0.78 \quad .$$

The Froude number based on particle diameter is just

$$F_r = \frac{U}{\sqrt{gD_P}} \qquad (3.7.3)$$

where, as discussed earlier, U is the mean approach velocity. Define the modified Froude number, F_r^*, as

$$F_r^* = \left(\frac{U}{\sqrt{gD_P}} \right)^{b_2} \left(\frac{D_T}{D_G} \right)^{b_3} \qquad (3.7.4)$$

so that the above correlation may be written

$$\theta_S = b_1 F_r^* + b_4 \varphi \quad . \qquad (3.7.5)$$

The experimental results for the 23 mil diameter glass beads (P-0280) is presented in the form θ_S versus modified Froude number in Fig. 3.7.1. The intercept at $F_r^* = 0$ is just a constant times the internal friction angle for the material. The data for the other mate-rials may be presented in the same manner with different intercepts

resulting from the different internal friction angles for the various materials.

It is seen that the above correlation, given by Eq. 3.7.5, describes the variation of separation angle with flow parameter equally well for flow over aluminum and lucite cylinders. That is, the variation in measured separation angle resulting from a variation in surface friction is within experimental scatter. Therefore Eq. 3.7.5 describes variation of the separation angle with flow parameters for the flow of granular materials over lucite and aluminum cylinders with moderate surface friction angles.

The proposed correlation, Eq. 3.7.5, may be given the following physical interpretation. As the mass flow rate of the granular material approaches zero, the separation angle is given as a constant, less than one, times the internal friction angle alone. It is seen from geometry that the separation angle, θ_S, is equal to an angle which could be thought of as the angle of repose of the small pile formed below the cylinder. Thus, for vanishing flow velocity the separation angle should be given by the angle of repose, which as discussed by Taylor [86], is smaller than, but close to, the internal friction angle of the material.

As the flow velocity increases from zero, the mean pressure in the granular material increases allowing the flow to remain

"attached" to the cylinder longer. Thus, the separation angle should decrease slightly as the mean approach velocity increases. This description and the above correlation should be valid as long as the flow is continuous. If the modified Froude number becomes too large, i.e., the channel opening D_G becomes so small that the gap between the cylinder and wall behaves as an orifice, the flow will separate around $\theta_S = 90°$, and continue past the cylinder in free fall. Under these conditions the flow is no longer continuous since a large void region will occur extending across the entire channel below the cylinder.

A comment should also be made regarding the stagnant region. No systematic investigation of this region was made but it has been observed that a stagnant region does develop under certain circumstances. It has been found that this region is relatively insensitive to flow velocity but is greatly influenced by mean particle size. In fact, for particles with mean diameters greater than 20 mils the region seems to disappear completely [95, 107]. From qualitative observations made during the initial stages of this investigation it was concluded that the size of the stagnant region depends on both the mean particle size and the surface friction angle between the particles and cylinder surface. For example, for the glass beads (see Appendix B for material properties) flowing over either the lucite or aluminum

cylinders the stagnant region was never greater than 3 particle diameters. For the fine-grained sand (sand No. 1), however, a large stagnant region as may be seen in Fig. 3.1.3 was observed.

CHAPTER IV
TEMPERATURE PROFILES IN THE WAKE OF A HEATED CYLINDER

1. Introduction

Chapter IV deals specifically with the problem of determining the size and character of the wake of a heated cylinder in the transverse flow of a granular material. Some prior work on this type of problem has been done in connection with flow over a tube bundle [127]. However, it seems that the more basic problem concerning the region downstream of a single tube has not been treated so far. The spreading of the temperature in the wake will be an important factor in the design of granular heat exchangers as it will give an indication of the distance required to obtain a relatively uniform temperature increase throughout the medium.

The problem was approached experimentally and an apparatus was constructed for the purpose of determining the spanwise temperature profile at three locations downstream of a heated tube. The primary variables were the tube diameter, the granular material properties, the heat input and the mean approach velocity. Two different diameter heated tubes and three granular materials were investigated.

To obtain some additional understanding of the variables governing the temperature distribution in the wake an analytical solution is developed for the very simple case of a line source in two-dimensional, uniform flow of a one-component continuum.

2. Continuum Solution

The problem to be considered is that of a line source in the two dimensional, steady, uniform flow of a one-component continuum.

For the velocity field

$$\underline{u} = U\underline{i} + 0\underline{j} \qquad (4.2.1)$$

where $U =$ constant and $\underline{i}$ and $\underline{j}$ are unit vectors in $+x$ and $+y$ directions, respectively, the energy equation given by

$$\rho c \frac{DT}{Dt} = -P\nabla \cdot \underline{u} + \Phi + k\nabla^2 T$$

where $\frac{D}{Dt}$ is the substantial derivative, ∇ is the del operator, and Φ is the dissipation function, reduces to

$$\rho c U \frac{\partial T}{\partial x} = k\nabla^2 T \quad . \qquad (4.2.2)$$

The boundary conditions are

$$(1) \quad q = \lim_{r \to 0} -k \oint r \frac{\partial T}{\partial r} d\theta \quad \text{at} \quad r = 0$$

where q is the source strength per unit depth, and

$$(2) \quad T = T_0 \quad \text{at} \quad x \to \infty \quad \text{or} \quad y \to \infty \quad .$$

Define a dimensionless temperature, T^*, as

$$T^* = \frac{T - T_0}{T_0},$$

so that the energy equation may be written

$$\frac{\rho c U}{k} \frac{\partial T^*}{\partial x} = \nabla^2 T^* \qquad (4.2.3)$$

and condition (2) is replaced by the homogenous boundary condition

$$T* = 0 \quad \text{at} \quad x \to \infty \quad \text{or} \quad y \to \infty \quad .$$

The solution to 4.2.3 is of the following form [130]

$$T* = e^{ax} \Omega \quad . \tag{4.2.4}$$

Substitution of Eq. 4.2.4 into the energy Eq. 4.2.3 yields

$$\frac{\rho C U}{k} \left\{ a e^{ax} \Omega + e^{ax} \frac{\partial \Omega}{\partial x} \right\} = a^2 e^{ax} \Omega + 2 a e^{ax} \frac{\partial \Omega}{\partial x} + e^{ax} (\nabla^2 \Omega)$$

which reduces to

$$\nabla^2 \Omega - a^2 \Omega = 0 \tag{4.2.5}$$

for

$$a = \frac{\rho C U}{2k} \quad . \tag{4.2.6}$$

Since the boundary condition at $r = 0$ is independent of θ, Ω is independent of θ and Eq. 4.2.5 becomes an ordinary differential equation, namely

$$\frac{d^2 \Omega}{dr^2} + \frac{1}{r} \frac{d\Omega}{dr} - a^2 \Omega = 0 \quad .$$

In terms of dimensionless radial position $\bar{r}$ defined as

$$\bar{r} = \frac{r}{L}$$

the above equation may be written

$$\frac{d^2 \Omega}{d\bar{r}^2} + \frac{1}{\bar{r}} \frac{d\Omega}{d\bar{r}} - \frac{1}{4} Pe^2 \Omega = 0 \tag{4.2.7}$$

where Pe is the Peclet number defined as

$$Pe = \frac{\rho C U L}{k} \quad . \tag{4.2.8}$$

Now consider the boundary conditions for the variable Ω.
Boundary condition (2) becomes simply

$$\Omega = 0 \quad \text{at} \quad r \to \infty \ .$$

Boundary condition (1) may be written

$$q = \lim_{r \to 0} \left\{ -k \oint T_0 r \frac{\partial}{\partial r} (e^{r \cos \theta} \Omega) d\theta \right\}$$

which upon performing the differentiation becomes

$$q = \lim_{r \to 0} \left\{ -k \oint T_0 r e^{r \cos \theta} (\Omega \cos \theta + \frac{d\Omega}{dr}) d\theta \right\} \ .$$

Expanding the exponential term, $e^{r \cos \theta}$, in a Taylor's series, about the origin, integrating the series term by term and then taking the limit of the resulting expression as $r \to 0$ gives

$$q = \lim_{r \to 0} \left(-kT_0 2\pi r \frac{d\Omega}{dr} \right) \ .$$

Thus the problem may be written

$$\frac{d^2\Omega}{d\bar{r}^2} + \frac{1}{\bar{r}} \frac{d\Omega}{d\bar{r}} - \frac{1}{4} Pe^2 \Omega = 0 \tag{4.2.9}$$

with boundary conditions

$$(1)^1 \quad q = \lim_{\bar{r} \to 0} \left(-2\pi kT_0 \bar{r} \frac{d\Omega}{d\bar{r}} \right) \quad \text{at} \quad \bar{r} \to 0$$

and

$$(2)^1 \quad \Omega = 0 \quad \text{at} \quad \bar{r} \to \infty \ .$$

Equation 4.2.9 is in the form of a modified Bessel equation so that the solution is given by

$$\Omega = C_1 I_0(\tfrac{1}{2} Pe \, \bar{r}) + C_2 K_0(\tfrac{1}{2} Pe \, \bar{r}) \ . \tag{4.2.10}$$

Applying the boundary condition $(2)^1$ it is seen that

$$C_1 = 0$$

so that the solution reduces to

$$\Omega = C_2 K_0 (\tfrac{1}{2} Pe\,\bar{r}) \ . \tag{4.2.11}$$

Applying boundary condition $(1)^1$ gives an expression for determining C_2, namely,

$$q = \lim_{\bar{r} \to 0} C_2 \left\{ 2\pi\,k\,T_0\,\bar{r}\,K_1(\tfrac{1}{2} Pe\,\bar{r}) \cdot \tfrac{1}{2} Pe \right\} \quad *$$

which for small values of $\tfrac{1}{2} Pe\,\bar{r}$ reduces to

$$q = C_2 2\pi\,k\,T_0 \lim_{\bar{r} \to 0} \left\{ \bar{r}\ \frac{1}{\frac{1}{2}Pe\,\bar{r}}\ \tfrac{1}{2} Pe \right\} \quad ** \ .$$

Thus, the constant C_2 becomes

$$C_2 = \frac{q}{2\pi\,k\,T_0} \ . \tag{4.2.12}$$

Therefore, the temperature distribution may be written

$$T^* = \frac{q}{2\pi\,k\,T_0}\,e^{\frac{1}{2} Pe\,\bar{r}\cos\theta}\,K_0(\tfrac{1}{2} Pe\,\bar{r}) \tag{4.2.13}$$

and the dimensionless temperature profile, $\dfrac{2\pi\,k(T-T_0)}{q}$, which results from the line source is

$$\frac{2\pi\,k(T-T_0)}{q} = e^{\frac{1}{2} Pe\,\bar{r}\cos\theta}\,K_0(\tfrac{1}{2} Pe\,\bar{r}) \tag{4.2.14}$$

---

* Use has been made of the identity $\dfrac{d}{dx} K_0(x) = -K_1(x)$.

** Use has been made of the relation $K_1(x) \cong \dfrac{1}{x}$ for small x.

This analytical expression (4.2.14) can, of course, not be expected to agree exactly with the experimental measurements as the analytical model is a greatly simplified one. The solution suggests, however, that a single parameter may be used to present the experimental results and should indicate the behavior of the wake qualitatively. For this reason the analytical results are compared with those obtained by measurements.

3. Experimental Investigations

A. Plan of Experiments

The continuum solution developed in Section 2 indicates that the dimensionless temperature profile, $\dfrac{2\pi \, k(T-T_0)}{q}$, at a particular downstream location depends on a single parameter, the Peclet number defined as

$$Pe = \frac{UL}{\alpha}$$

where α is the bulk thermal diffusivity, U the mean approach velocity, and L a reference length taken as the heated cylinder diameter in the flow experiments. The experiments were designed so that the temperature in the wake could be measured for a reasonably wide range of Peclet numbers.

Medium-size spherical glass beads, coarse grain sand, and mustard seed, which represent granular materials with different thermal diffusivities, were chosen as the test materials. For each material a temperature profile is determined at three downstream locations for three flow velocities. For the coarse grain sand these velocities are approximately 0.10, 0.20, and 0.30 inches per second

which correspond to Peclet numbers of 200, 400 and 600. The three flow velocities for the glass beads and mustard seed are chosen so as to give Peclet numbers of 200, 400 and 600 also.

In the experimental apparatus, the power supplied to the heated cylinder per cylinder length is related to the source strength, q, in the continuum solution. For the coarse grain sand, the power supplied per cylinder length for the low, medium and high Peclet numbers are 100, 140 and 180 watts/ft., respectively.

Two different diameter heated cylinders, .375 and .750 inches, were used in the experiments. Temperature profiles were determined at three downstream locations for Peclet numbers of 200, 400 and 600 for each of the three granular materials.

B.   Experimental Apparatus

The experimental apparatus, shown in Fig. 3.3.1, has already been described in detail in Chapter III, Section 3..

Certain modifications, however, were made for the present experiments. Two different diameter, Cal-Rod, electrically heated cylinders were used. Concentric Plexiglass spacers, which fit flush with the inside channel surface, were constructed to hold the different diameter cylinders in position. Concentric insulation spacers were also constructed to be positioned between the heated cylinder and Plexiglass to minimize heat losses through the cylinder ends. The cylinders are heated with a variable AC source with the power supplied being measured.

Downstream temperature profiles are measured with a Bake-
lite thermocouple probe equipped with 5 copper-constantan thermo-
couples at $\frac{1}{2}$ inch spacing. The probe may be positioned at $1\frac{1}{2}$, 3 and
$4\frac{1}{2}$ inches below the centerline of the heated cylinder. The probe may
also be adjusted to shift the overall spanwise position of the five
thermocouples. A similar probe, equipped with a single thermo-
couple, is positioned 6 inches upstream of the cylinder to serve as a
free stream reference.

To determine the power dissipated in the cylinders the voltage
across the heater circuit is measured by a true RMS voltmeter and
this along with the known heater resistance serves to determine the
power dissipated. In addition, a 250-watt full scale watt meter is
connected in the heater circuit to provide a continuous reading of the
power supplied.

The five thermocouples in the lower thermocouple probe are
referenced to the single thermocouple far upstream of the heated
cylinder. Thus the measured potentials are proportional to the tem-
perature difference between the free stream flow and the wake. The
potentials are measured with a sensitive voltmeter with an error less
than 5%.

The mass flow rate is determined by weighing the net mass
output in a fixed time. The mass flow rate is then converted to
approach velocity by dividing by channel area and material bulk den-
sity. The error involved in using this technique for determining
approach velocity is usually less than 10% [9]. It should be noted
that for each flow condition at least two measurements of mass flow

rate are made. The mass flow rate recorded is the mean value of the measurements made.

C. Procedure

The lower thermocouple probe is positioned $1\frac{1}{2}$ inches below the heated cylinder. The experimental apparatus is filled with one of the test materials and the gate valve is adjusted to give a Peclet number of 200. For the coarse grain sand this corresponds to a particle velocity of approximately 0.10 inches per second. The heater power is then adjusted to provide a temperature difference of approximately 20 degrees between the free stream and wake centerline. The temperature at a particular point in the wake is recorded at one minute intervals to determine when steady-state conditions have been reached. The temperature at several points in the wake, the power supplied, and the mass flow rate are then recorded. During this process, usually taking 15 minutes, the supply hopper is refilled as required. Since the flow apparatus was designed to operate in the head independent range, refilling has no effect on the channel mass flow rate.

The gate valve is adjusted to give a moderate and then high Peclet number of 400 and 600, respectively, with the heater power in each case being increased to maintain a midstream temperature difference of approximately 20 degrees. Measurements are then made in the manner indicated before.

In the actual experiments, the entire procedure outlined above was repeated for each of the test materials a minimum of four times. In addition, wake temperature measurements were made for several

arbitrary combinations of material, probe location, and Peclet number, as a check on measurement repeatability.

A total of three granular materials were used. These include spherical glass beads, coarse grain sand, and mustard seed with mean particle diameters of 23.3, 26.8 and 81.4 mils, respectively. Mustard seed (hard, ellipsoidal-shaped particles) was chosen to represent a material with low thermal diffusivity.

For the experiments performed, certain physical and thermal properties of these materials were required. The physical properties include bulk and particle specific gravity, void ratio, and particle size. The thermal properties include thermal diffusivity and conductivity. The physical and thermal properties are summarized in Table B-1.

D. Results, Discussion of Results, Conclusions

The temperature profile in the wake as determined by the continuum solution is given in Eq. 4.2.14. At any particular downstream location x and spanwise location y the temperature depends on the material Peclet number and the ratio of the power supplied to the bulk thermal conductivity.

For each of the materials investigated, temperature measurements were made at three downstream locations for Peclet numbers of 200, 400 and 600. For a given Peclet number and material, the power supplied was kept constant at all downstream locations. For the coarse grain sand, the power supplied per unit cylinder length for

the low, moderate, and high Peclet numbers was 100, 140 and 180 watts/ft., respectively.

Experimental results are given in terms of dimensionless wake temperature excess versus spanwise location in inches with Peclet number and downstream location as parameters. Wake temperature measurements for the .750 inch diameter cylinder for the three granular materials with a Peclet number of 200 and a downstream location of $1\frac{1}{2}$ inches are given in Fig. 4.3.2. A symmetric curve representing the average measure of the wake temperature excess at each of the thermocouple locations for each of the three materials along with the continuum prediction is also shown. The results for Peclet numbers of 400 and 600 at a downstream location of $1\frac{1}{2}$ inches are given in Figs. 4.3.3 and 4.3.4, respectively.

Experimental results for Peclet numbers of 200, 400 and 600 at a downstream location of 3 inches are given in Figs. 4.3.5, 4.3.6 and 4.3.7, respectively. Results for the three Peclet numbers at a downstream location of $4\frac{1}{2}$ inches are given in Figs. 4.3.8, 4.3.9 and 4.3.10.

The temperature profiles in Figs. 4.3.2 to 4.3.10 show a definite wake-like behavior. The profiles are "bell-shaped," for given flow conditions the width increases with distance from the heated cylinder, and at a given location below the cylinder the profile narrows as the velocity is increased. In this general sense the profiles are similar to those obtained analytically for the line source in an idealized granular medium of uniform velocity. Any more quantitative agreement was not to be expected because of the idealizations in the analytical model.

The analytical model was of help in defining the key parameters of the problem, that is, the dimensionless temperature $\left(\frac{2\pi k\Delta T}{q}\right)$ and the Peclet number $\left(\frac{UL}{\alpha}\right)$, which have been used in preparing the foregoing graphs. However, when examining the experimental data for the three granular materials it is seen that even when presented in the above manner, data fall on three different curves rather than on a single one.

Fairly consistently the peak temperatures of the flowing mustard seed are the lowest of the three and those of the glass beads are the highest. Similarly, the wake seems to spread the fastest in the mustard seed.

When interpreting the data it has to be realized, of course, that the experiments were exploratory in nature and that the measurements may well be in error by ± 20%. The results are sufficiently consistent, however, to indicate that there may be additional parameters required for the full description of the wake formation. For example, it is to be realized that the idealized concept, which leads to the dimensionless temperature and Peclet number, did not account for the velocity profile in the wake or any changes in the bulk thermal properties for a moving granular medium. Both of these factors may contribute to the lack of complete thermal and dynamic similarity in the wake. In particular, the concept of a conductivity for a moving granular medium may have to be examined in more detail. When the granules are in motion the air in the voids may be displaced relative to the granules and in this way the air may enhance the heat transport. In future investigations on the wake in a moving granular medium, these aspects will certainly have to be considered.

References

1. Weidler, J. B. and Pasley, P. R., "Analytical Description of Behavior of Granular Media", Journal of the Proceedings of the ASCE — Engineering Mechanics Division, EM2, April 1969, pp. 379-394.

2. Drucker, D. C., "Coulomb Friction, Plasticity and Limit Loads", Journal of Applied Mechanics, vol. 21, 1954, pp. 71-74.

3. Drucker, D. C., Henkel, D. J., and Gibson, R. E., "Soil Mechanics and Work Hardening Theories of Plasticity", Transactions, ASCE, vol. 122, 1957, pp. 338-346.

4. Jenike, A. W. and Shield, R. T., "On the Plastic Flow of Coulomb Solids Beyond Original Failure", Journal of Applied Mechanics, vol. 26, 1959, pp. 599-602.

5. Shield, R. T., "On Coulomb's Law of Failure in Soils", Journal of the Mechanics and Physics of Solids, vol. 4, 1955, pp. 10-16.

6. Shaxley, J. H. and Evans, J. C., "The Variation of Pressure with Depth in Columns of Powders", Transaction of Faraday Society, vol. 55, pp. 60-72, 1923.

7. Deming, W. E. and Mehring, A. L., "The Gravitational Flow of Fertilizers and Other Comminuted Solids", Industrial and Engineering Chemistry, vol. 21, no. 7, July 1929, pp. 661-665.

8. Takahasi, K., "Experimental Investigation of the Velocity of Efflux of Granular Mass", Institute of Physical and Chemical Research, vol. 26, Jan. 1935, pp. 11-20.

9. Wolf, E. F. and Hohenleiten, H. L., "Experimental Study of the Flow of Coal in Chutes at Riverside Generating Station", Transactions, ASME, vol. 67, Oct. 1945, pp. 585-598.

10. Wolf, E. F. and Hohenleiten, H. L., "Flow of Coal in Chutes", Mechanical Engineering, vol. 70, April 1948, pp. 313-335.

11. Franklin, F. C. and Johanson, L. N., "Flow of Granular Material through a Circular Orifice", Chemical Engineering Science, vol. 4, 1955, pp. 119-129.

12. Newton, R. H., Dunham, G. S., and Simpson, T. P., Transactions American Institute Chemical Engineers, vol. 41, 1945, pp. 215-220.

13. Fowler, R. T. and Glastonbury, J. R., "The Flow of Granular Solids through Orifices", Chemical Engineering Science,

vol. 10, 1959, pp. 150-156.

14. Brown, R. L. and Richards, J. C., "Exploratory Study of the Flow of Granules through Apertures", Trans. Instn. Chem. Engrs., vol. 37, 1959, pp. 108-119.

15. Brown, R. L. and Richards, J. C., "Profile of Flow of Granules through Apertures", Trans. Instn. Chem. Engrs., vol. 38, 1960, pp. 243-256.

16. Beverloo, W. A., Leniger, H. A. and van de Velde, Jr., "The Flow of Granular Solids through Orifices", Chemical Engineering Science, vol. 15, 1961, pp. 260-269.

17. McDougall, I. R. and Knowles, G. H., "Flow of Particles through Orifices", Trans. Instn. Chem. Engrs., vol. 47, 1969, pp. T73-T78.

18. Trees, J., "A Practical Investigation of the Flow of Particulate Solids through Sloping Pipes", Trans. Instn. Chem. Engrs., vol. 40, 1962, pp. 286-296.

19. Roberts, A. W., "The Dynamics of Granular Material Flow through Curved Chutes", Mechanical and Chemical Engineering Transactions, Nov. 1967, pp. 216-224.

20. Jenike, A. W., Gravity Flow of Bulk Solids", University of Utah, Engineering Experimental Station, Bulletin No. 108, 1961.

21. Johanson, J. R. and Jenike, A. W., "Stresses and Velocity Fields in Gravity Flow of Bulk Solids", University of Utah, Engineering Experimental Station, Bulletin No. 116, May 1962, 138 p.

22. Jenike, A. W., "Storage and Flow of Solids", University of Utah, Engineering Experimental Station, Bulletin No. 123, Nov. 1964, 198 p.

23. Richmond, O., "Gravity Hopper Design", Mechanical Engineering, vol. 85, Jan. 1963, pp. 46-49.

24. Lee, Y., "Flow of Coal in Hoppers", Combustion, vol. 31, no. 7, Jan. 1960, pp. 20-27.

25. Roberts, A. W., "An Investigation of the Gravity Flow of Non-cohesive Granular Materials through Discharge Chutes", Journal of Engineering for Industry — Transactions, ASME, May 1969, pp. 373-381.

26. Gardner, G. C., "Limiting Conditions for Flow of a Cohesive Granular Material Down an Inclined Plane (Chute) or Between Paralle Inclined Walls (Bin or Channel)", Chemical Engineering

Science, vol. 17, 1962, pp. 1079-1086.

27. Gardner, G. C., "The 'Best' Hopper Profile for Cohesive Material", Chemical Engineering Science, vol. 18, 1963, pp. 35-39.

28. Delaplaine, J. W., "Forces Acting in Flowing Bed of Solids", AIChE Journal, vol. 2, no. 1, 1956, pp. 127-138.

29. Jenike, A. W., "Better Design for Bulk Handling", Chemical Engineering, Dec. 1954, pp. 175-180.

30. Jenike, A. W., Elsey, P. J. and Woolley, R. H., "Flow Properties of Bulk Solids", University of Utah, Engineering Experimental Station, Bulletin No. 96, Dec. 1958.

31. Holland, J., Miles, J. E. P., Schofield, C., and Shook, C. A., "Fluid Drag Effects in the Discharge of Granules from Hoppers", Trans. Instn. Chem. Engrs., vol. 47, 1969, pp. T154-T159.

32. Bosley, J., Schofield, C. and Shook, C. A., "An Experimental Study of Granular Discharge from Model Hoppers", Trans. Instn. Chem. Engrs., vol. 47, 1969, pp. T147-T152.

33. Rausch, J. M., Ph. D. Thesis, 1948, Princeton University.

34. Shook, C. A., Carleton, A. J. and Flain, R. J., "Effect of Fluid Drag on the Flow Rate of Granular Solids from Hoppers", Trans. Instn. Chem. Engrs., vol. 48, 1970, pp. T173-T175.

35. Toyama, S., "The Flow of Granular Materials in Moving Beds", Powder Technology, vol. 4, 1970-1971, pp. 214-220.

36. Kotchanova, I., "Experimental and Theoretical Investigations on the Discharge of Granular Materials from Bins", Powder Technology, vol. 4, 1970-1971, pp. 32-37.

37. Bagster, D. F. and Bridgewater, J., "The Flow of Granular Material over a Moving Blade", Powder Technology, vol. 3, 1969-1970, pp. 323-338.

38. Handley, M. F. and Perry, M. G., "Stresses in Granular Materials Flowing in Converging Hopper Sections", Powder Technology, vol. 1, 1967-1968, pp. 245-251.

39. Reisner, W., "The Behavior of Granular Materials in Flow out of Hoppers", Powder Technology, vol. 1, 1967-1968, pp. 257-264.

40. Platonov, P. and Poltorak, V., "Investigation of Shear of a

Granular Material Along a Bordering Surface", Powder Technology, vol. 3, 1969-1970, pp. 361-363.

41. Johanson, J. R., "Stress and Velocity Fields in the Gravity Flow of Bulk Solids", Journal of Applied Mechanics, Trans. ASME, Sept. 1964, pp. 499-506.

42. Jenike, A. W., "Steady Gravity Flow of Frictional-Cohesive Solids in Converging Channels", Journal of Applied Mechanics, Trans. ASME, March 1964, pp. 5-11.

43. Lee, J., Cowin, S. C. and Templeton, J. S., "An Experimental Study of the Kinematics of Flow through Hoppers", Trans. of the Society of Rheology, vol. 18, 1974, pp. 247-269.

44. Jenike, A. W., "Gravity Flow of Frictional-Cohesive Solids-Convergence to Radial Stress Fields", Journal of Applied Mechanics, Trans. ASME, March 1965, pp. 205-207.

45. Emery, R. B., "Aeration Apparatus Converts Bin from Funnel-Flow to Mass-Flow Characteristics", Journal of Engineering for Industry, Trans. ASME, Feb. 1973, pp. 37-41.

46. Gardner, G. C., "The Region of Flow When Discharging Granular Materials from Bin-Hopper Systems", Chemical Engineering Science, vol. 21, 1966, pp. 261-273.

47. Pariseau, W. G., "Gravity Flow of Ideally Plastic Materials through Slots", Journal of Engineering for Industry, Trans. ASME, May 1969, pp. 414-422.

48. Pariseau, W. G., "Discontinuous Velocity Fields in Gravity Flows of Granular Materials through Slots", Powder Technology, vol. 3, 1969-1970, pp. 218-226.

49. Marais, G. R., "Stresses in Wedges of Cohesionless Materials Formed by Free Discharge at the Apex", Journal of Engineering for Industry, Trans. ASME, May 1969, pp. 345-352.

50. Stainforth, P. T., Ashley, R. C. and Morley, J. N. B., "Computer Analysis of Powder Flow Characteristics", Powder Technology, vol. 4, 1970-1971, pp. 250-256.

51. Rao, L. V. and Venkatesevarly, D., "Static and Dynamic Wall Pressures in Experimental Mass Flow Bunkers", Powder Technology, vol. 10, 1974, pp. 143-152.

52. Blair-Fish, P. M. and Bransley, P. L., "Flow Patterns and Wall Stresses in a Mass Flow Bunker", Journal of Engineering for Industry, Trans. ASME, Feb. 1973, pp. 17-26.

53. Bransley, P. L., Blair-Fish, P. M. and James, R. G., "An Investigation of the Flow of Granular Materials", Powder Technology, vol. 8, 1973, pp. 197-206.

54. Cowin, S. C. and Goodman, M. A., "Two Problems in the Gravity Flow of Granular Materials", J. Fluid Mechanics, vol. 45, 1971, pp. 321-339.

55. Cowin, S. C., "A Theory for the Flow of Granular Materials", Powder Technology, vol. 9, 1974, pp. 61-69.

56. Gudehus, G., "Granular Media as Rate-Independent Simple Materials — Constitutive Relations", Powder Technology, vol. 3, 1969-1970, pp. 344-351.

57. Bagster, D. F., "The Prediction of the Force Needed to Move Blades through a Bed of Cohesionless Granules", Powder Technology, vol. 3, 1969-1970, pp. 153-162.

58. Jenike, A. W. and Johanson, J. R., "Bin Loads", Proceedings ASCE, Structural Division, April 1968, pp. 1011-1041.

59. Jenike, A. W. and Johanson, J. R., "On the Theory of Bin Loads", Journal of Engineering for Industry, Trans. ASME, May 1969, pp. 339-344.

60. Jenike, A. W., Johanson, J. R., and Carson, J. W., "Bin Loads — Part 2: Concepts", Journal of Engineering for Industry, Trans. ASME, Feb. 1973, pp. 1-5.

61. Jenike, A. W., Johanson, J. R., and Carson, J. W., "Bin Loads — Part 3: Mass-Flow Bins", Journal of Engineering for Industry, Trans. ASME, Feb. 1973, pp. 6-12.

62. Jenike, A. W., Johanson, J. R., and Carson, J. W., "Bin Loads — Part 4: Funnel-Flow Bins", Journal of Engineering for Industry, Trans. ASME, Feb. 1973, pp. 13-16.

63. Jenike, A. W., "Gravity Flow of Solids", Trans. Instn. Chem. Engrs., vol. 40, 1962, pp. 264-271.

64. Deutsch, G. P. and Clyde, D. H., "Flow and Pressure of Granular Materials in Silos", Proceedings ASCE — Engineering Mechanics Division, Dec. 1967, pp. 103-125.

65. Johanson, J. R., "Modeling Flow of Bulk Solids", Powder Technology, vol. 5, 1971-1972, pp. 93-99.

66. Williams, J. C., Birks, A. H., and Bhattacharya, D., "The Direct Measurement of the Failure Function of a Cohesive Powder", Powder Technology, vol. 4, 1970-1971, pp. 328-337.

67. Wenzel, F., "Pressure Behavior in Double Cylindrical Silos", Journal of Engineering for Industry, Trans. ASME, Feb. 1973, pp. 97-100.

68. Wright, H., "An Evaluation of the Jenike Bunker Design Method", Journal of Engineering for Industry, Trans. ASME, Feb. 1973, pp. 48-54.

69. Schweder, J., "Measurement of Powder Properties for Hopper Design", Journal of Engineering for Industry, Trans. ASME, Feb. 1973, pp. 55-59.

70. Bagster, D.F., "A Geometric Study of In-Bin Blending", Journal of Engineering for Industry, Trans. ASME, Feb. 1973, pp. 86-92.

71. Wieghardt, K., "Experiments in Granular Flow", Annual Review of Fluid Mechanics, vol. 7, 1975, pp. 89-114.

72. Spencer, A.J.M., "A Theory of the Kinematics of Ideal Soil Under Plane Strain Conditions", J. Mech. Phys. Solids, vol. 12, 1963, pp. 337-351.

73. Shield,R.T., "Mixed Boundary Value Problems in Soil Mechanics", Quarterly of Applied Mathematics, vol. 11, 1953, pp. 61-75.

74. De Josselin De Jong, G., "The Double Sliding, Free Rotating Model for Granular Assemblies", Gestechnique, vol. 21, 1971, pp. 155-163.

75. Mandl, G. and Fernandez Luque, R., "Fully Developed Plastic Shear Flow of Granular Materials", Gestechnique, vol. 21, 1970, pp. 277-307.

76. Drescher, A. and De Josselin De Jong, G., "Photoelastic Verification of a Mechanical Model for the Flow of a Granular Material", J. Mech. Phys. Solids, vol. 20, 1972, pp. 337-351.

77. Shield, R.T., "Stress and Velocity Fields in Soil Mechanics", J. of Math. and Phys., vol. 33, 1955, pp. 144-156.

78. Drucker, D.C., Prager, W., and Greenberg, H.J., "Extended Limit Design Theorems for Continuous Media", Quarterly of Applied Mathematics, vol. 9, 1952, pp. 381-389.

79. Drucker, D.C., "Some Implications of Work Hardening and Ideal Plasticity", Quarterly of Applied Mathematics, vol. 7, 1950, pp. 411-418.

80. Johanson, J. R. and Jenike, A. W., "Review of the Principles of Flow of Bulk Solids", CIM Transaction, vol. 78, 1970, pp. 141-146.

81. Johanson, J. R. and Jenike, A. W., "Solids Flow in Bins and Moving Beds", Chemical Engineering Progress, vol. 66, 1970, pp. 31-34.

82. Brown, R. L., "Minimum Energy Theorem for Flow of Dry Granules through Apertures", Nature, vol. 191, 1961, pp. 458-461.

83. Duffy, J. and Mindlin, R. D., "Stress-Strain Relations and Vibrations of a Granular Medium", J. of Applied Mechanics, vol. 79, 1957, pp. 585-593,

84. Deresiewicz, H., "Stress-Strain Relations for a Simple Model of a Granular Medium", Journal of Applied Mechanics, vol. 80, 1958, pp. 402-406.

85. Scarlett, B. and Todd, A. C., "The Critical Porosity of Free Flowing Solids", Trans. ASME, J. Engineering for Industry, vol. 91, 1969, pp. 478-487.

86. Taylor, D. W., Fundamentals of Soil Mechanics, John Wiley and Sons, Inc., 1948.

87. Sokolovski, V. V., Statics of Soil Media, Butterworth Scientific Publications, 1960.

88. Scott, R. F., Principles of Soil Mechanics, Addison-Wesley Publishing Company, Inc., 1963.

89. Courant, R. and Hilbert, D., Methods of Mathematical Physics, vol. 2, Interscience Publishers, 1962.

90. Garabedian, P. R., Partial Differential Equations, John Wiley and Sons, Inc., 1974.

91. Courant, R. and Friedrichs, K. O., Supersonic Flow and Shock Waves, Interscience Publishers, 1956.

92. Hill, R., The Mathematical Theory of Plasticity, Oxford University Press, 1967.

93. Schlichting, H., Boundary-Layer Theory, McGraw-Hill Book Company, 1968.

94. Cole, J. D., Perturbation Methods in Applied Mathematics, Blaisdell Publishing Company, 1968.

95. Sullivan, W. N., "Heat Transfer to Flowing Granular Media", Ph. D. Thesis, California Institute of Technology, 1972.

96. Rainville, E. D. and Bedient, P. E., Elementary Differential Equations, The MacMillan Company, 1969.

97. Drucker, D. C. and Prager, W., "Soil Mechanics and Plastic Analysis or Limit Design", Quarterly of Applied Mathematics, vol. 10, 1952.

98. Drucker, D. C., "Limit Analysis of Two and Three Dimensional Soil Mechanics Problems", Journal of the Mechanics and Physics of Solids, vol. 1, 1953.

99. Shield, R. T., "Plastic Flow in a Converging Conical Channel", Journal of the Mechanics and Physics of Solids, vol. 3, 1955.

100. Kuchanov, S. I., Pis'Men, L. M. and Levich, V. G., "Mass and Heat Transfer in a Granular Bed", Heat Transfer — Soviet Research, vol. 1, no. 1, Jan. 1969, pp. 17-23.

101. Barker, J. J., "Heat Transfer in Packed Beds", Industrial and Engineering Chemistry, vol. 57, no. 4, April 1965, pp. 43-51.

102. Dul'nev, G. N., Zarichnyak, Y. P., Muratove, B. L. and Sigalova, Z. N., "Dependence of the Contact Heat Conductivity of Granular Systems on the External Load", IFZ (Journal of Engineering Physics), vol. 11, no. 2, 1966, pp. 202-206.

103. Sullivan, W. N. and Sabersky, R. H., "Heat Transfer to Flowing Granular Media", Int. J. Heat and Mass Transfer, vol. 18, 1975, pp. 97-107.

104. Uhl, V. W. and Root, W. L., "Heat Transfer to Granular Solids in Agitated Units", Chem. Engng. Progr., vol. 63, 1967, pp. 81-92.

105. Brinn, M. S., Friedman, S. J., Gluckert, F. A. and Pigford, R. L., "Heat Transwer to Granular Materials", Industrial and Engineering Chemistry, vol. 90, 1948, pp. 1050-1061.

106. Donskov, S. V., "Heat Loss from a Round Cylinder in Transverse Flow of a Granular Medium", Teploenergetica, vol. 5, no. 10, 1958, pp. 65-73.

107. Kurochkin, Y. P., "Heat Transfer Between Tubes of Different Sections and a Stream of Granular Material", IFZ (J. of Engineering Physics), vol. 10, no. 6, 1966, pp. 447-449.

108. Harakas, N. K. and Beatty, K. O., "Moving Bed Heat Transfer: Effect of Interstitial Gas with Fine Particles", Chemical

Engineering Progress Symposium Series, vol. 59, no. 41, 1963, pp. 122-128.

109. Tamarin, A. E., Dunskii, V. D. and Gorbacher, L. V., "A Study of the Transfer of Heat Between a Surface and a Layer of Moving Particles", IFZ (Journal of Engineering Physics), vol. 13, no. 4, 1967, pp. 450-454.

110. Wechsler, A. E., "Thermal and Mechanical Properties of Evacuated Powders", Powder Technology, vol. 3, 1969-1970, pp. 163-169.

111. Yagi, S. and Kunii, D., "Studies on Effective Thermal Conductivities in Packed Beds", AIChE Journal, vol. 3, no. 3, pp. 373-381.

112. Harriot, P., "Heat Transfer in Scraped-Surface Exchangers", Chemical Engineering Progress Symposium Series, vol. 55, no. 29, pp. 137-138.

113. Dul'nev, G. N. and Sigalova, Z. N., "Effective Conductivity of Granular Materials", IFZ (Journal of Engineering Physics), vol. 13, no. 5, 1967, pp. 670-685.

114. Yagi, S. and Kunii, D., "Studies on Heat Transfer Near Wall Surface in Packed Beds", AIChE Journal, vol. 6, no. 1, 1960, pp. 97-104.

115. Berry, M. R., Parker, R. W. and Dickerson, R. W., "A Dry Materials Heat Exchanger with Regeneration", ASME publication 73-WA/HT-14, Nov. 1973.

116. Mickley, H. S. and Fairbanks, D. F., "Mechanism of Heat Transfer to Fluidized Beds", AIChE Journal, vol. 1, 1955, pp. 373-384.

117. Baskakov, A. P., "The Mechanism of Heat Transfer Between a Fluidized Bed and a Surface", Int. Chem. Eng., vol. 4, no. 2, 1964, pp. 320-324.

118. Botterill, J. S. M. and Williams, J. R., "The Mechanism of Heat Transfer to Gas Fluidized Beds", Trans. Instr. Chem. Engrs., vol. 41, no. 5, 1963, pp. 217-230.

119. Ziegler, E. N. and Agrawal, S., "On the Optimum Heat Transfer Coefficient at an Exchange Surface in a Gas Fluidized Bed", Chem. Engng. Science, vol. 24, 1969, pp. 1235-1240.

120. Gabor, J. D., "Wall-to-Bed Heat Transfer in Fluidized and Packed Beds", Chemical Engineering Progress Symposium Series, vol. 66, no. 105, 1970, pp. 76-86.

121. Baskakov, A. P., "Transfer of Heat from an Isothermal Surface to a Continuous Flow of Dispersed Medium", Heat Transfer-Soviet Research, vol. 1, no. 6, 1969, pp. 103-107.

122. Kubie, J. and Broughton, J., "A Model of Heat Transfer in Gas Fluidized Beds", Int. J. Heat and Mass Transfer, vol. 18, 1975, pp. 289-299.

123. Hougen, J. O. and Piret, E. L., "Effective Thermal Conductivity of Granular Solids through which Gases are Flowing", Chemical Engineering Progress, vol. 47, no. 6, 1951, pp. 295-303.

124. Hougen, J. O. and Molino, D. F., "Thermal Conductivity of Granular Solids through which Gases are Flowing", Chemical Engineering Progress, vol. 48, no. 3, 1952, pp. 147-149.

125. Kasatkin, A. G., Lekae, V. M., and Elkin, L. N., "Investigation of the Operation of Screw Conveyer Heat Exchanger Reactors", Internal Chemical Engineering, vol. 4, no. 1, 1964, pp. 85-88.

126. Harakas, N. K., "Moving Bed Heat Transfer", Ph. D. Thesis North Carolina State University, 1962.

127. Donskov, S. B., "Heat Loss from Clusters of Tubes in a Transverse Flow of a Sifting Body (Sand)", Teploenergetica, vol. 5, no. 11, pp. 76-81.

128. Kreith, F., Principles of Heat Transfer, 2nd ed., International Textbook Company, 1967.

129. Jumikis, A. R., Thermal Soil Mechanics, Rutgers University Press, 1966.

130. Eckert, E. R. G. and Drake, R. M., Analysis of Heat and Mass Transfer, McGraw-Hill Book Company, 1972.

131. Poole, W. D., Chesness, J. L., Val, S. Ramarao, V., and Wratten, F. T., "Physical and Thermal Properties of Rough Rice", Trans. ASAE, vol. 12, 1969, pp. 801-803.

132. Broughton, J. and Kubie, J., "A Note on Heat Transfer Mechanism as Applied to Moving Granular Media", to be published, 1975.

APPENDIX A — PERTURBATION TO "EXACT" SOLUTION DEVELOPED BY SULLIVAN [95]

An alternate approximate solution to the system of equations developed in Chapter II, Section 1 will be presented here. This solution is a perturbation to the "exact" solution of Sullivan [95] described in Chapter II, Section 2. Again it will be assumed that the material obeys the Jenike-Shield yield condition, the material is cohesionless, and that the material flows at constant bulk density. The problem considered is for the steady flow of a frictional cohesionless solid through plane symmetric channels with "small" wall friction.

The geometry of the channel is given in Fig. A-1. The material is assumed to satisfy a Coulomb condition along the walls, namely,

$$\left. \frac{\tau_{r\theta}}{\sigma_\theta} \right|_{\theta=\theta_w} = -\tan(\delta)$$

where δ is restricted to being "small". The entrance and exit planes at $r = R$ and $r = r_o$ are assumed to be free surfaces with $\tau_{r\theta} = \sigma_\theta = \sigma_r = 0$. It is also assumed that the channel walls are sufficiently steep that the body force acts in a purely radial direction.

Again the component stresses σ_r, σ_θ and $\tau_{r\theta}$ are written in terms of a mean stress σ and a stress angle ψ such that the yield condition, Eq. 2.1.20, is satisfied identically. The relations are given in Eq. 2.2.6. The solution developed by Sullivan for the steady flow of a frictional cohesionless material through plane channels with smooth walls and radial gravity described earlier may be written

$$\sigma = S(r)$$

$$\psi = \frac{\pi}{2}$$

$$u = \bar{u}\frac{r_o}{r} = U$$

$$v = 0$$

where $S(r)$ is given by Eq. 2.2.15 and $\bar{u}$ is given in Eq. 2.2.16.

Following Courant and Hilbert [89], it will be assumed that from the stress and velocity state defined by the Sullivan solution the actual flow deviates only by small "quantities" such that second order terms in these "quantities" and their derivatives may be neglected. A solution of the following form is assumed

$$\sigma = S(r) + \tilde{\sigma}$$

$$\psi = \frac{\pi}{2} + \tilde{\psi}$$

$$u = U + \tilde{u} \qquad\qquad (A. 1)$$

$$v = 0 + \tilde{v}$$

where $\tilde{\sigma}, \tilde{\psi}, \tilde{u}, \tilde{v}$ are the small "quantities" that represent the perturbation from the radial body force solution.

Substitution of the relations given by Eq. A.1 into the equations of continuity, isotropy and motion and then the subsequent neglecting of second order terms in the perturbation variables yields the following linear system in the perturbation variables

continuity $\qquad \dfrac{\partial \tilde{u}}{\partial r} + \dfrac{\tilde{u}}{r} + \dfrac{1}{r}\dfrac{\partial \tilde{v}}{\partial \theta} = 0$

isotropy $\qquad \dfrac{\partial \tilde{v}}{\partial r} - \dfrac{\tilde{v}}{r} + \dfrac{1}{r}\dfrac{\partial \tilde{u}}{\partial \theta} = 0$

θ equation
of motion $\qquad -2\dfrac{dS}{dr}(\sin\varphi)\tilde{\psi} - 2S\sin\varphi\dfrac{\partial \tilde{\psi}}{\partial r} + \dfrac{1}{r}\dfrac{\partial \tilde{\sigma}}{\partial \theta}(1+\sin\varphi)$ $\qquad$ (A. 2)

$$-4\dfrac{S}{r}(\sin\varphi)\tilde{\psi} = -\rho\, U\left(\dfrac{\partial \tilde{v}}{\partial r} + \dfrac{U\tilde{v}}{r}\right)$$

r equation
of motion $\qquad \dfrac{\partial \tilde{\sigma}}{\partial r}(1-\sin\varphi) - \dfrac{2S}{r}\sin\varphi\dfrac{\partial \tilde{\psi}}{\partial \theta} - \dfrac{2S}{r}\sin\varphi = -\rho\dfrac{\partial}{\partial r}(U\tilde{u})$.

The above system of equations, Eq. A. 2, may be written in matrix form
as follows:

$$
\begin{bmatrix}
(1-\sin\varphi) & 0 & \rho U & 0 \\
0 & -2S\sin\varphi & 0 & \rho U \\
0 & 0 & 0 & 1 \\
0 & 0 & 1 & 0
\end{bmatrix}
\begin{Bmatrix}
\dfrac{\partial \tilde{\sigma}}{\partial r} \\[4pt]
\dfrac{\partial \tilde{\psi}}{\partial r} \\[4pt]
\dfrac{\partial \tilde{u}}{\partial r} \\[4pt]
\dfrac{\partial \tilde{v}}{\partial r}
\end{Bmatrix}
+
\begin{bmatrix}
0 & \dfrac{-2S\sin\varphi}{r} & 0 & 0 \\[4pt]
\dfrac{1+\sin\varphi}{r} & 0 & 0 & 0 \\[4pt]
0 & 0 & \dfrac{1}{r} & 0 \\[4pt]
0 & 0 & 0 & \dfrac{1}{r}
\end{bmatrix}
\begin{Bmatrix}
\dfrac{\partial \tilde{\sigma}}{\partial \theta} \\[4pt]
\dfrac{\partial \tilde{\psi}}{\partial \theta} \\[4pt]
\dfrac{\partial \tilde{u}}{\partial \theta} \\[4pt]
\dfrac{\partial \tilde{v}}{\partial \theta}
\end{Bmatrix}
+
$$

$$
\begin{bmatrix}
-\dfrac{2}{r}\sin\varphi & 0 & \rho\dfrac{dU}{dr} & 0 \\[4pt]
0 & -2\sin\varphi\left(\dfrac{dS}{dr}+\dfrac{2S}{r}\right) & 0 & \dfrac{\rho U}{r} \\[4pt]
0 & -4\dfrac{dU}{dr} & 0 & -\dfrac{1}{r} \\[4pt]
0 & 0 & \dfrac{1}{r} & 0
\end{bmatrix}
\begin{Bmatrix}
\tilde{\sigma} \\[4pt]
\tilde{\psi} \\[4pt]
\tilde{u} \\[4pt]
\tilde{v}
\end{Bmatrix}
= \underline{0} \quad . \qquad \text{(A. 3)}
$$

If the following definitions are made

$$\underline{x} = \text{vector} \equiv \begin{Bmatrix} \tilde{\sigma} \\ \tilde{\psi} \\ \tilde{u} \\ \tilde{v} \end{Bmatrix} \qquad\qquad \text{(A. 4)}$$

$$B = \text{matrix} \equiv \begin{bmatrix} 0 & -2S\sin\varphi & 0 & 0 \\ 1+\sin\varphi & 0 & 0 & 0 \\ 0 & 0 & 1 & 0 \\ 0 & 0 & 0 & 1 \end{bmatrix} \tag{A.5}$$

$$A = \text{matrix} \equiv \begin{bmatrix} 1-\sin\varphi & 0 & \rho U & 0 \\ 0 & -2S\sin\varphi & 0 & \rho U \\ 0 & 0 & 0 & 1 \\ 0 & 0 & 1 & 0 \end{bmatrix} \tag{A.6}$$

$$C = \text{matrix} \equiv \begin{bmatrix} -\dfrac{2\sin\varphi}{r} & 0 & \rho\dfrac{dU}{dr} & 0 \\ 0 & 2\sin\varphi\left(\dfrac{dS}{dr}+\dfrac{2S}{r}\right) & 0 & \rho\dfrac{U}{r} \\ 0 & -4\dfrac{dU}{dr} & 0 & -\dfrac{1}{r} \\ 0 & 0 & \dfrac{1}{r} & 0 \end{bmatrix} \tag{A.7}$$

then the matrix Eq. A.3 may be written

$$A\underline{x}_r + \frac{1}{r}B\underline{x}_\theta + C\underline{x} = \underline{0} \tag{A.8}$$

where here the subscripts of r and θ refer to partial differentiation, with respect to r and θ respectively, and the zero on the right hand side of the matrix equation is a vector. Premultiplying by the inverse of matrix B, B^{-1}, gives

$$\frac{1}{r}\underline{x}_\theta + B^{-1}A\underline{x}_r + B^{-1}C\underline{x} = \underline{0} \ . \tag{A.9}$$

It is initially assumed that the above system is hyperbolic. Following the method outlined by Courant and Hilbert [89] for reducing

a hyperbolic system to normal form, characteristic curves C:
$\Omega(r, \theta) = 0$ are given by the differential equation

$$\frac{dr}{rd\theta} = + \lambda \qquad \text{(A. 10)}$$

or

$$\frac{1}{r}\Omega_\theta + \lambda\Omega_r = 0 \qquad \text{(A. 10a)}$$

where λ is defined as the root of the algebraic equation

$$\|B^{-1}A - \lambda I\| = 0 \quad . \qquad \text{(A. 11)}$$

The scalar characteristic equation for λ given by Eq. A. 11 is just

$$(\lambda^2 - 1)\left(\lambda^2 - \frac{1-\sin\varphi}{1+\sin\varphi}\right) = 0$$

which gives

$$\lambda_{1,2} = \pm 1 \qquad \text{(A. 12)}$$

and

$$\lambda_{3,4} = \pm \sqrt{\frac{1-\sin\varphi}{1+\sin\varphi}} \quad . \qquad \text{(A. 13)}$$

Hence, there exists four positive distinct eigenvalues and the system
is hyperbolic.

In general, for the system of four partial differential equations
defining both the velocity and stress fields, the characteristic direc-
tions (which for the present analysis are given by the λ's defined
above) associated with the velocity field are

$$\lambda^G_{1,2} = \tan\left(\frac{2\psi \pm 90}{2}\right) \qquad \text{(A. 14)}$$

and those associated with the stress field are

$$\lambda^G_{3,4} = \tan\left(\frac{2\psi \pm (90-\varphi)}{2}\right) . \qquad \text{(A. 15)}$$

The above result can be obtained by following for the general set of differential equations the general method outlined earlier. By referring to the Mohr diagram and Mohr Envelope, Fig. A-2, it is seen that the characteristic directions associated with the stress field are coincident with the lines of slip defined by the point of tangency of the Mohr Envelope to the Mohr Circle, and that the characteristic direction associated with the velocity field are coincident with the lines of maximum shear stress. These are obvious consequences of the Jenike constitutive postulates.

It is seen that the characteristic directions for both velocity and stress field in the present analysis are given by

$$\lambda_{1,2} = \lim_{\psi \to 0} \lambda_{1,2}^G$$

and

$$\lambda_{3,4} = \lim_{\psi \to 0} \lambda_{3,4}^G$$

respectively. That is, the characteristic directions for the linearized system of equations that describe a flow that deviates only "slightly" from a main flow given by the Sullivan solution are identical with the characteristic directions for the main flow.

Since the equations are linear, the characteristic directions are independent of the dependent variables, and thus the characteristic equations may be solved independently of the solution. The characteristics for the velocity field are given by the solution to the ordinary differential equations

$$\frac{dr}{rd\theta} = \lambda_1 \quad \text{and} \quad \frac{dr}{rd\theta} = \lambda_2$$

yielding

$$r = + c_1 e^{+\theta} \quad \text{and} \quad r = + c_2 e^{-\theta} \quad \text{for} \qquad \text{(A. 16)}$$

the first and second velocity characteristics, respectively. The

characteristics for the stress field are given by the solutions to the

differential equations

$$\frac{dr}{rd\theta} = \lambda_3 \quad \text{and} \quad \frac{dr}{rd\theta} = \lambda_4$$

yielding

$$r = + c_3 e^{-\sqrt{\frac{1+\sin\varphi}{1-\sin\varphi}}\,\theta} \quad \text{and} \quad r = + c_4 e^{-\sqrt{\frac{1+\sin\varphi}{1-\sin\varphi}}\,\theta} \qquad \text{(A. 17)}$$

for the first and second stress characteristics, respectively. It is

seen that the characteristics for the system are logarithmic spirals.[*]

For the above set of eigenvalues, that is, the characteristic

directions given by the λ's, the eigenvector matrix for the hyperbolic

system defined by the matrix Eq. A.9 is found to be

$$X = \begin{bmatrix} 1 & 1 & 1 & 1 \\ \dfrac{-1}{2S\sin\varphi} & \dfrac{+1}{2S\sin\varphi} & \dfrac{-\lambda_3(1+\sin\varphi)}{2S\sin\varphi} & \dfrac{+\lambda_3(1+\sin\varphi)}{2S\sin\varphi} \\ \dfrac{+\sin\varphi}{\rho U} & \dfrac{+\sin\varphi}{\rho U} & 0 & 0 \\ \dfrac{+\sin\varphi}{\rho U} & \dfrac{-\sin\varphi}{\rho U} & 0 & 0 \end{bmatrix} \qquad \text{(A. 18)}$$

[*]For the case when the inertial terms are negligible, Sokolovski [87] found the stress characteristics as logarithmic spirals when $\psi = \psi_0 = $ constant.

and the inverse of the eigenvector matrix, X^{-1}, is given by

$$
X^{-1} = \frac{1}{|X|}
\begin{bmatrix}
0 & 0 & \dfrac{-\lambda_3(1+\sin\varphi)}{\rho US} & \dfrac{-\lambda_3(1+\sin\varphi)}{\rho US} \\[2ex]
0 & 0 & \dfrac{-\lambda_3(1+\sin\varphi)}{\rho US} & \dfrac{+\lambda_3(1+\sin\varphi)}{\rho US} \\[2ex]
\dfrac{-\lambda_3\sin\varphi(1+\sin\varphi)}{\rho^2 U^2 S} & \dfrac{+2\sin^2\varphi}{\rho^2 U^2} & \dfrac{+\lambda_3(1+\sin\varphi)}{\rho US} & \dfrac{1}{\rho US} \\[2ex]
\dfrac{-\lambda_3\sin\varphi(1+\sin\varphi)}{\rho^2 U^2 S} & \dfrac{-2\sin^2\varphi}{\rho^2 U^2} & \dfrac{+\lambda_3(1+\sin\varphi)}{\rho US} & \dfrac{-1}{\rho US}
\end{bmatrix}
$$

<div align="right">(A. 19)</div>

where $|X|$ is the determinant of the matrix X given by

$$
|X| = \frac{-2\lambda_3\sin\varphi(1+\sin\varphi)}{\rho^2 U^2 S} \quad .
\tag{A. 20}
$$

Define a new vector variable, $\underline{y}$, by

$$
\underline{x} = X\underline{y} \quad \text{then} \tag{A. 21}
$$

$$
\underline{x}_\theta = X\underline{y}_\theta \quad \text{since } X \text{ is independent of } \theta
$$

and

$$
\underline{x}_r = X_r\underline{y} + X\underline{y}_r \quad .
$$

Substituting for the $\underline{x}$ in Eq. A. 9 and premultiplying by X^{-1}

$$
\frac{1}{r}X^{-1}X\underline{y}_\theta + X^{-1}B^{-1}AX_r\underline{y} + X^{-1}B^{-1}AX\underline{y}_r + X^{-1}B^{-1}CX\underline{y} = \underline{0} \quad .
$$

However the eigenvector matrix X diagonalizes the matrix $B^{-1}A$ such that

$$X^{-1}B^{-1}AX = \Lambda = \begin{bmatrix} \lambda_1 & 0 & 0 & 0 \\ 0 & \lambda_2 & 0 & 0 \\ 0 & 0 & \lambda_3 & 0 \\ 0 & 0 & 0 & \lambda_4 \end{bmatrix} \tag{A.22}$$

and the matrix equation for $\underline{y}$ becomes

$$\frac{1}{r}\underline{y}_\theta + \Lambda \underline{y}_r + (X^{-1}B^{-1}AX_r + X^{-1}B^{-1}CX)\underline{y} = \underline{0} \quad . \tag{A.23}$$

It was assumed that the actual flow of a frictional, cohesionless solid through converging channels deviates only slightly from a main flow defined by Sullivan's "exact" solution for smooth walls and radial gravity. It has been shown that the linear system of equations describing this "slight" deviation is hyperbolic and the characteristics for both the velocity and stress field coincide with those for the frictionless flow. The characteristic equations were found and the characteristics are logarithmic spirals from the origin. This agrees with Sokolovski [87] for negligible inertial terms and constant stress angle. The system was then reduced to normal form which yields a system of four ordinary differential equations for the stress-velocity vector $\underline{y}$.

The assumed form of the solution, Eq. (A.3), implies that the perturbation quantities are uniformly small in that second order terms of all of these quantities may be neglected. However, by writing the complete system of equations in dimensionless form and assuming a form of solution not necessarily uniform in a perturbation parameter, the perturbation parameter may be found and it may be seen that the solution is indeed not uniform in this parameter. This more general approach is followed in Chapter II, Section 3.

APPENDIX B – MATERIAL PROPERTIES

The subject matter of the thesis concerns the flow of a frictional, cohesionless solid (dry granular materials which exhibit negligible cohesion for example) and the heat transfer from a heated surface to a flowing, frictional, cohesionless solid. For the experiments performed, certain physical, mechanical and thermal properties were required. The physical properties include bulk specific gravity, particle specific gravity, void ratio (which can be determined from the bulk and particle specific gravities under certain conditions), and particle size; the mechanical properties include internal friction angle and wall friction angle (the coefficient of friction between a granular material and a well-defined surface); the thermal properties include bulk thermal diffusivity and bulk thermal conductivity.

A total of nine granular materials were used. Five of these consisted of different sizes of spherical glass beads ranging in diameter from 10.7 mils to 127.2 mils. Fine, medium and coarse grain quartz sand were also used. Mustard seed (hard, ellipsoidal-shaped particles) was chosen to represent a material with a low thermal diffusivity.

Most of the properties outlined above are bulk properties in that they depend on the particular arrangement of the grains (particles) in the granular mass. For example, a large variation in void ratio may be obtained by measuring the void ratio of the same material in both a "loose" and "dense" state. For this reason it is somewhat

important to establish an initial state or condition for each test sample for the material property evaluation.

Briefly, it has been experienced that if a given frictional cohesionless solid in the "loose" state undergoes shear deformation, the void ratio, which is defined as the ratio of the volume of the voids to the volume of the solids, initially decreases but at large shear strains reaches and remains at a near constant value. Similarly, if the same frictional, cohesionless solid in the "dense" state undergoes shear deformation, the void ratio slightly decreases, increases, and then at large shear strains reaches and remains at a near constant value. It is possible to prepare a test sample of this same material with a particular initial void ratio such that under shear deformation the void ratio remains essentially unchanged. The void ratio for the solid in both the "loose" and "dense" state approaches this constant void ratio at large shear strains. This constant void ratio will be called the critical void ratio.

For the experiments considered in the thesis, it is assumed that the granular material behaves as a frictional, cohesionless solid continuously failing (implying sufficiently large shearing deformations that "state state" flow conditions, i.e., constant void ratio, have been reached) at constant void ratio. Thus, the material properties are desired and were determined at the critical void ratio. The specific methods used in determining the material properties are described below. The material properties are summarized in Table B-1.

Bulk Specific Gravity, Particle Specific Gravity, and Void Ratio

Specific gravity is defined as the ratio of the density of a substance to the density of some reference substance, the reference substance usually being taken as distilled water at some specified temperature. Distilled water at 4°C which has a density of exactly 1.0 gm/cc will be taken as the reference substance. Thus, the measured density of any substance will be numerically equal to its specific gravity.

Bulk specific gravity at the critical or flowing void ratio is desired. The bulk density of a dry granular material is easily determined by measuring, with a graduated cylinder, the volume occupied by a known mass of the test substance. The volume corresponding to the critical or flowing state is achieved by capping and then slowly inverting (two inversions necessary) the filled cylinder. Denser states may be achieved by gently tapping the sides of the cylinder.

Sullivan [7] discussed a method for determining particle specific gravity. However, failure to remove all interstitial air using his test procedure will result in large (non-negligible) error in the particle specific gravity measurement. A more refined test procedure is given by Taylor [4]. For this particular investigation not all particle specific gravities were measured. The specific gravities for the five glass beads and the three quartz sands were taken from the literature [1, 3, 4]. The particle specific gravity for the mustard seed was determined by using Taylor's method.

Void ratio is defined as the ratio of the volume of the voids to the volume of the solids. For a granular material with negligible water content (water content is defined as the ratio of the weight of water to the weight of solids in a unit volume of material), the void ratio may be determined from the particle specific gravity, ρ_P, and the granular bulk specific gravity, ρ_B, in the following formula

$$\epsilon = \frac{\rho_P}{\rho_B} - 1 \ .$$

Particle Size

An arbitrary granular mass will consist of a random assortment of three-dimensional, irregular shaped particles. If with each of these particles there can be associated some characteristic length, then this length can be taken as a measure of the particle size. Since for such a definition to be meaningful it must be possible to prescribe this characteristic length in a standardized manner (measurement method), the particle size will depend on the particular method or manner of measurement chosen.

Normally in soil mechanics, the particle size distribution for a given granular mass is determined by performing a "sieve analysis". Briefly, the analysis consists of passing the given sample through a set of sieves (care must be taken in choosing the appropriate set of sieves) and weighing the amount of material retained on each sieve. Thus, in the sieve analysis the particle size is related to the mesh opening. A somewhat different approach, which is used in this investigation, is described below.

The characteristic length used in this investigation is defined as the distance between two planes each plane being tangent to opposite sides of the particle. If an irregular granular particle is viewed using a light microscope, the above characteristic length becomes the distance, d, between two lines each line being tangent to the outline of the particle planform area. For the spherical glass beads, this distance is just the particle diameter. For the irregular shaped quartz sand particles and the ellipsoidal-shaped mustard seed particle, the distance, d, will depend on the particular particle orientation. However, if d is measured for a "sufficient" number of randomly oriented particles, then d should be representative of the particle size and independent of orientation.

The light microscope used was equipped with a special eyepiece inscribed with parallel lines at $\frac{1}{2}$ mil spacing. The measurement procedure adopted consists of slowly traversing a slide containing a large number of randomly oriented particles and measuring all particles coming into view. Approximately 100 particles for each of the nine materials were measured. Mean particle size, standard deviation, and particle size distribution were determined. The experimental set up is shown in Figure B1. A typical particle size distribution is given in Figure B2.

Internal Friction Angle

Static friction between two plane solid surfaces can be characterized by a coefficient of friction which is defined as the ratio of the available friction force, which acts along the interface, to the

normal force between the surfaces. The force is applied through one of the surfaces and reacted at the other. The resultant of the reacted normal force and the maximum available friction force will act at an angle, φ, (called the friction angle) to the surface normal. From geometry and the above definition it is observed that

$$\frac{\text{maximum available friction force}}{\text{normal force}} = \text{coefficient of friction} = \text{tangent}(\varphi).$$

In a similar fashion the resultant of the applied normal force and applied tangent force will act at angle say, θ, to the surface normal. The angle θ is usually called the obliquity of the applied force. For all values of θ less than φ the system is stable in that there is no danger of slip between the solid surfaces. For $\theta = \varphi$, however, slip is imminent. Thus, for this system failure or instability occurs when the obliquity of the applied force is maximum and equal to the friction angle.

The ideas developed above for solid friction can be used to describe slip, or more appropriately the resistance to slip, on a specified plane in a granular mass. The problem here is more complicated in that resistance to slip is not due to merely sliding friction between solid surfaces but to a combination of sliding and rolling friction be between grains as well as an interlocking of the irregular surfaces of the individual grains.

The shear stress, τ, on a particular plane, analogous to the applied tangent force above, may be related to the applied normal stress, σ, through an obliquity angle, θ, as follows

$$\tau = \sigma \tan \theta \ .$$

Failure or slip is imminent when θ reaches its maximum value which is given by the internal friction angle, φ. The internal friction angle, φ, must be taken to be a measure of the overall resistance to slip due to the three mechanisms mentioned. The shear strength, s, which is just the shear stress at failure, is given by

$$s = \sigma \tan\varphi \ .$$

Thus in normal stress-shear stress coordinates, the shear strength is represented by two straight lines through the origin with slopes $+\tan\varphi$ and $-\tan\varphi$ which define what is called the Mohr Envelope. For a particular stress state defined by a Mohr's circle, failure or slip is imminent when the Mohr circle is tangent to the Mohr Envelope.

A direct shear type of apparatus was chosen to measure the internal friction angle for the test materials. Basically a direct shear test consists of shearing the test material along a particular (well-defined) plane and measuring the applied normal load and reactive shear load on the failure plane. The ratio of the maximum shear load achieved to the applied normal load corresponds to the peak-point internal friction angle. A brief description of the sample preparation, the direct shear machine, and the test procedure follows.

The sample, loaded into a shear box, is constrained peripherally by an upper and lower metal ring separated by approximately $\frac{1}{2}$ grain diameter and is constrained from above and below by two porous stones. For each test, the sample weight and test volume are measured to determine the initial void ratio. Each sample is prepared such that the initial void ratio is "near" the critical void ratio.

The direct shear machine, shown in Fig. B3, consists of three major parts: (1) a spring loaded apparatus to apply a known normal load to the test sample, (2) a constant speed motor to displace the upper half of the test sample relative to the lower half, and (3) a metal proving ring to measure the reactive shear load on the lower half of the test samples. The test procedure consists of applying a given normal load to the test sample, applying (through the constant speed motor) a shear displacement to the upper half of the test sample, and measuring the instantaneous shear displacement of the upper half and the instantaneous reactive shear load on the lower half. A typical plot of the ratio of shear load to normal load versus shear displacement is given in Fig. B4. The peak point friction angle corresponds to the maximum value of this ratio; the ultimate friction angle corresponds to the value of this ratio at large shear displacement. Since, as may be seen in Fig. B4, the difference in the peak point and ultimate values for this particular void ratio is not large, and since it is fairly common practice in soil mechanics to use peak point values from laboratory tests for analyses of problems in nature [4], peak point values were used in this investigation. A typical plot of peak shear load versus applied normal load is given in Fig. B5. The slope of the peak shear load versus applied normal load curve is just tangent (φ). The complete set of results is given in Table B1.

Generally the internal friction angle for cohesionless material is not a very strong function of applied normal load but is very sensitive to the initial void ratio. For the five sizes of glass beads tested, the variation is initial void ratio (test void ratio which was near the

critical void ratio) was not large. There was, however, an increase in internal friction angle with increase in standard deviation in particle diameter. This is perhaps related to the greater amount of interlocking taking place in the material with a larger variation in particle diameter. Interlocking might also explain the higher internal friction angles observed for the irregular-shaped sand particles.

Surface Friction Angle

One problem investigated experimentally and discussed in the thesis deals with the flow of a frictional cohesionless solid over a cylindrical surface. For these experiments two sets of cylinders were used. The first set were lucite with a smooth (as formed) surface finish; the second set were aluminum with a diamond knurl finish. Photographs of the 1" lucite and 1" aluminum cylinders are given in Figs. B6 and B7, respectively.

It was desired to determine the effective friction coefficient (or friction angle) for each individual test material and surfaces representative of each of the cylindrical surfaces. A very simple apparatus was designed and built to measure the surface friction angle. Basically the apparatus consisted of an open box (8 X 12 X 4" deep) to contain the test material, two test pads with surfaces representative of the cylindrical surfaces (photographs of the pad surfaces are given adjacent to the cylindrical surface photographs in Figs. B6 and B7), a pully attached to the box, a weight pan, and two sets of weights. The actual test apparatus is shown in Fig. B8.

The test procedure consists of applying a normal load to the test pad and then increasing the shear load by applying successive

weights to the test pan until slip is imminent. This is actually an iterative process in that often the final shear load increment will surpass the load necessary for slip requiring the test to be repeated with a decrease in the final load increment. The shear load required for slip was determined for eight normal loads for each of the nine materials. A typical plot of required shear load versus applied normal load is given in Fig. B9. The slope of the required shear load — applied normal load curve is just tangent (δ), where δ is the surface friction angle.

Thermal Diffusivity

The unsteady-state method for measuring thermal diffusivity of a granular mass proposed by Brinn [6] and used by Sullivan [7] was adopted. The method requires a simple test apparatus and a relatively short data acqusition time.

The apparatus consists of a $1\frac{1}{2}$ inch diameter copper tube wound with electrical resistance heater tape connected to a variable AC power source. One thermocouple is embedded in the wall of the copper tube to provide wall temperature; one thermocouple is positioned along the tube centerline to provide centerline temperature; one thermocouple is positioned in an ice-water bath to act as a reference junction. A schematic of the test apparatus is shown in Fig. B10.

The test material is loaded into the copper tube and the ends are capped. The test procedure consists of raising the wall temperature to approximately $50°F$ above the initially uniform temperature of the granular mass, and then measuring the temperature difference

between the wall and centerline at one minute intervals while keeping the wall temperature essentially constant.

For a cylindrical body initially at uniform temperature T_0 with a wall at radius R raised instantaneous at $t = 0$ to temperature T_1 (wall temperature at T_1 constant for all $t > 0$), the centerline temperature is given by

$$\theta(t) = \frac{T_1 - T_c}{T_1 - T_0} = 2 \sum_{n=1}^{\infty} \left[\frac{J_0(0)}{a_n J_1(a_n)} \cdot \exp\left(-\alpha \frac{a_n^2 t}{R^2}\right) \right]$$

where J_0 and J_1 are Bessel functions and the a_n's are the zeros of J_0. For increasing $\alpha t/R^2$ successive terms in the infinite expansion are of decreasing importance. Thus for large $\alpha t/R^2$ the slope of $\log_{10}(T_1 - T_c)/(T_1 - T_0)$ should approach a straight line with slope $-2.5\alpha/R^2$. As discussed by Sullivan [7] the second term in the expansion is negligible with respect to the first for $(\alpha t/R^2) > .3$ which should be reached on the order of 10 minutes for a typical granular material in this test apparatus.

A typical plot of $\log_{10}(T_1 - T_c)/(T_1 - T_0)$ versus time is given in Fig. B11. A summary of the thermal diffusivity data for the nine granular materials is given in Table B1. The data for thermal diffusivity of quartz sand agrees well with the data given by Jumkis [8].

Thermal Conductivity

The thermal conductivity was not measured directly. Instead the specific heat of the particles was measured and then the thermal conductivity was found using the definition

$$k = \rho c \alpha$$

where ρ and α are the previously determined bulk density and thermal diffusivity, respectively.

The same apparatus as used in the diffusivity test was used here with the wall condition changed from constant temperature to constant heat flux. To effect this change the apparatus was wound with a second electrical resistance tape heater to act as a guard heater, the two heaters being separated by a $\frac{1}{16}$ inch section of cardboard. In addition to the wall and centerline thermocouples, one thermocouple was positioned on each side of the cardboard section. The inner and other heaters were connected to separate variable AC power sources.

The test material was loaded into the copper tube and the ends were capped. The entire apparatus was then wrapped with rock wool insulation to minimize heat losses from portions of the apparatus not covered with the guard heater. The test procedure consists of applying a known AC voltage to the inner heater, and then measuring the wall temperature and the difference in temperature between the wall and centerline at one minute intervals while keeping the temperature difference across the cardboard less than $\frac{1}{2}°$F.

Neglecting the heat capacity of the copper tube, the exact solution for the radial temperature distribution for a cylindrical section with a constant heat flux, q'', at $r = R$ is given by Carslaw and Jaeger [5] as

$$T(r,t) - T_0 = 2q''\frac{\alpha t}{kR} + q''\frac{R}{k}\left[\frac{r^2}{2R^2} - \frac{1}{4} - 2\sum_{n=1}^{\infty}\frac{J_0(rb_n/R)}{b_n^2 J_0(b_n)}\cdot\exp\left(\frac{\alpha t b_n^2}{R^2}\right)\right]$$

where $J_1(b_n) = 0$ [$b_1 = 3.832$, $b_2 = 7.016$, ...]. For large $\alpha t/R^2$ (($\alpha t/R) > .5$) the terms in the infinite expansion are negligible compared to the term linear in time. Thus a plot of $(T_1 - T_0)$ versus time

should approach a linear asymptote with slope $2q''/\rho cR$ which may be used to find c.

The heat capacity of the copper cylinder does have an effect on the terminal slope of the temperature-time plot. According to Sullivan [7] the terminal slope is given in terms of the total heat added to the cylinder by

$$\lim_{t\to\infty} \frac{dT_1}{dt} = \frac{Q}{M_1 c_1 + M_p c_p}$$

where M_1 and M_p are the mass of the cylinder and granular material respectively and c_1 the specific heat of the copper.

A typical temperature time plot is given in Figure B12. A plot of $T_1 - T_c$ is also given. The measured specific heats of the glass beads and quartz sand agreed quite well with published data [8, 9].

References (Appendices)

1. Scott, R. F., Principles of Soil Mechanics, Addison-Wesley Publishing Company, Inc., 1963.

2. Scott, R. F., Lecture Notes on Soil Mechanics, 1966, revised 1969, 1971.

3. Scott, R. F., Professor of Civil Engineering, Caltech, private communication.

4. Taylor, D. W., Fundamentals of Soil Mechanics, John Wiley and Sons, Inc., 1948.

5. Carslaw, H. S. and Jaeger, J. C., Conduction of Heat in Solids, 2nd edition, Oxford University Press, 1959.

6. Brinn, M. S., et al., "Heat Transfer to Granular Materials", Industrial and Engineering Chemistry, vol. 40, no. 4, 1948.

7. Sullivan, W. N., Ph. D. Thesis, Caltech, 1973.

8. Jumkis, A. R., Thermal Soil Mechanics, Rutgers University Press, 1966.

9. "Potters Technical Quality Glass Beads", Potters Industries, Inc., No. 471, 1974.

10. Skinner, A. E., "A Note on the Influence of Interparticle Friction on the Shearing Strength of a Random Assembly of Spherical Particles", Geotechnique, vol. 19, 1969, pp. 150-156.

11. Courant, R. and Hilbert, D., Methods of Mathematical Physics, vol. 2, Interscience Publishers, 1962.

12. Sokolovski, V. V., Statics of Soil Media, Butterworth Scientific Publications, 1960.

TABLE B-1.
MATERIAL PROPERTIES

Material	Bulk Specific Gravity	Particle Specific Gravity	Critical Void Ratio	Mean Dia. (mils)	1 Std. Dev.Dia. (mils)	(internal) friction angle	δ-Lucite (surface) friction angle	δ-Aluminum (surface) friction angle	Thermal diffusivity ×10⁶ (ft²/sec)	Thermal conductivity (BTU/hr ft°F)
P-0140	1.50	2.47	.65	10.7	1.8	18.2	15.7		1.86	.13
P-0170	1.46	2.47	.69	12.8	1.6	24.6	15.3	17.7	1.80	.12
P-0280	1.48	2.47	.67	23.3	2.2	24.3	14.4	15.1	1.87	.13
V-070	1.71	2.92	.71	52.2	4.5	26.8	14.2	15.1	1.71	.11
V-160	1.66	2.92	.76	127.2	6.9	31.7	12.9		1.88	.12
Mustard Seed	.71	1.22	.72	81.4	7.7	38.2	12.0		.86	.08
Sand No. 1	1.56	2.67	.71	8.8	2.9	24.1	20.2		2.63	.18
Sand No. 2	1.30	2.67	1.05	12.5	2.8	30.7	17.9		2.22	.12
Sand No. 3	1.53	2.67	.75	26.8	4.3	30.6	14.4	24.5	2.47	.16

PRESSURE

VOLUME
CHANGE

UNLOADING

R

RELOADING

A
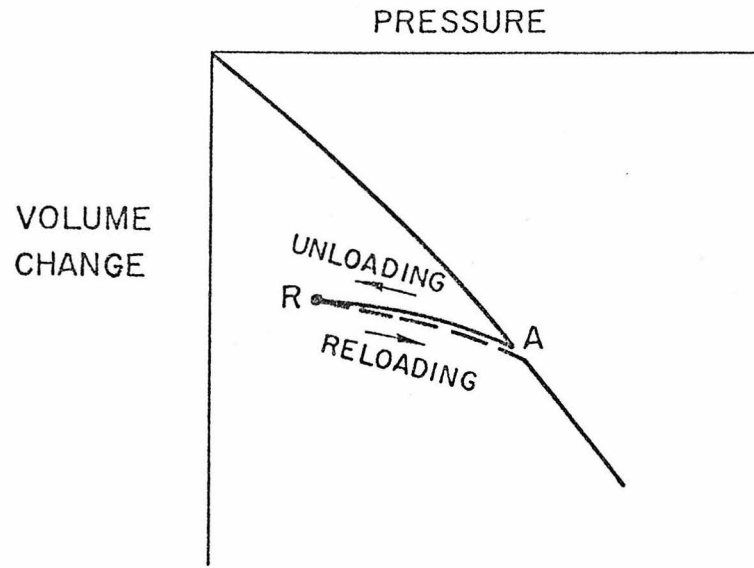
Figure 2. 1. 1   Hydrostatic pressure versus volume change for
the drained, triaxial test of a saturated clay.

σ_3

σ_3

σ_2

σ_1

$\sqrt{2}\, c \cot \phi_1$

$c \cot \phi_1$

$\sigma \sqrt{3}$

$\sigma_1 \sqrt{2} = \sigma_2 \sqrt{2}$

$\sqrt{3}\, c \cot \phi_1$
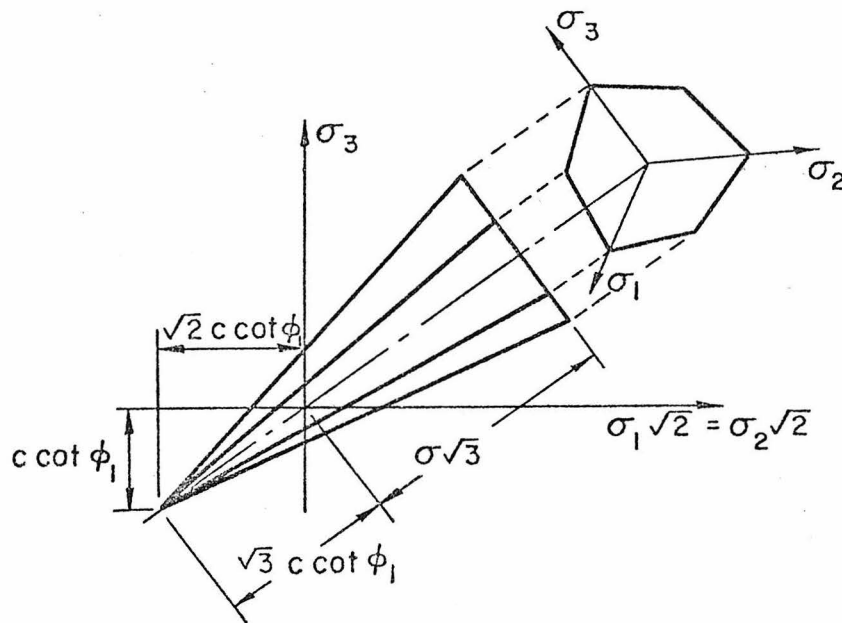
Figure 2. 1. 2   Jenike — Shield pyramid yield surface.
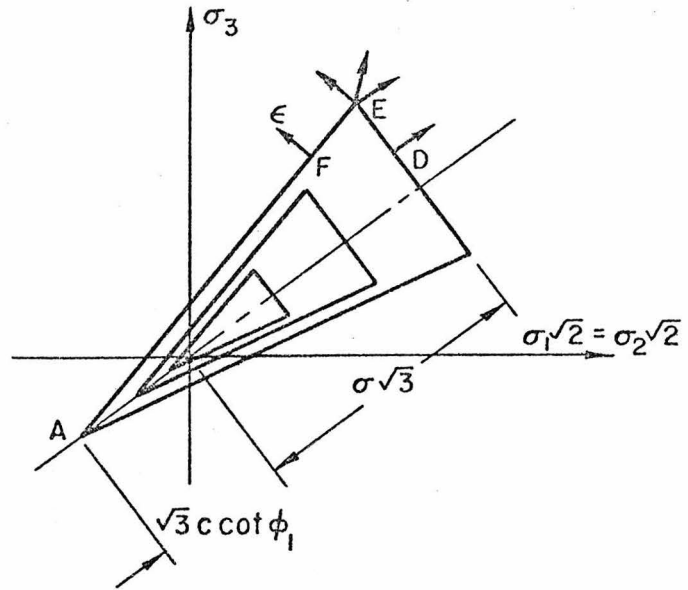
Figure 2.1.3 Growth (contraction) of yield surface for the process of consolidation (expansion).
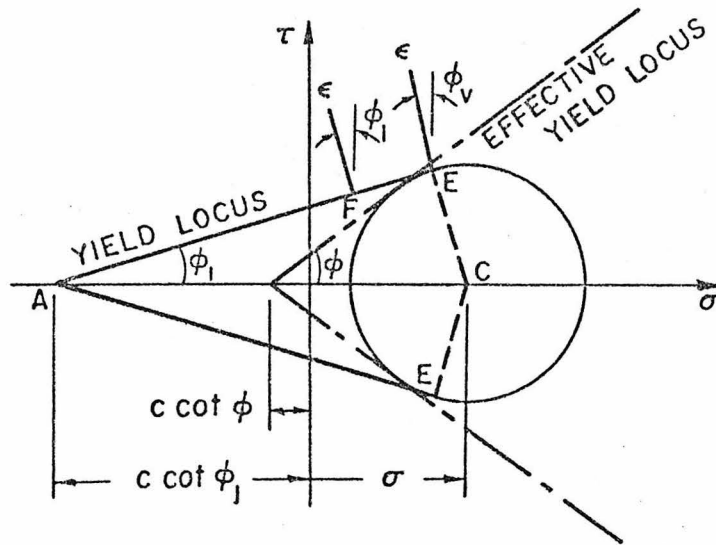
Figure 2.1.4 Yield locus and Jenike — Shield effective yield locus in (σ, τ) coordinates.
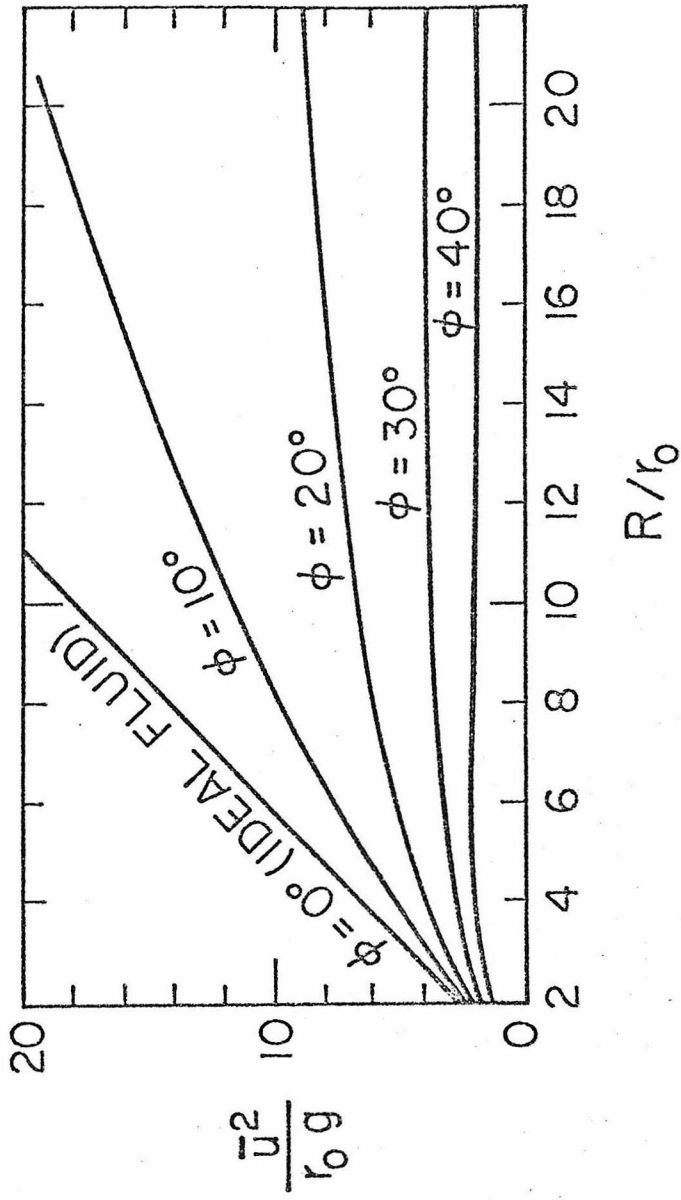
Figure 2.2.1 Dimensionless exit velocity versus dimensionless material head for various internal friction angles.
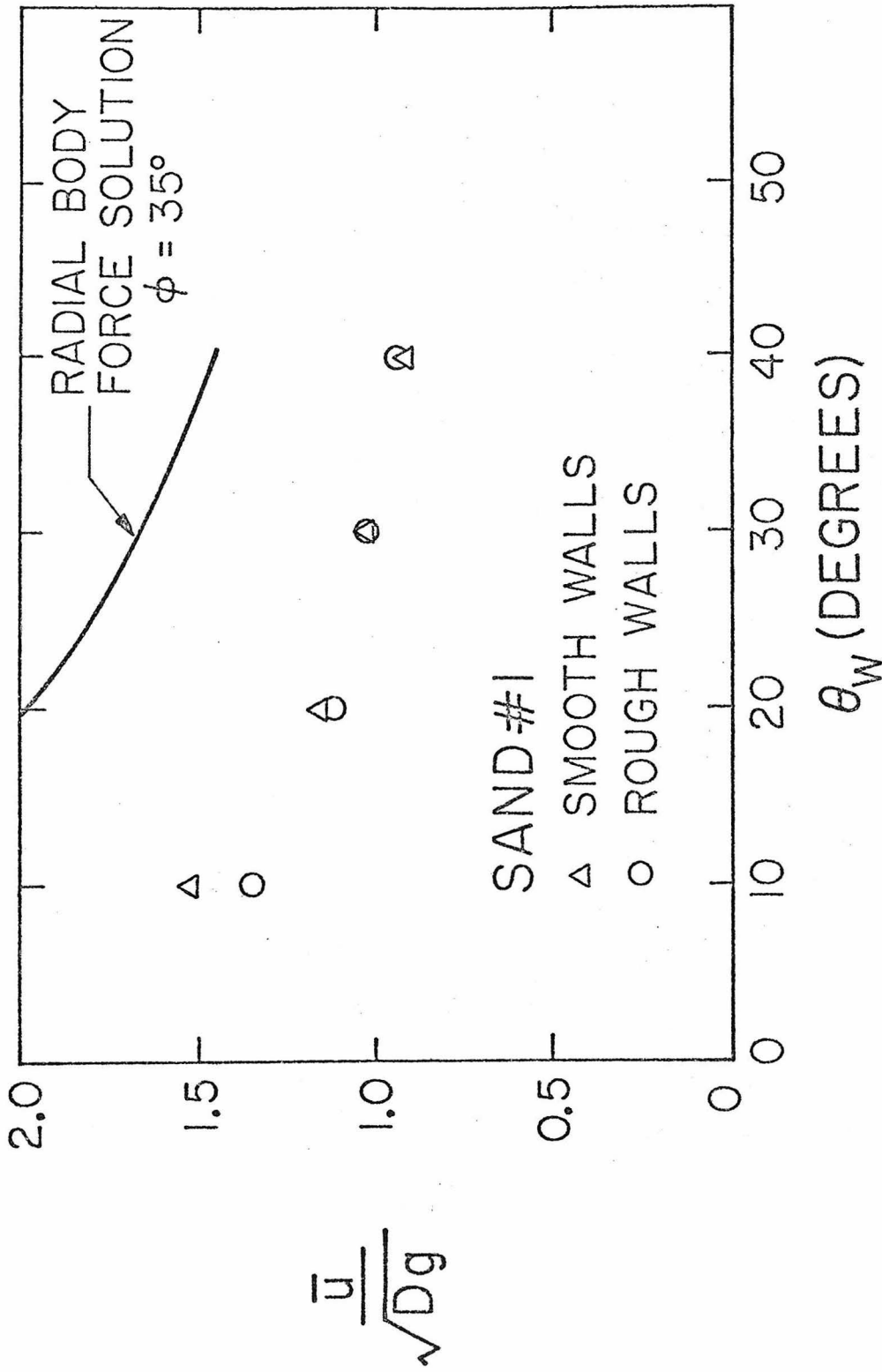
Figure 2.2.2 Dimensionless exit velocity for sand ($\varphi = 35°$) versus channel opening angle.
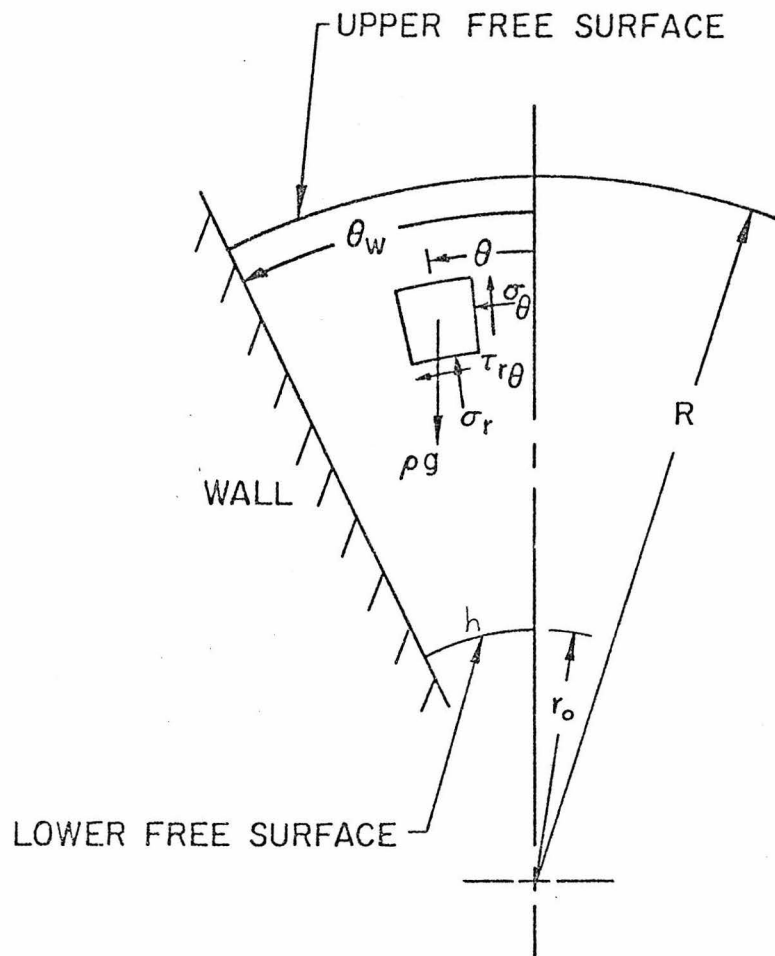
Figure 2.3.1 Plane, symmetric converging channel.
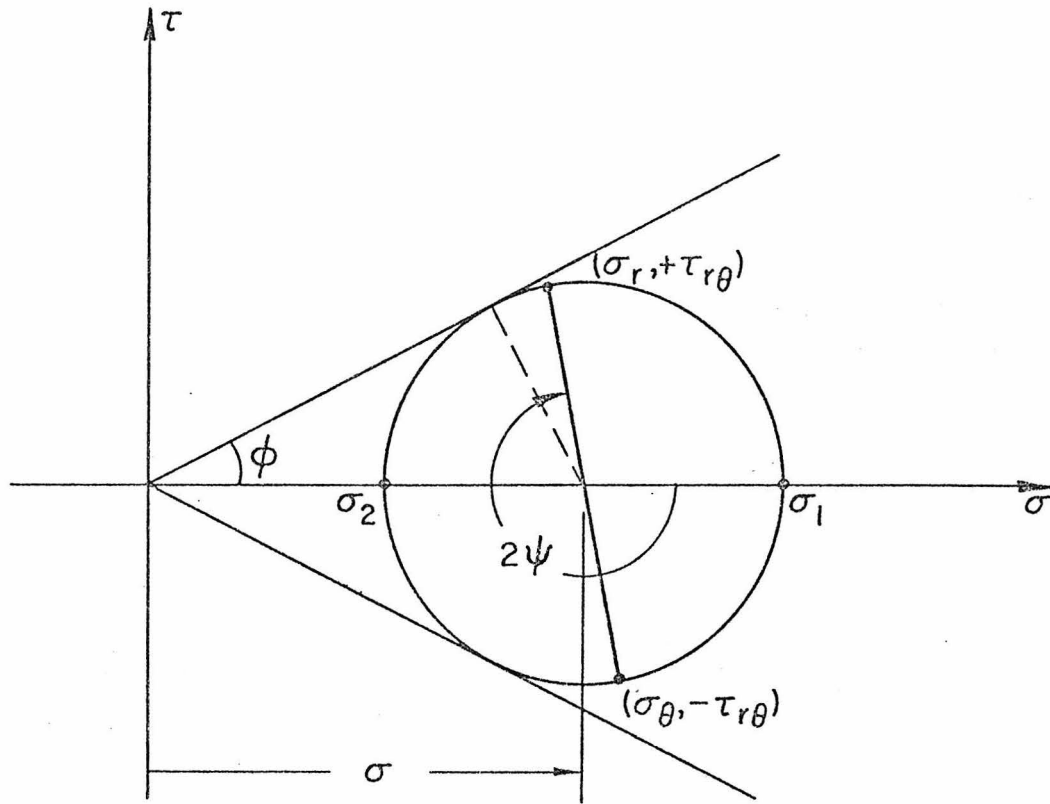
Figure 2.3.2 Mohr diagram and Mohr envelope
with effective friction angle, φ.
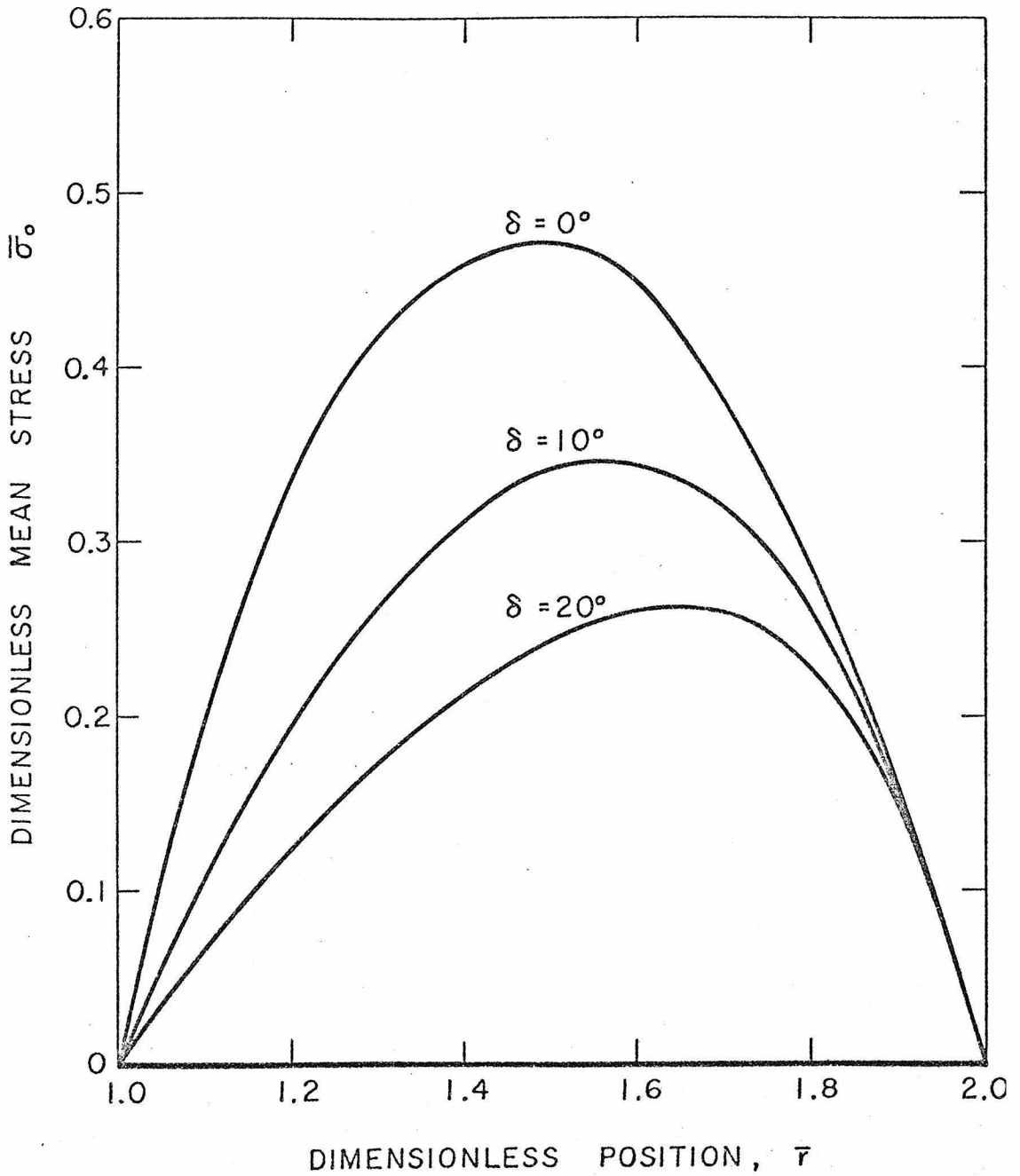
Figure 2.3.3 Mean stress versus radial position for $\varphi = 35°$, $\frac{R}{r_0} = 2$, $\delta = 0°, 10°, 20°$.
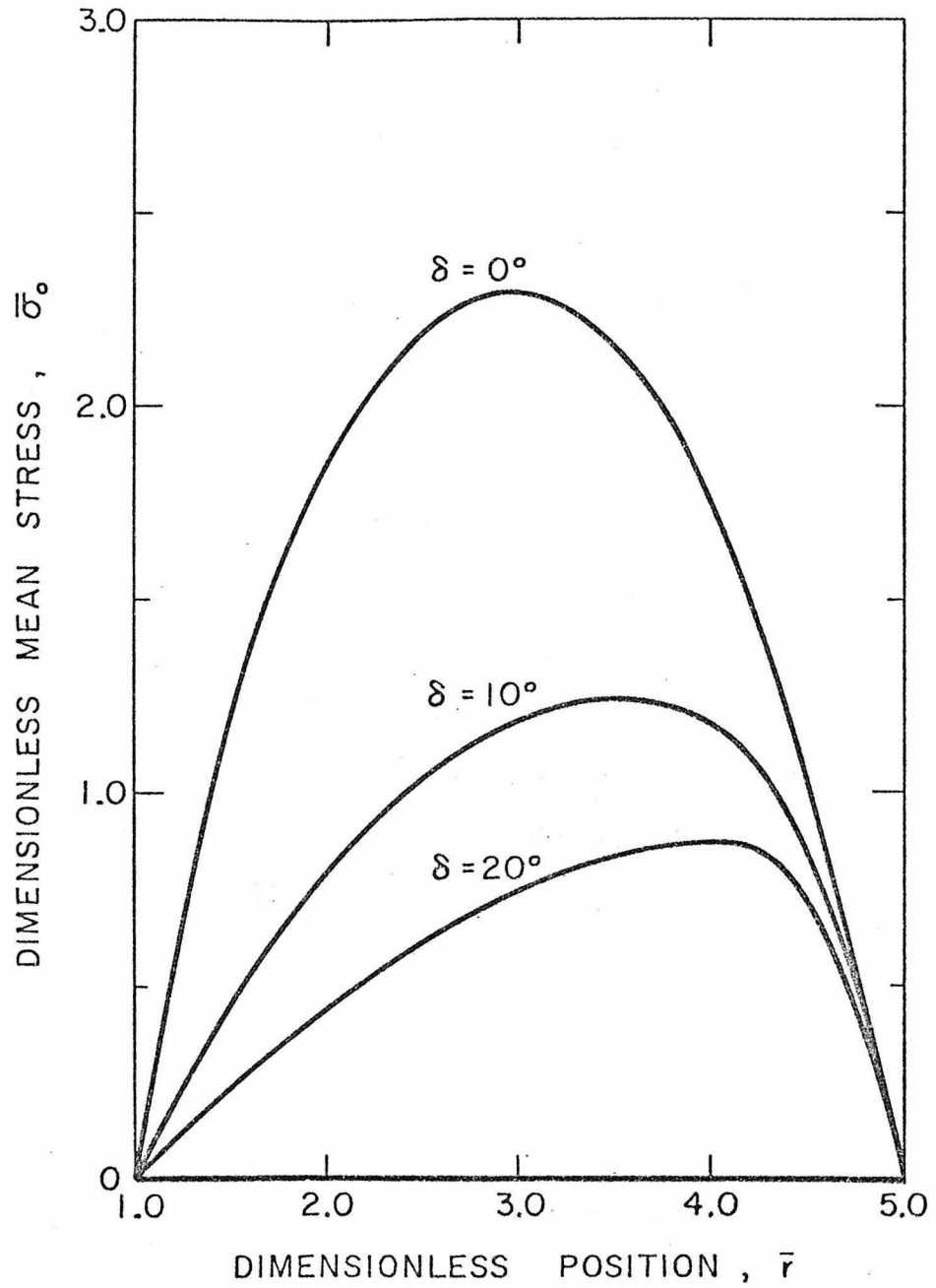
Figure 2.3.4 Mean stress versus radial position for
$\varphi = 35°$, $\dfrac{R}{r_0} = 5$, $\delta = 0°$, $10°$, $20°$.
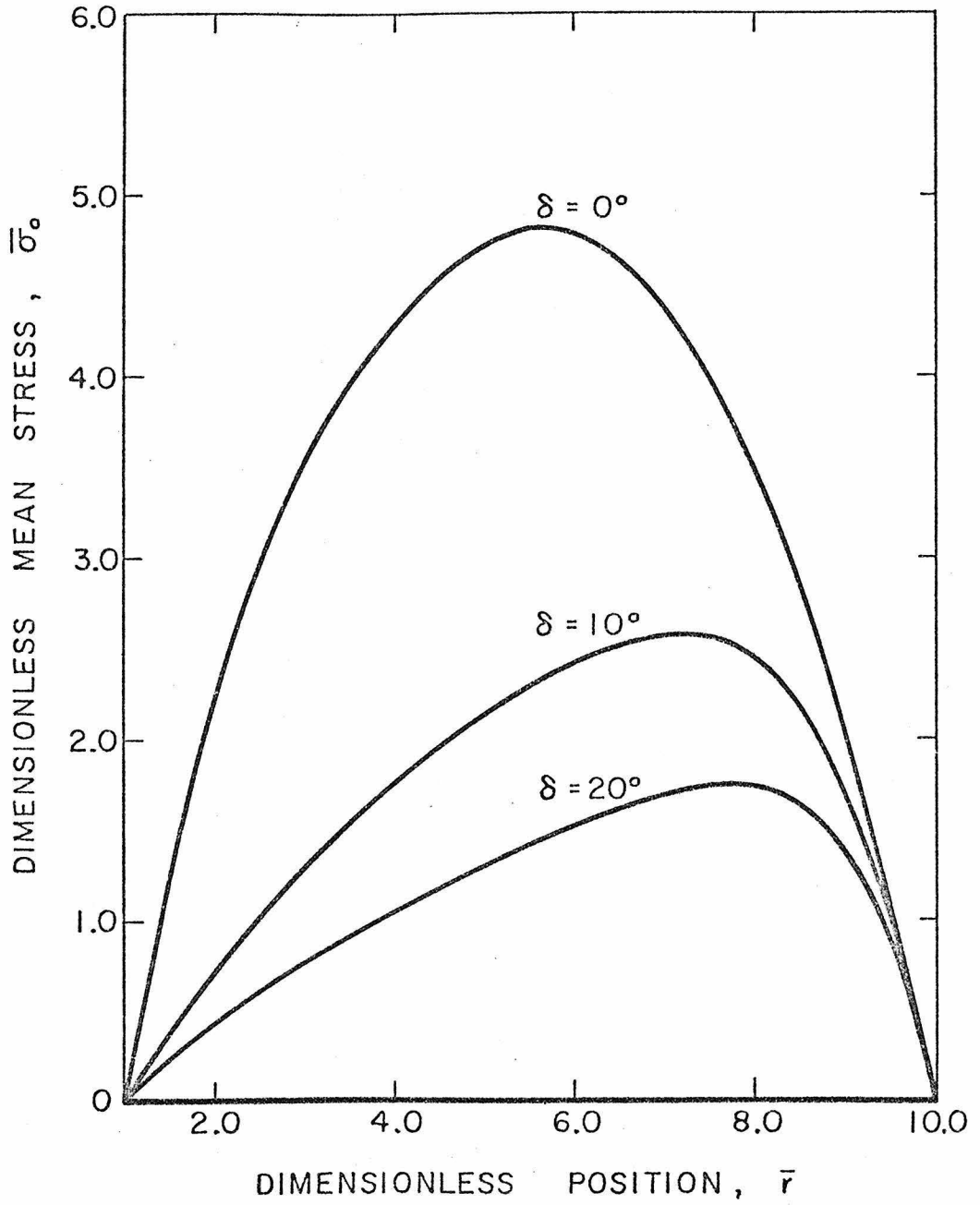
Figure 2.3.5 Mean stress versus radial position for $\varphi = 35°$, $\dfrac{R}{r_0} = 10$, $\delta = 0°$, $10°$, $20°$.
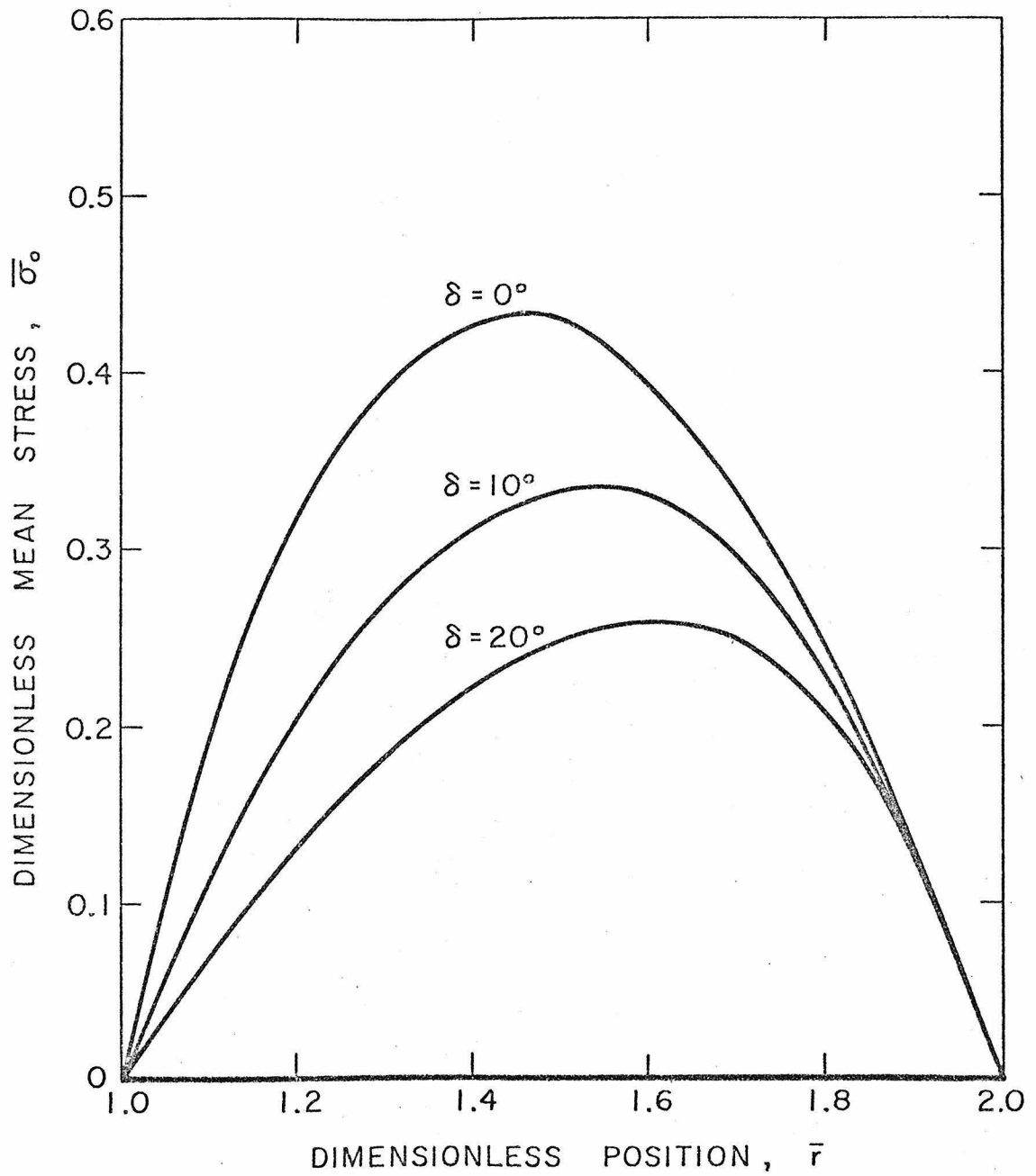
Figure 2. 3. 6   Mean stress versus radial position for
$\varphi = 30°$, $\dfrac{R}{r_0} = 2$, $\delta = 0°$, $10°$, $20°$.
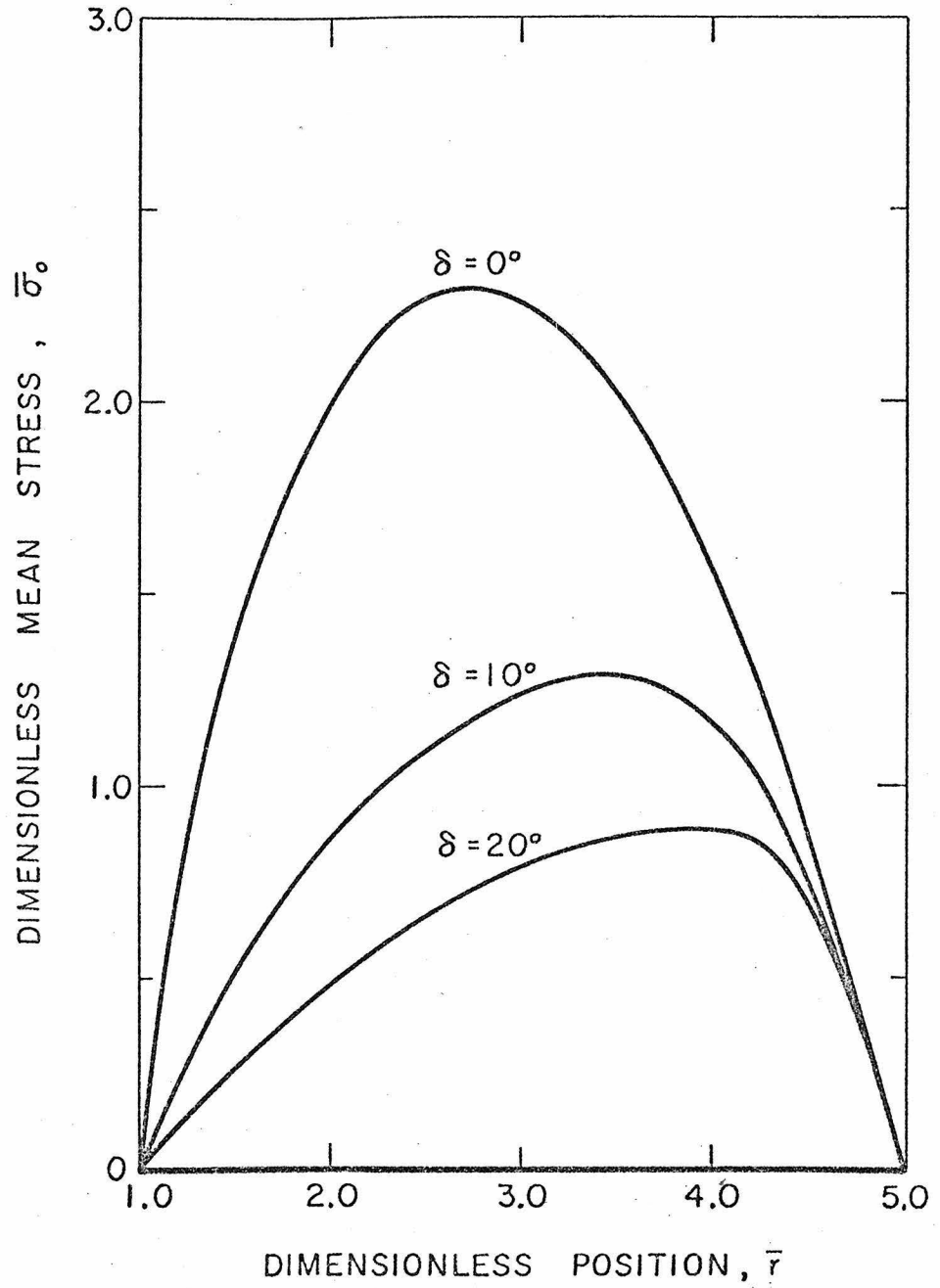
Figure 2.3.7 Mean stress versus radial position for
$\varphi = 30°$, $\dfrac{R}{r_0} = 5$, $\delta = 0°$, $10°$, $20°$.
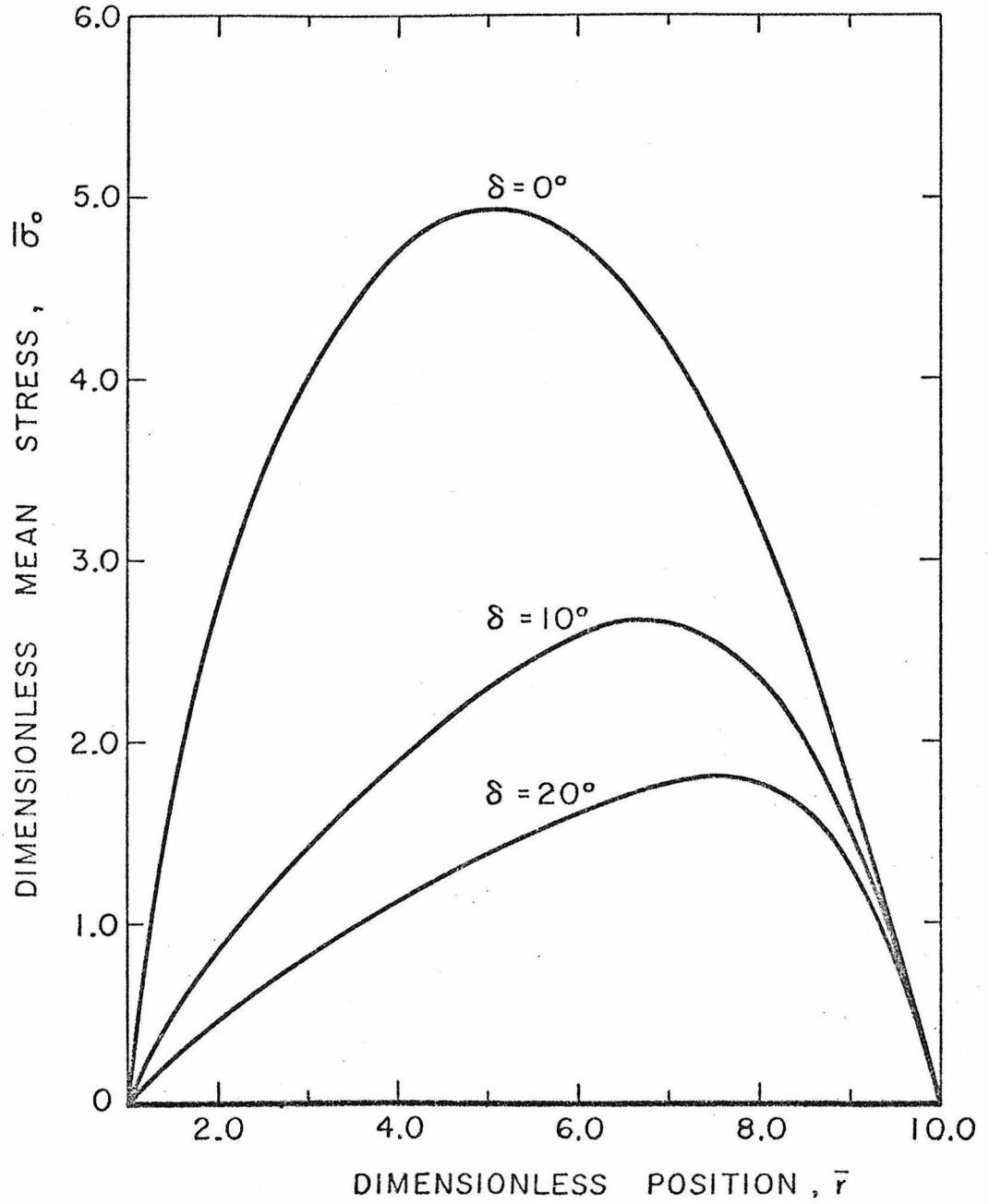
Figure 2.3.8 Mean stress versus radial position for $\varphi = 30°$, $\dfrac{R}{r_0} = 10$, $\delta = 0°$, $10°$, $20°$.
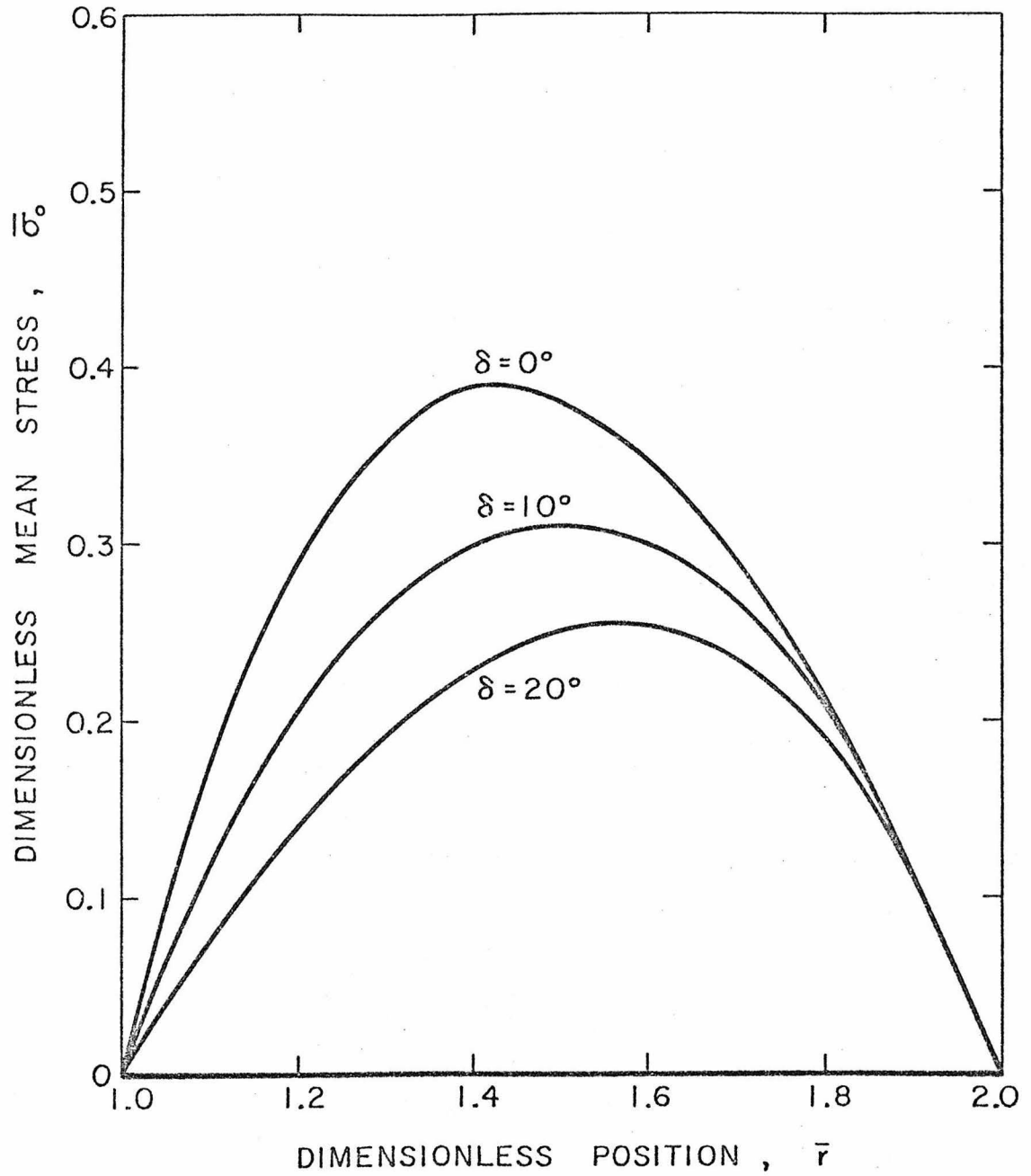
Figure 2.3.9 Mean stress versus radial position for
$\varphi = 25°$, $\dfrac{R}{r_0} = 2$, $\delta = 0°$, $10°$, $20°$.
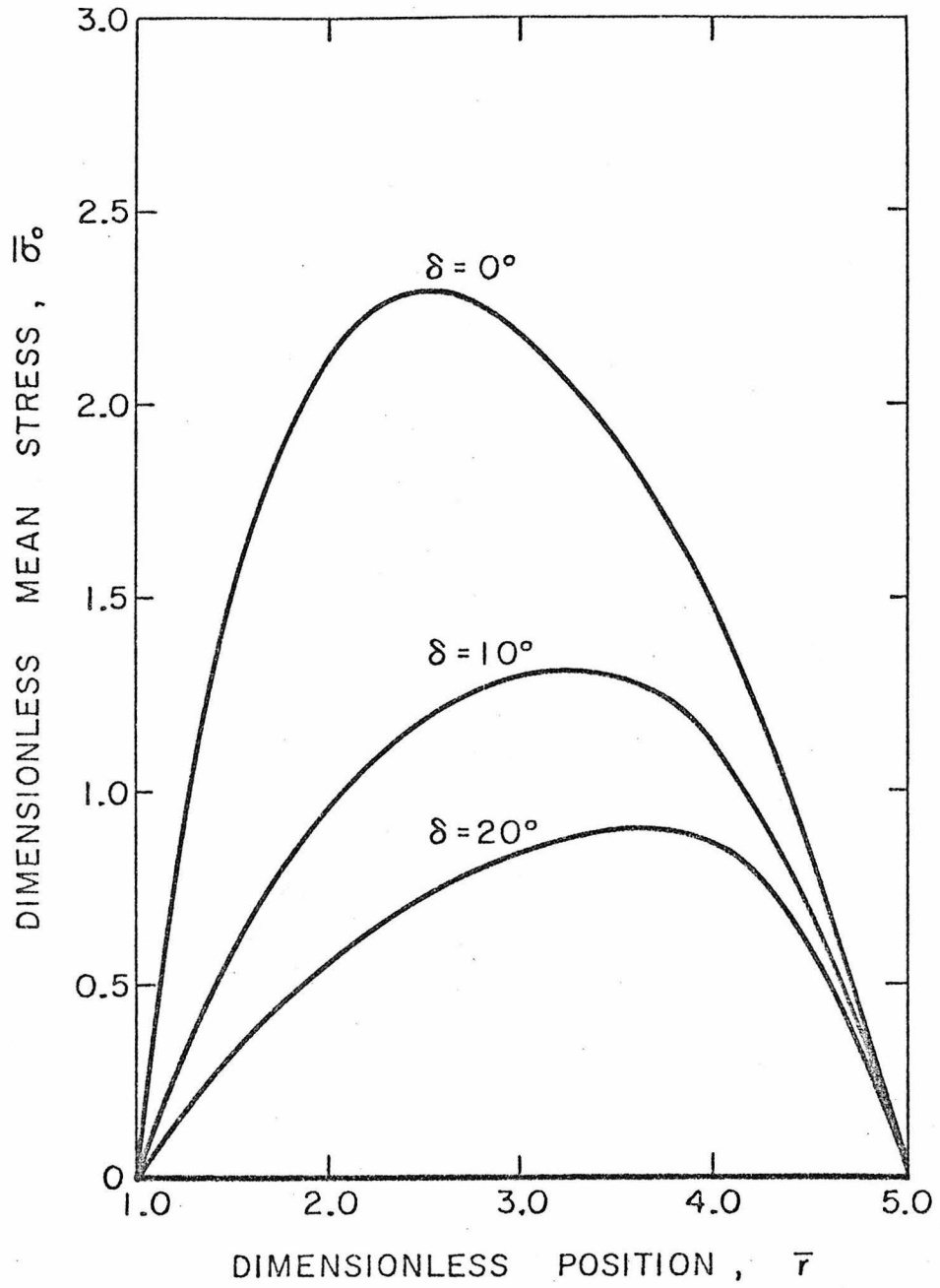
Figure 2.3.10 Mean stress versus radial position for
$\varphi = 25°$, $\dfrac{R}{r_0} = 5$, $\delta = 0°$, $10°$, $20°$.
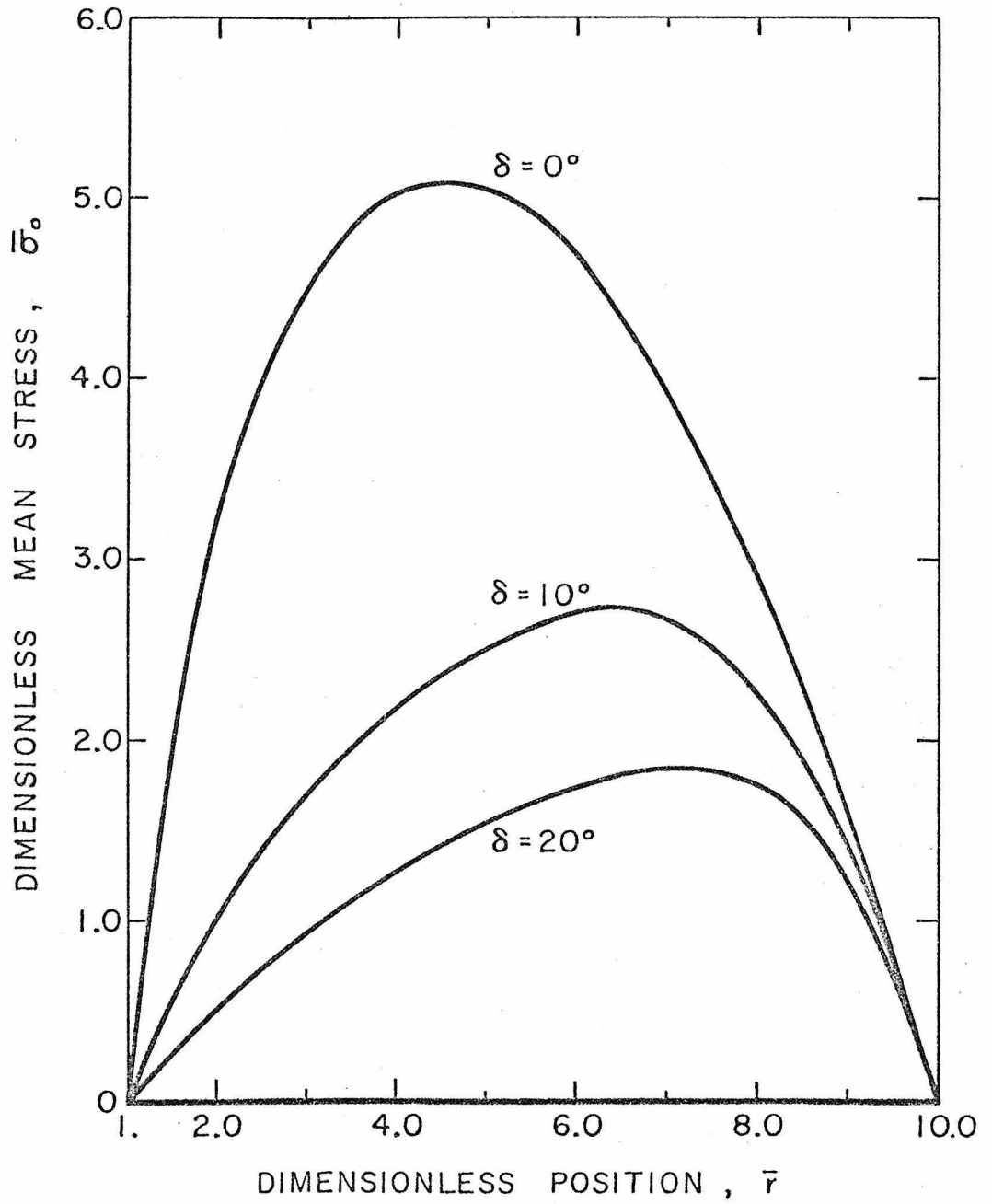
Figure 2.3.11 Mean stress versus radial position for
$\varphi = 25°$, $\frac{R}{r_0} = 10$, $\delta = 0°$, $10°$, $20°$.
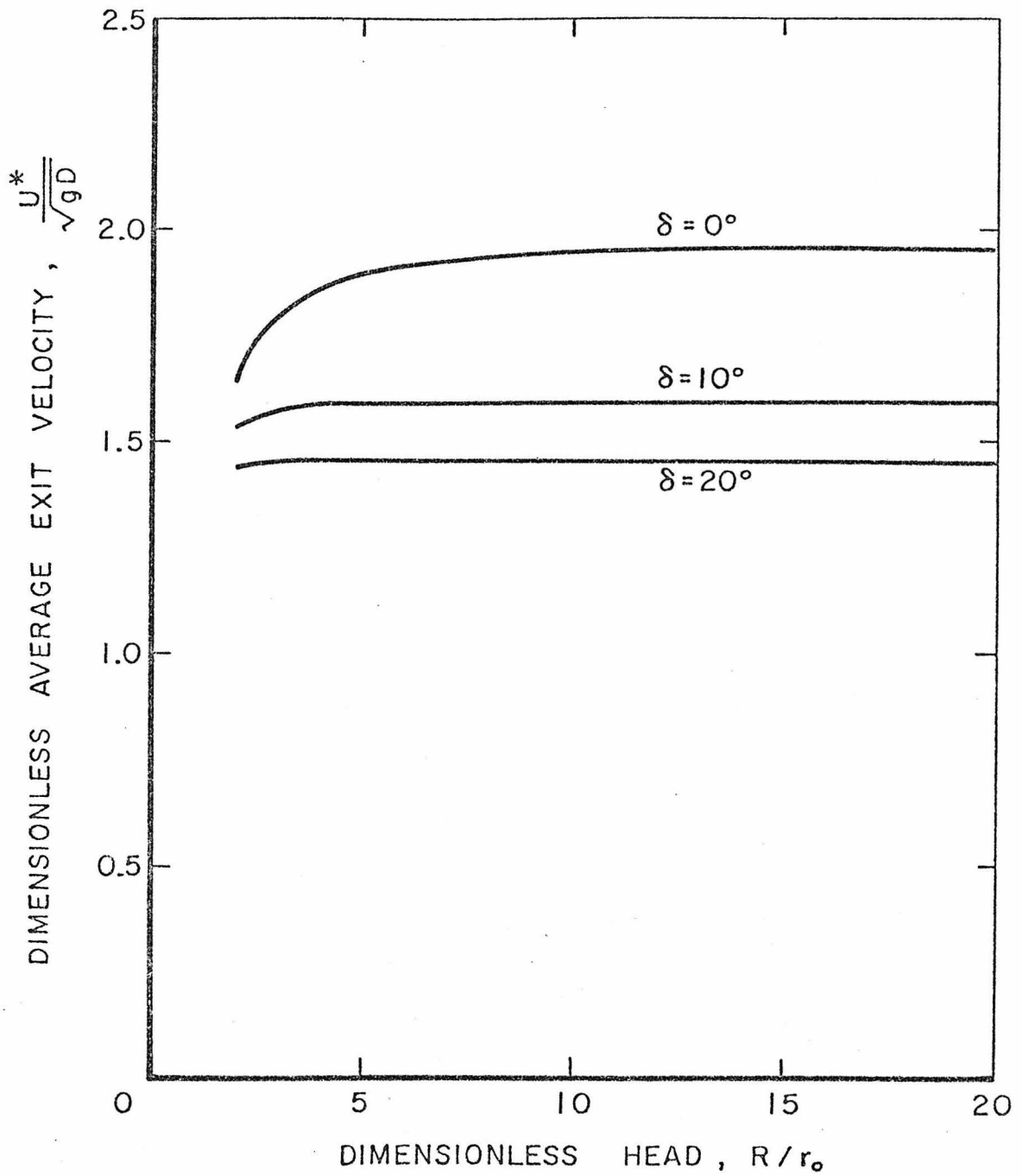
Figure 2.3.12 Average dimensionless exit velocity, $\dfrac{U^*}{\sqrt{gD}}$, versus dimensionless head for $\varphi = 35°$, $\theta_w = 20°$, $\delta = 0°$, $10°$, $20°$.
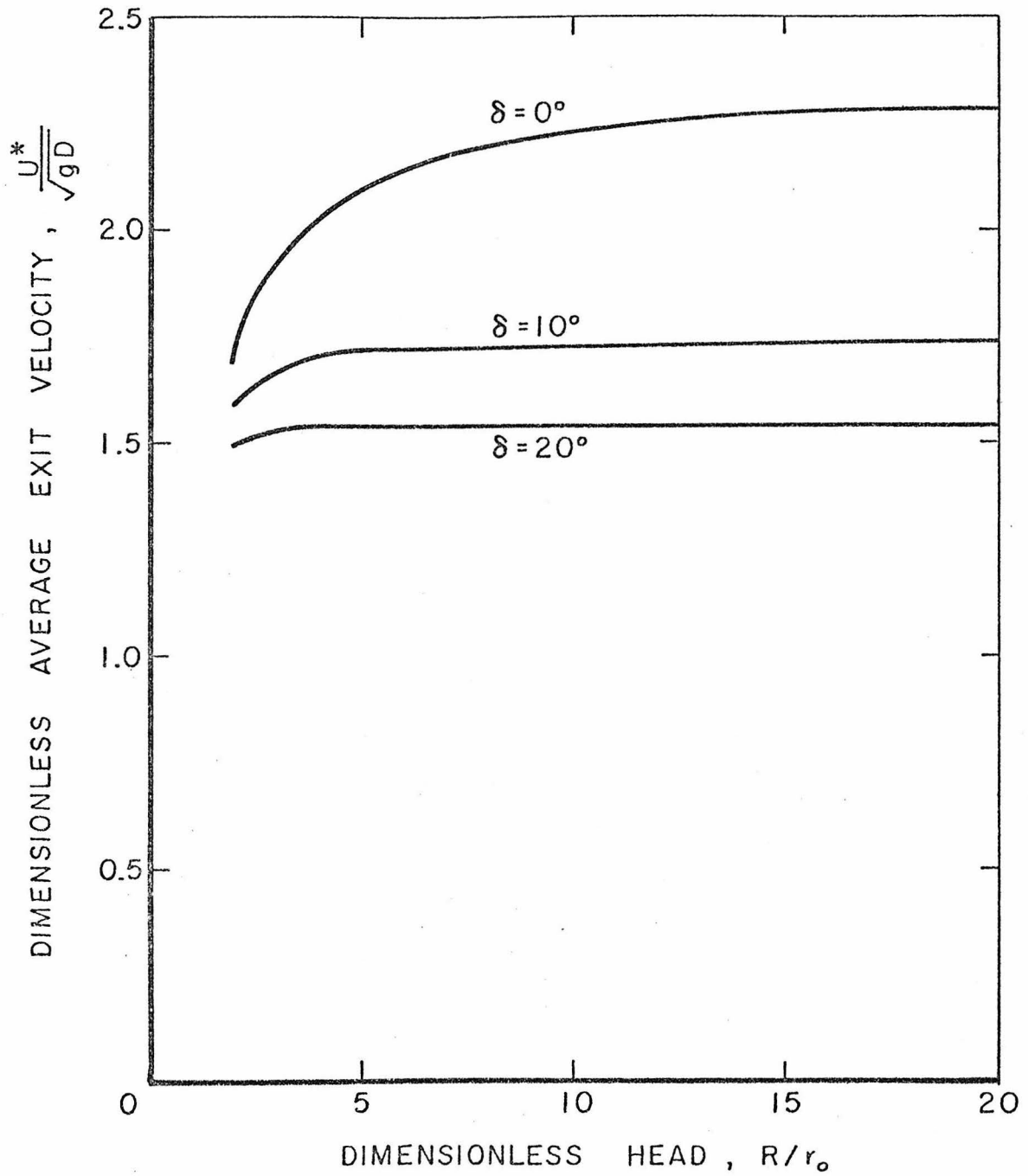
Figure 2.3.13 Average dimensionless exit velocity, $\frac{U^*}{\sqrt{gD}}$, versus dimensionless head for $\varphi = 30°$, $\theta_w = 20°$, $\delta = 0°$, $10°$, $20°$.
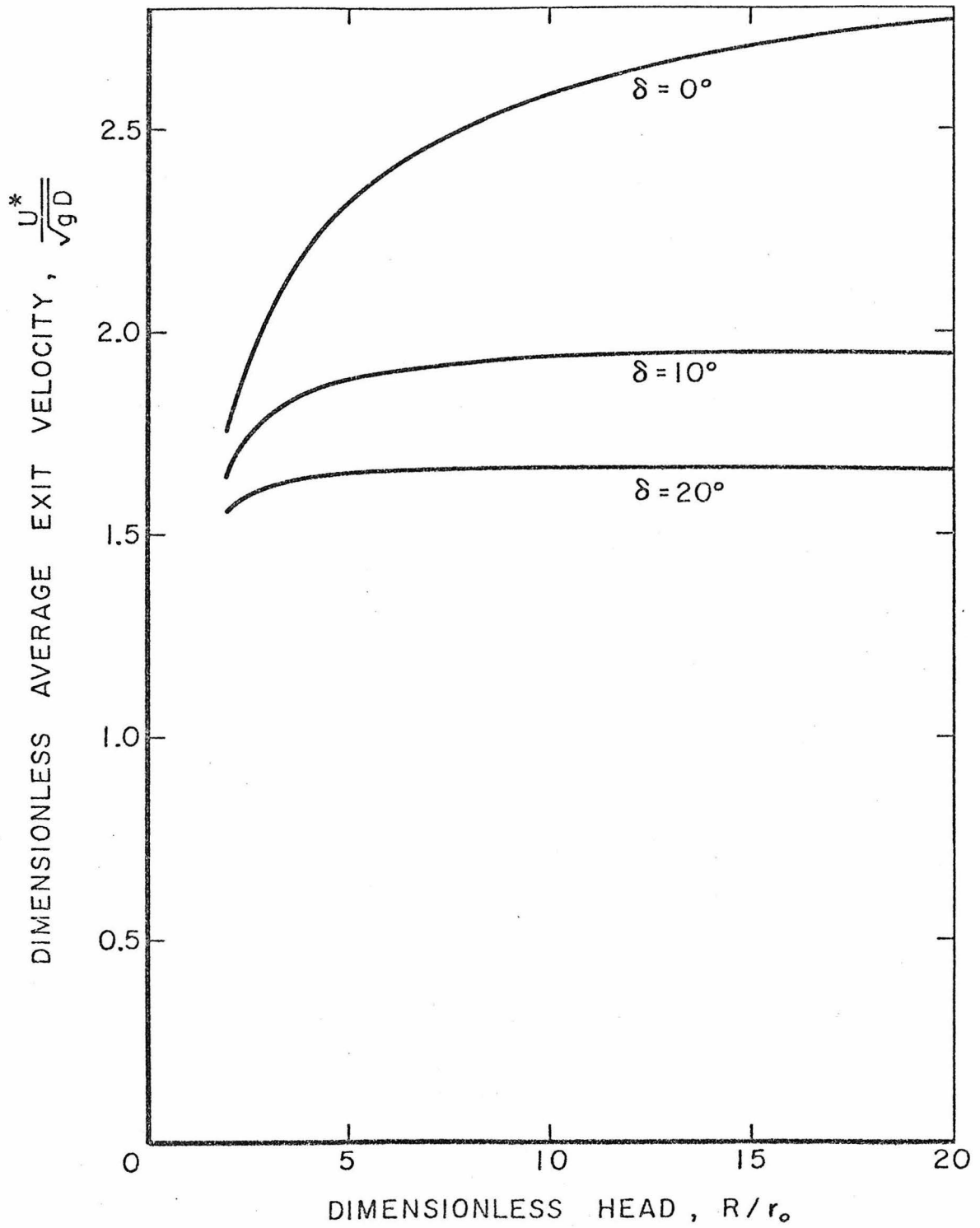
Figure 2.3.14 Average dimensionless exit velocity, $\dfrac{U^*}{\sqrt{gD}}$, versus dimensionless head for $\varphi = 25°$, $\theta_w = 20°$, $\delta = 0°$, $10°$, $20°$.
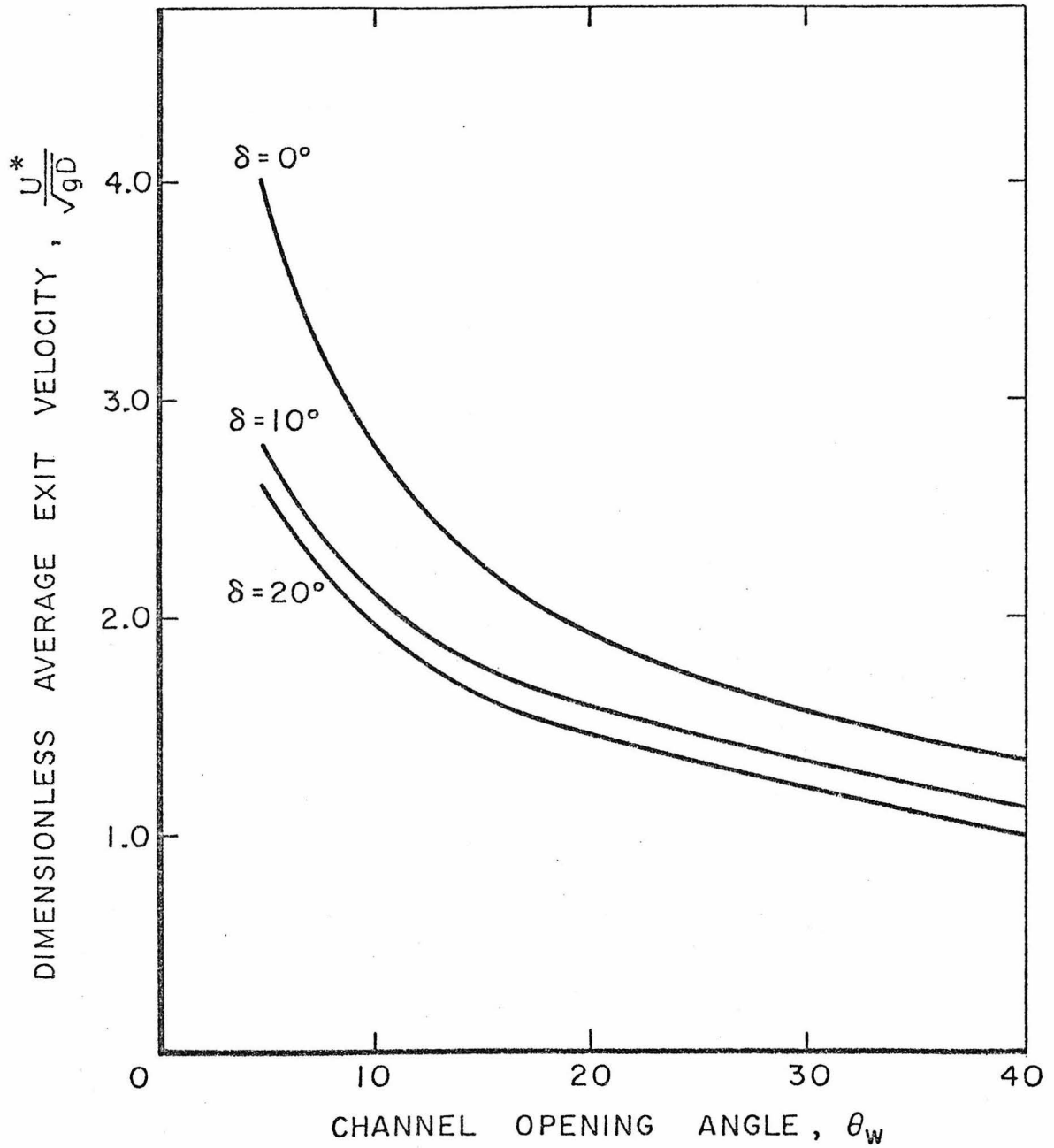
Figure 2.3.15 Average dimensionless exit velocity, $\dfrac{U^*}{\sqrt{gD}}$, versus channel opening angle, θ_w, for $\varphi = 35°$, $\dfrac{R}{r_0}$ large, $\delta = 0°$, $10°$, $20°$.

Figure 2.3.16 Average dimensionless exit velocity, $\dfrac{U^*}{\sqrt{gD}}$, versus channel opening angle, θ_w, for $\varphi = 30°$, $\dfrac{R}{r_0}$ large, $\delta = 0°$, $10°$, $20°$.
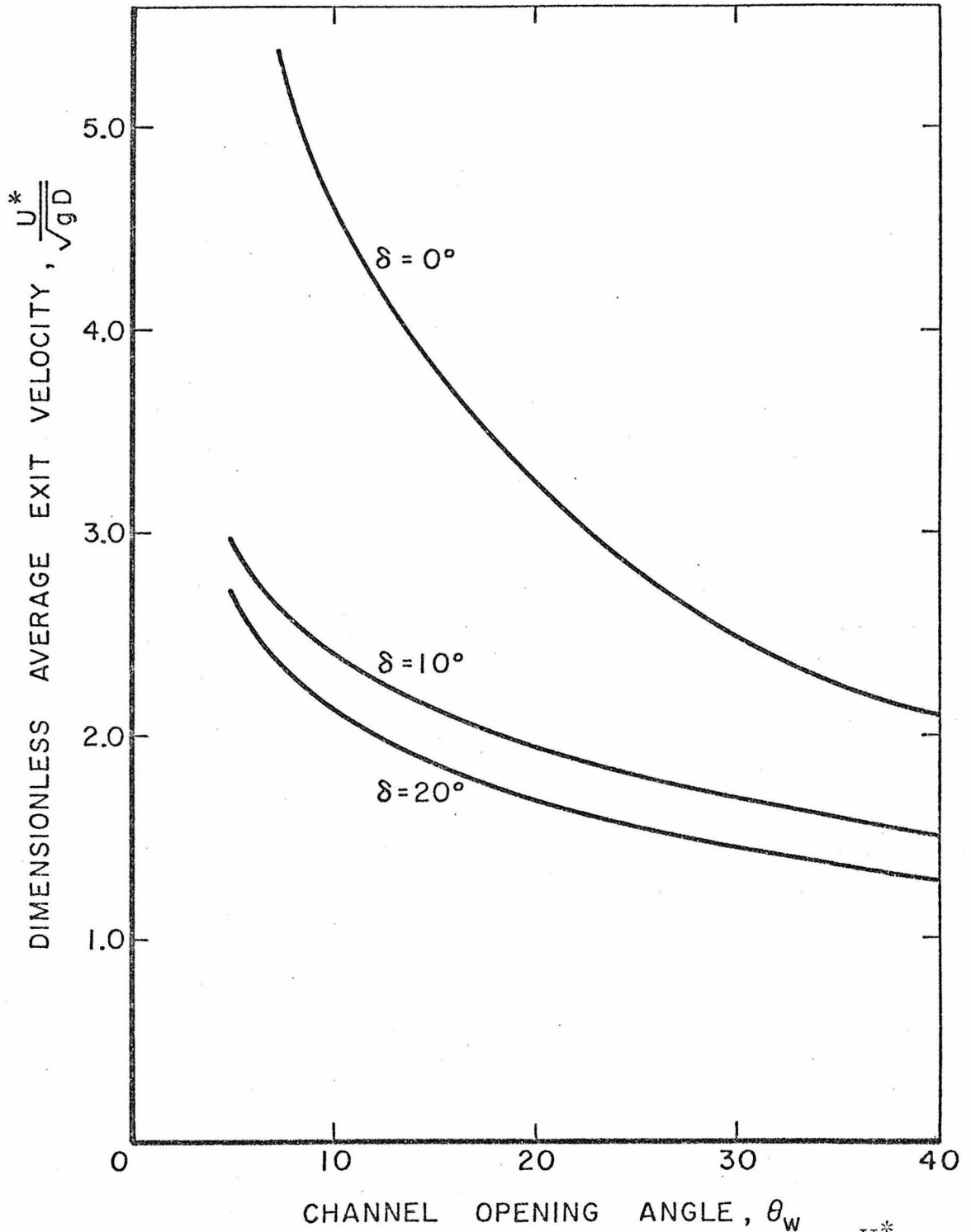
Figure 2.3.17 Average dimensionless exit velocity, $\dfrac{U^*}{\sqrt{gD}}$, versus channel opening angle, θ_w, for $\varphi = 25°$, $\dfrac{R}{r_0}$ large, $\delta = 0°$, $10°$, $20°$.
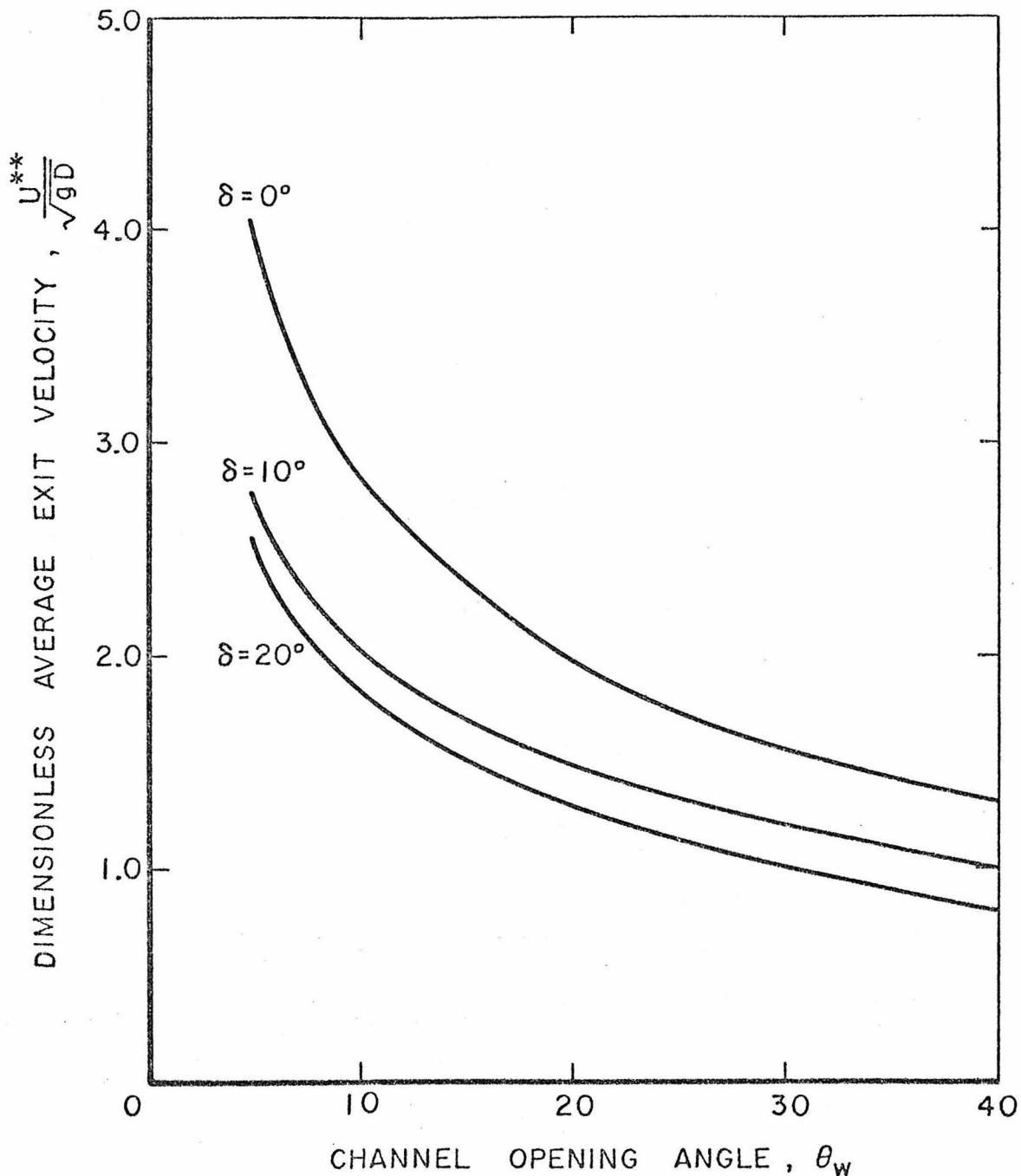
Figure 2.3.18 Average dimensionless exit velocity, $\dfrac{U^{**}}{\sqrt{gD}}$, versus channel opening angle, θ_w, for $\varphi = 35°$, $\dfrac{R}{r_0}$ large, $\delta = 0°$, $10°$, $20°$.

Figure 2.3.19 Average dimensionless exit velocity, $\dfrac{U^{**}}{\sqrt{gD}}$, versus channel opening angle, θ_w, for $\varphi = 30°$, $\dfrac{R}{r_0}$ large, $\delta = 0°$, $10°$, $20°$.
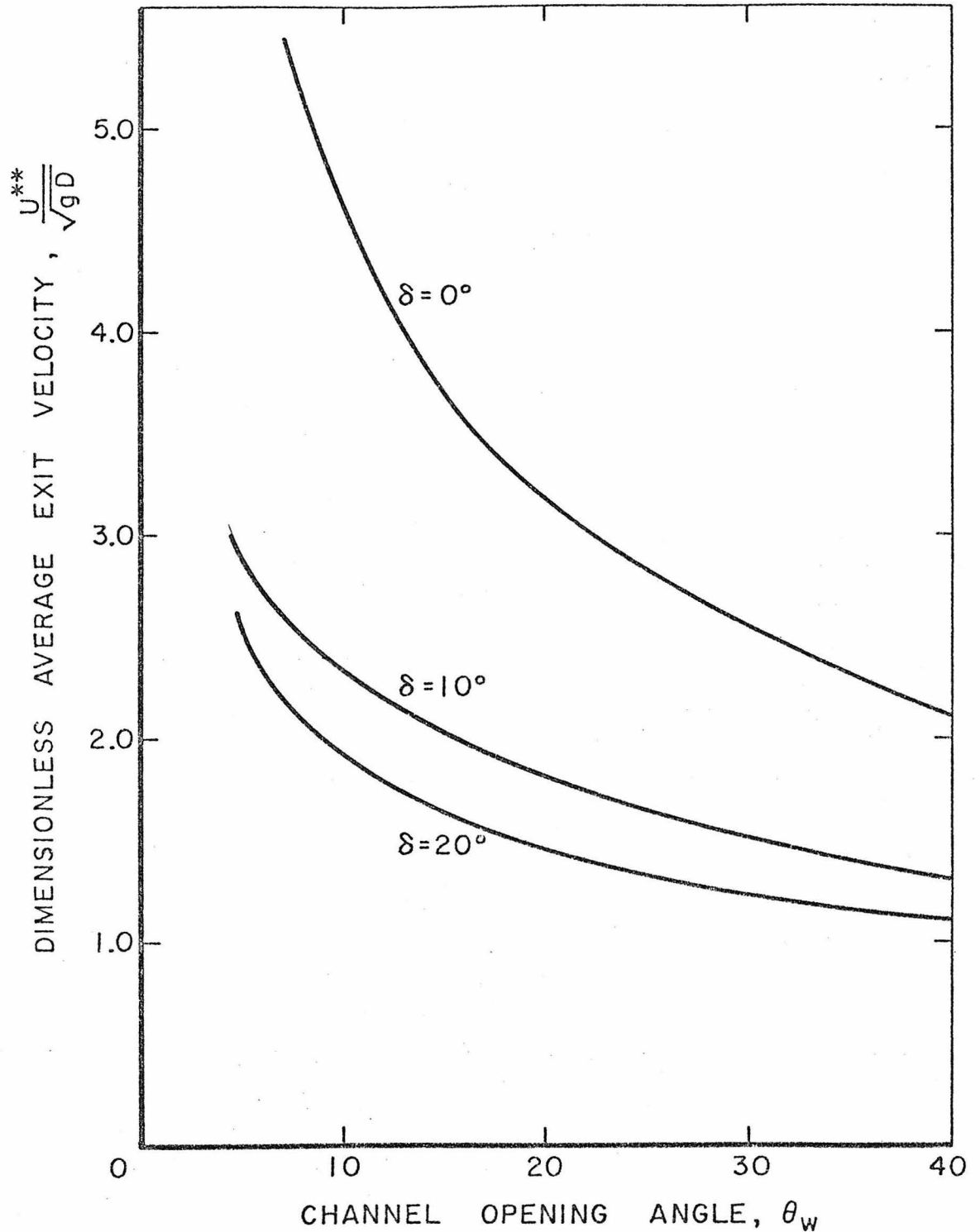
Figure 2.3.20 Average dimensionless exit velocity, $\dfrac{U^{**}}{\sqrt{gD}}$, versus channel opening angle, θ_w, for $\varphi = 25°$, $\dfrac{R}{r_0}$ large, $\delta = 0°$, $10°$, $20°$.
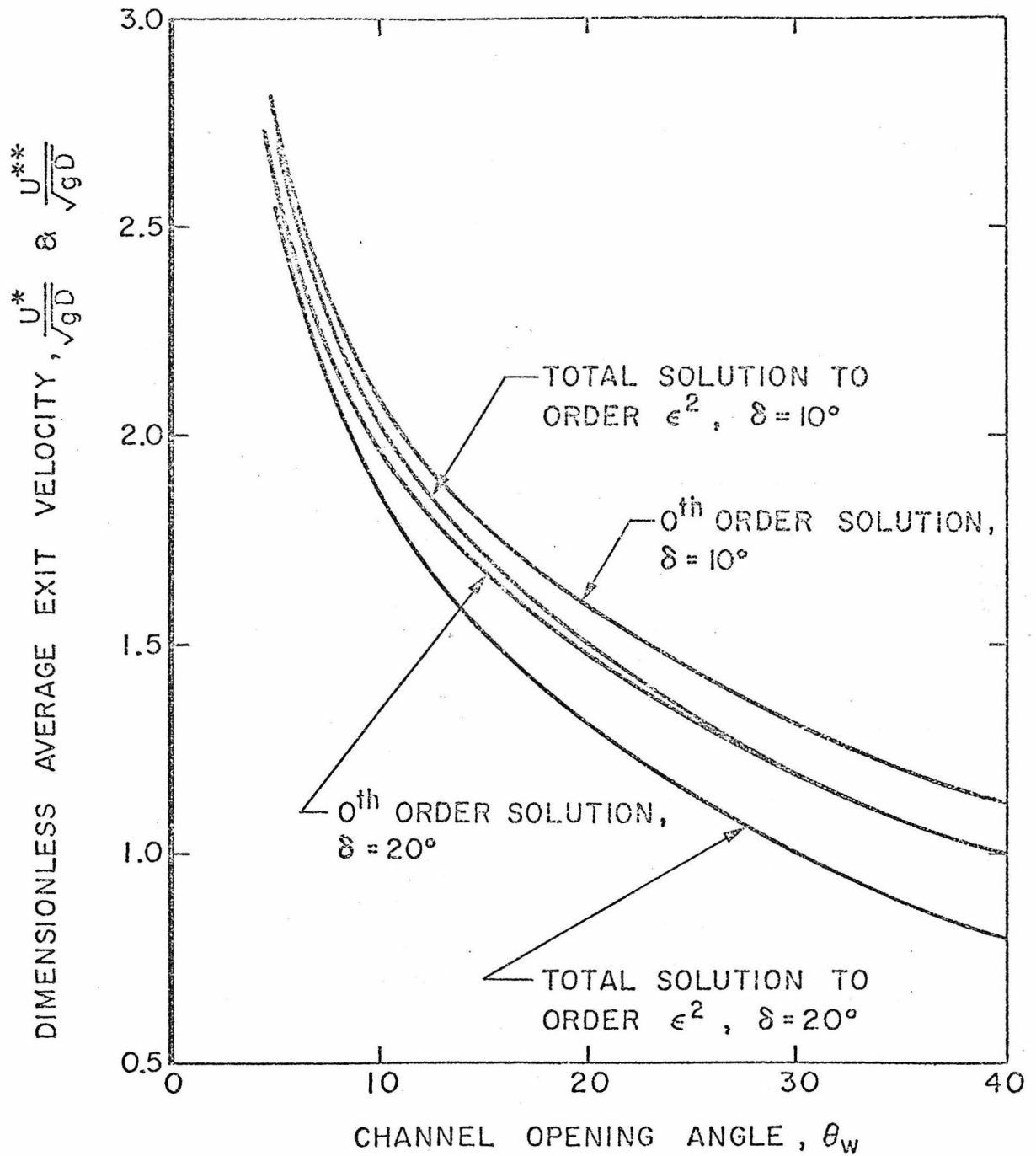
Figure 2.3.21 Average dimensionless exit velocities, $\dfrac{U^*}{\sqrt{gD}}$ and $\dfrac{U^{**}}{\sqrt{gD}}$, versus channel opening angle θ_w for $\varphi = 35°$.

Figure 2.3.22 Dimensionless exit velocity, $\bar{u}_{\bar{r}=1}$, versus angular position, $\bar{\theta}$, for $\varphi = 35°$ and $\bar{\theta}_w = 32.5°$.
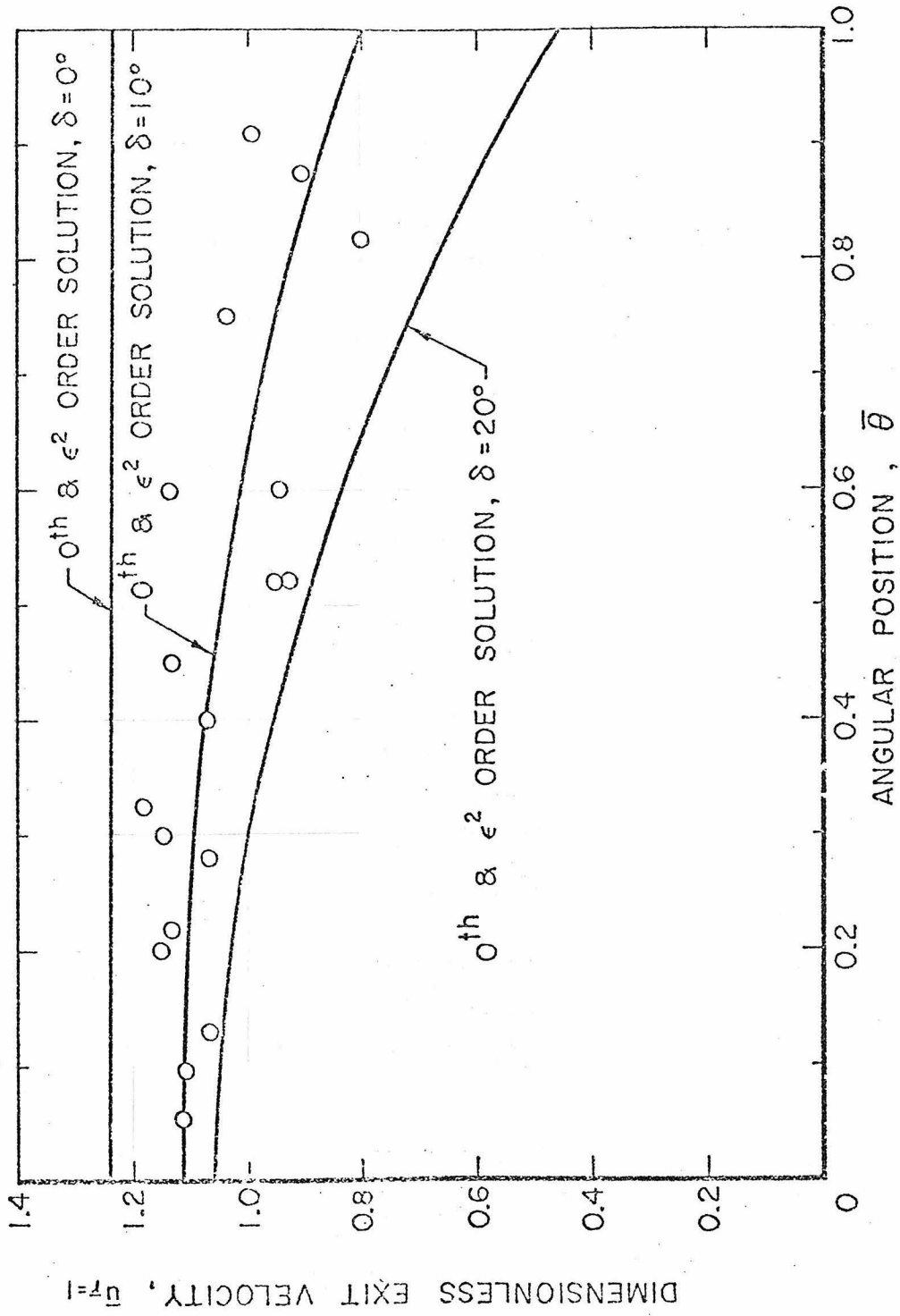
Figure 2.3.23 Dimensionless exit velocity, $\bar{u}_{\bar{r}=1}$, versus angular position, $\bar{\theta}$, for $\varphi = 40°$ and $\theta_w = 32.5°$.
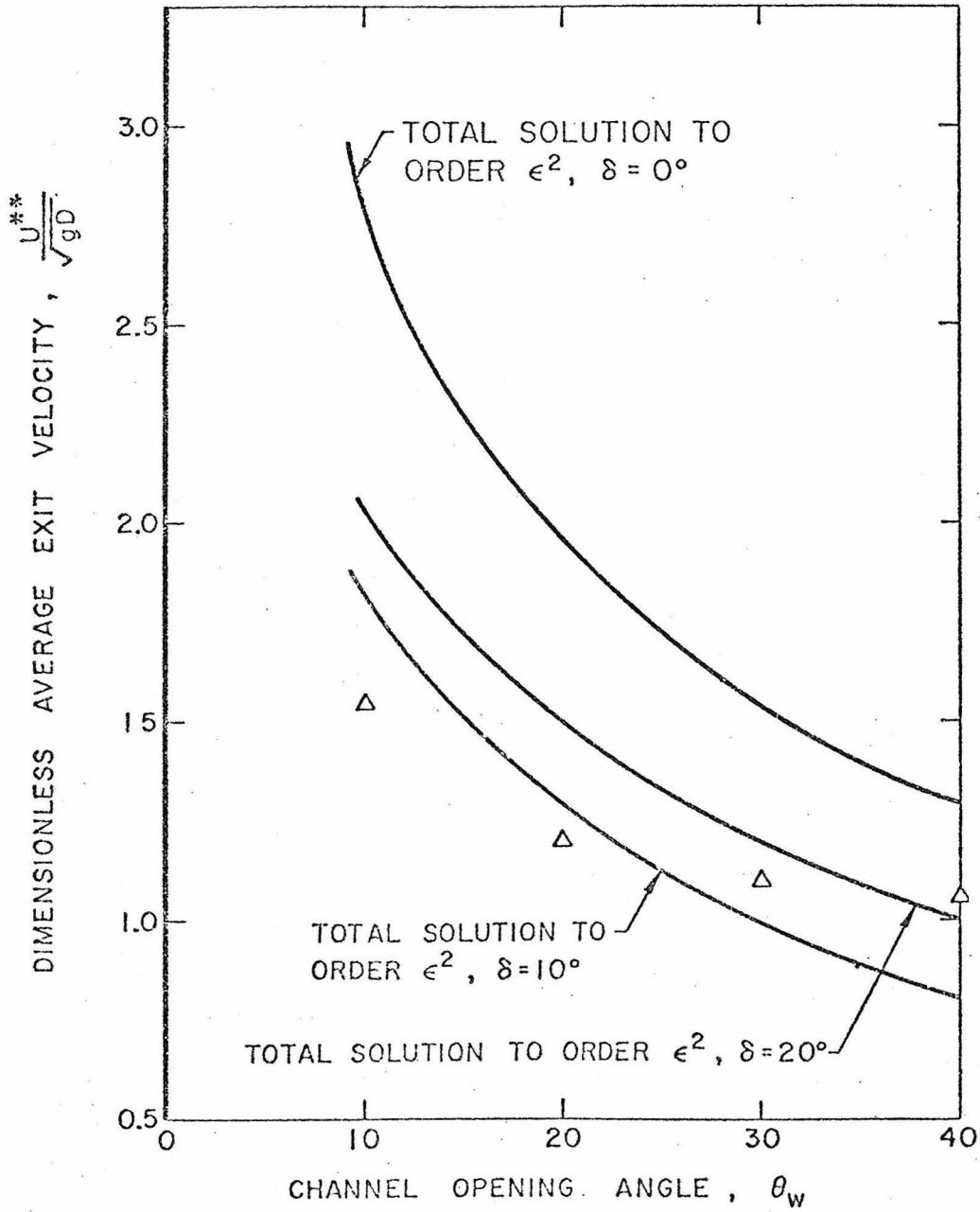
Figure 2.3.24 Average dimensionless exit velocity, $\dfrac{U^{**}}{\sqrt{gD}}$, versus channel opening angle, $\dot{\theta}_w$, for $\varphi = 35°$.
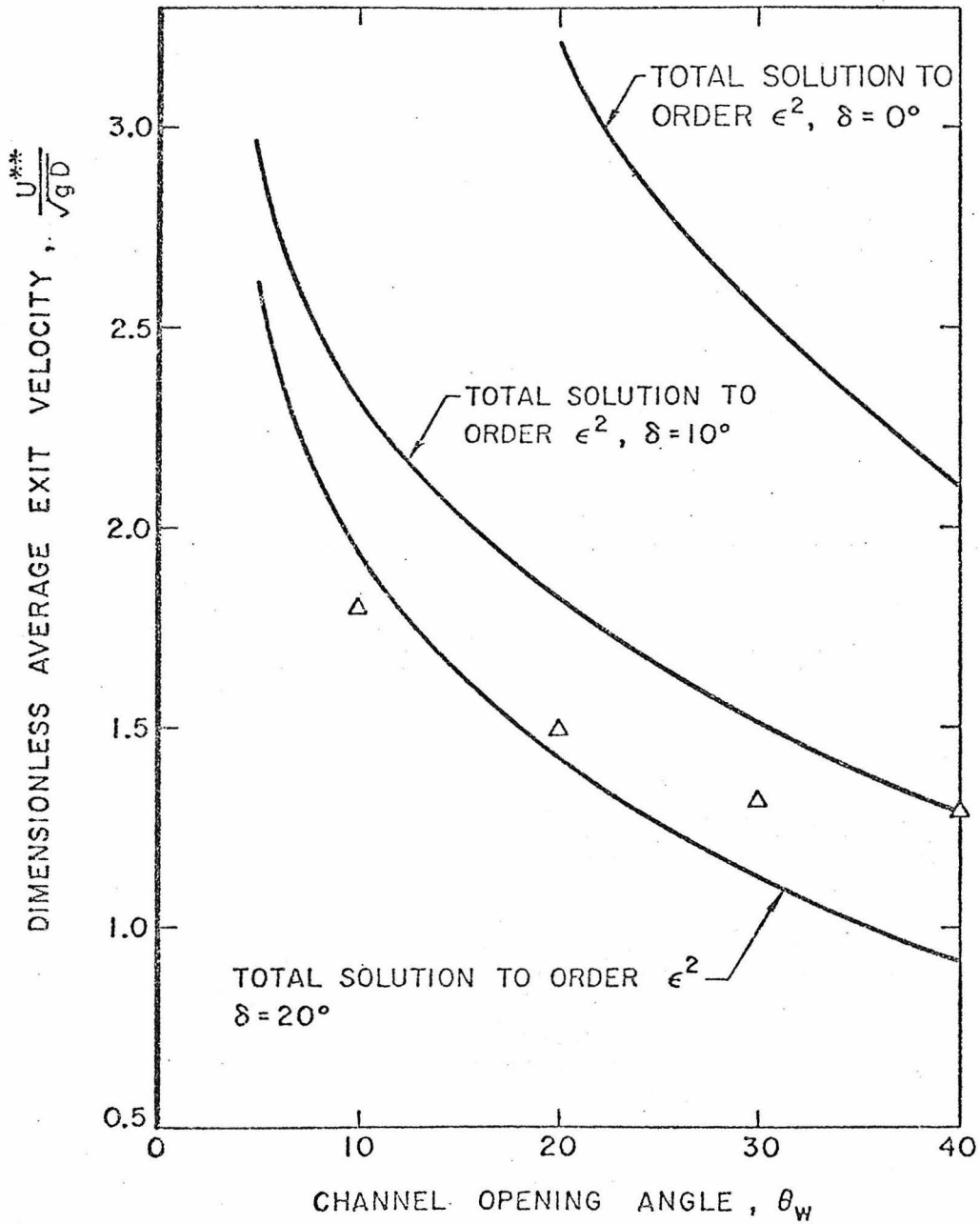
Figure 2.3.25 Average dimensionless exit velocity, $\dfrac{U^{**}}{\sqrt{gD}}$, versus channel opening angle, θ_w, for $\varphi = 25°$.
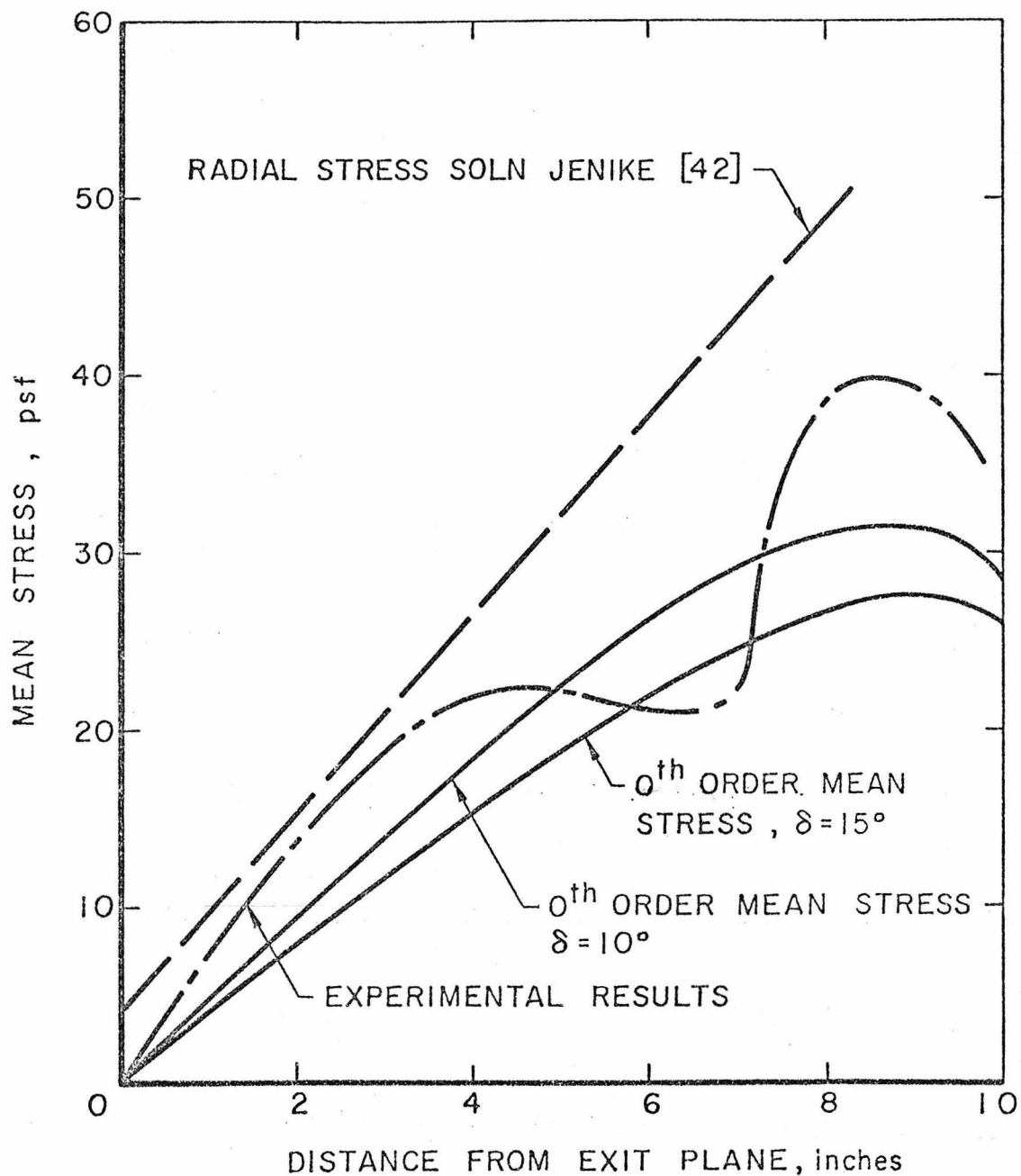
Figure 2.3.26 Wall mean stress, $\overline{\sigma}_0$, versus radial position, $\overline{r}$.
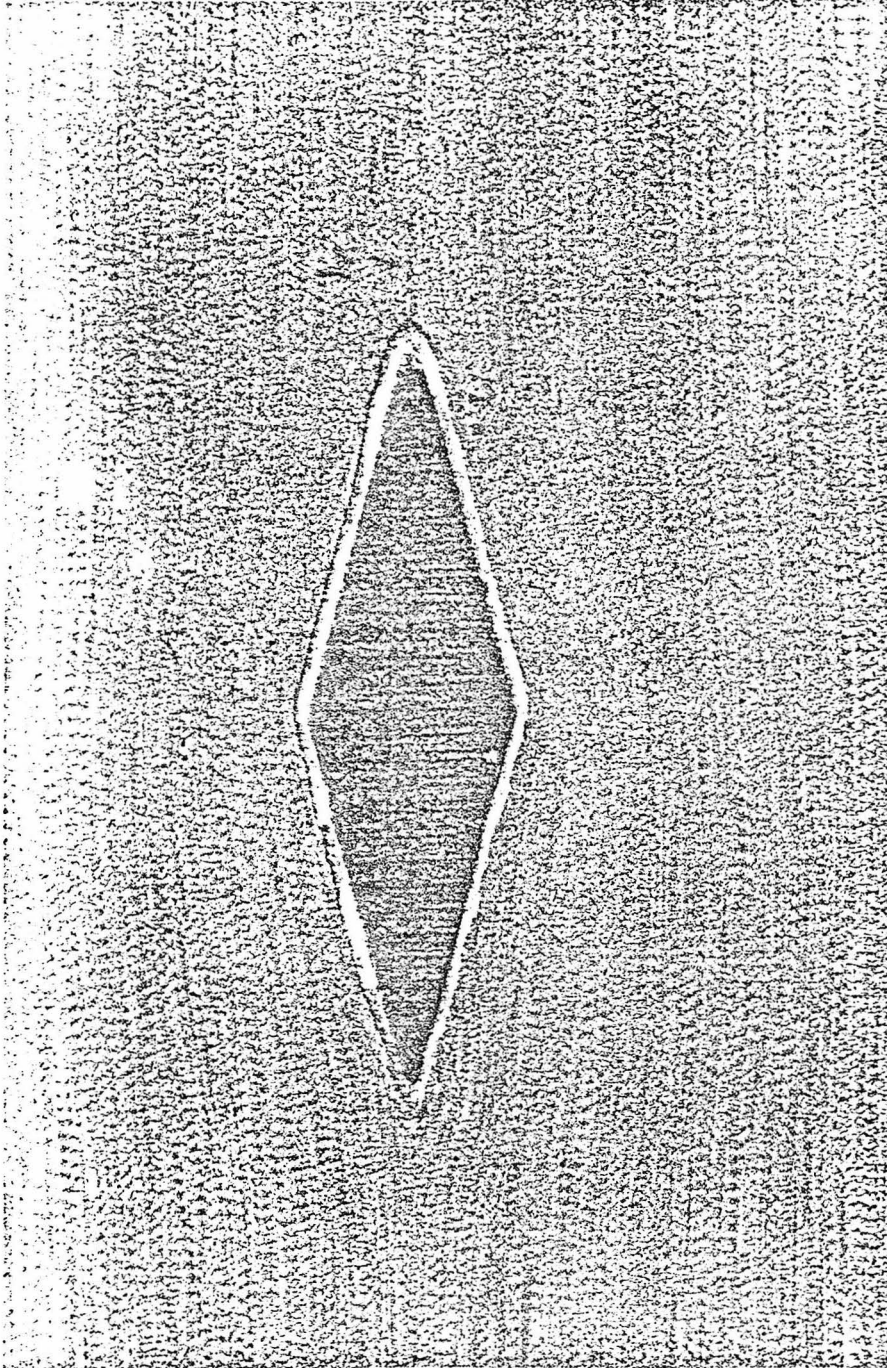
Figure 3.1.1 Flow of a fine grain sand over a double wedge.
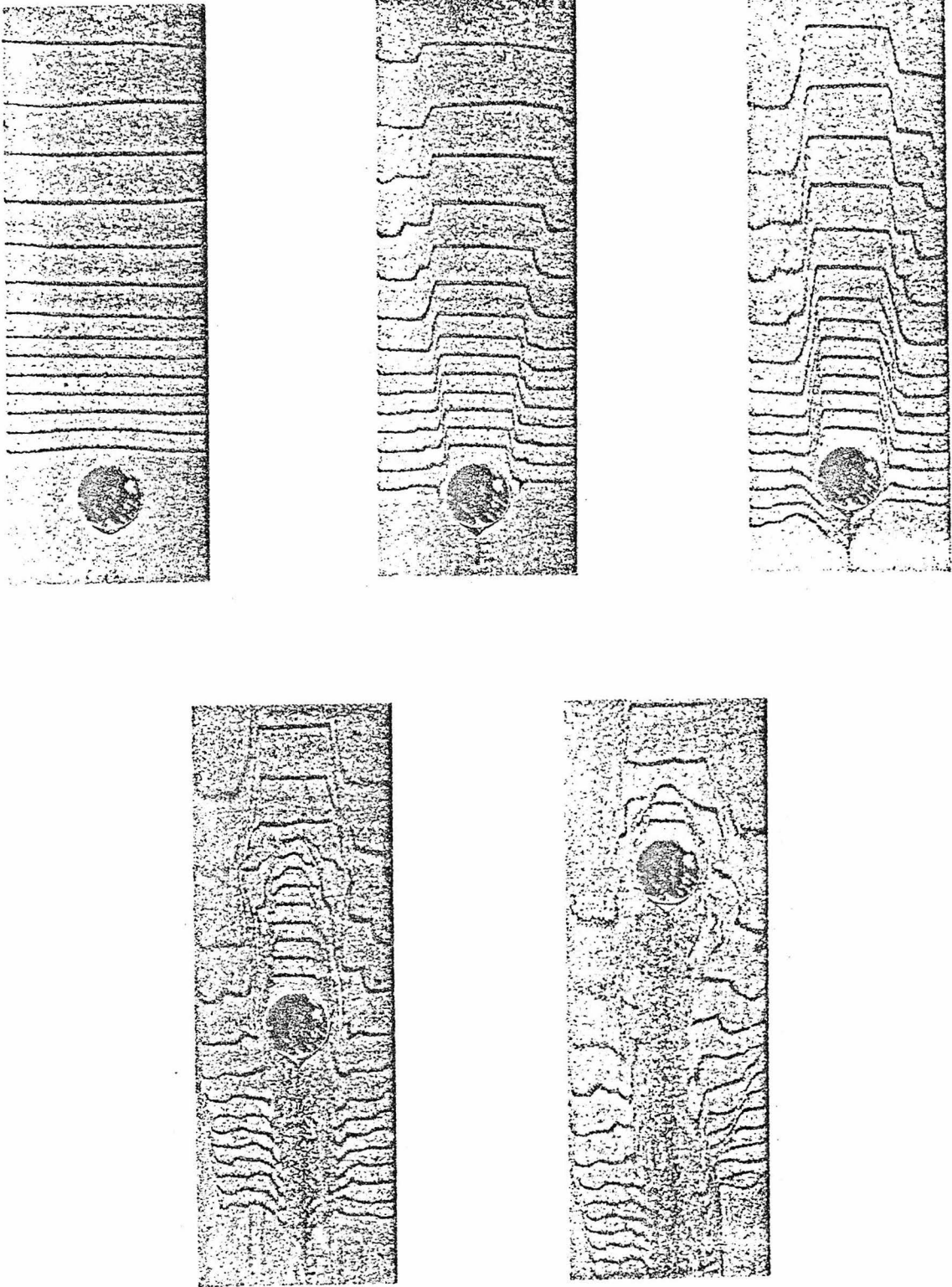
Figure 3.1.2 Initiation of flow over a cylinder.
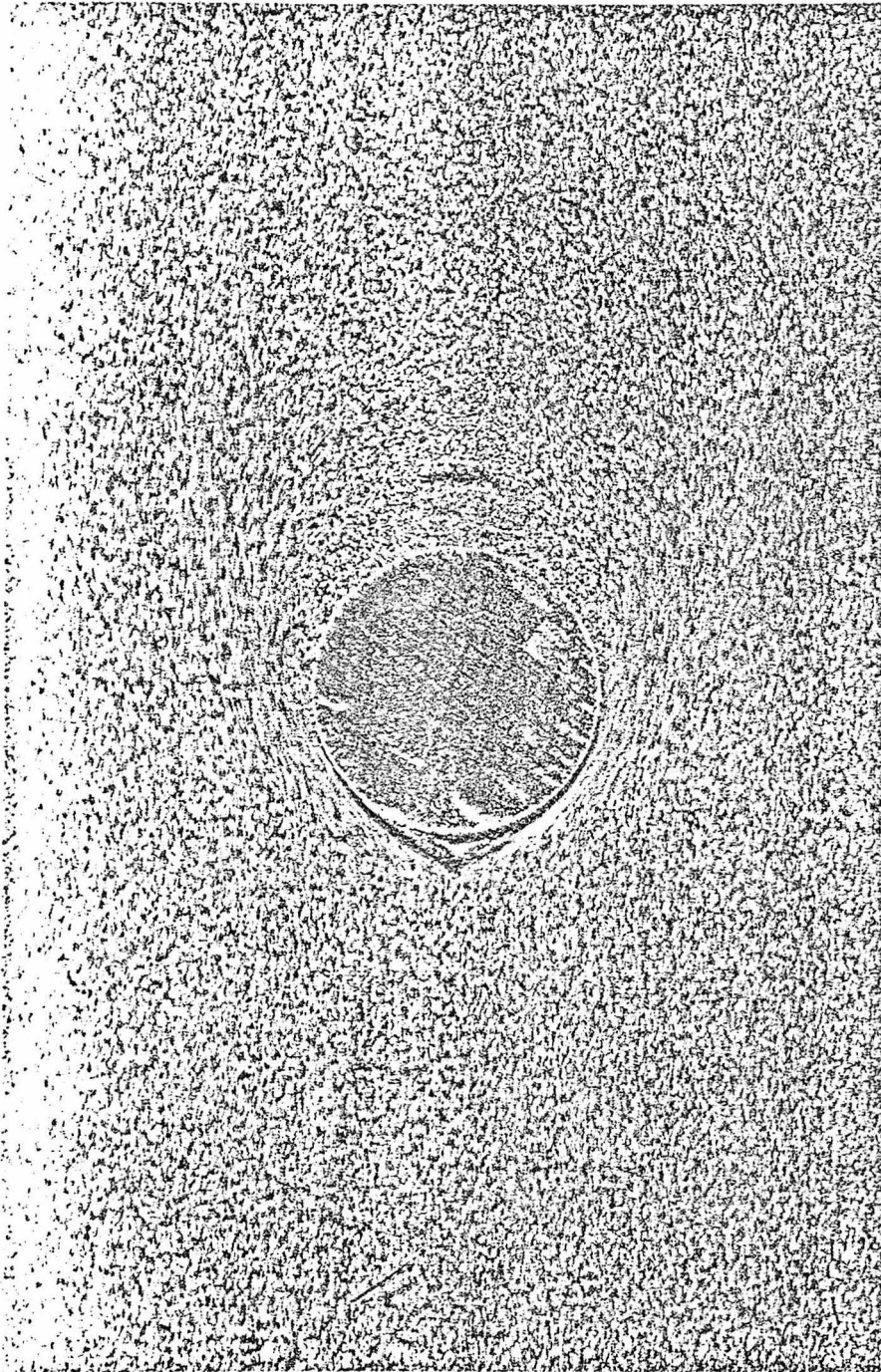
Figure 3. 1. 3   Stagnant region and cavity for the flow of
a fine grain sand over a cylinder.
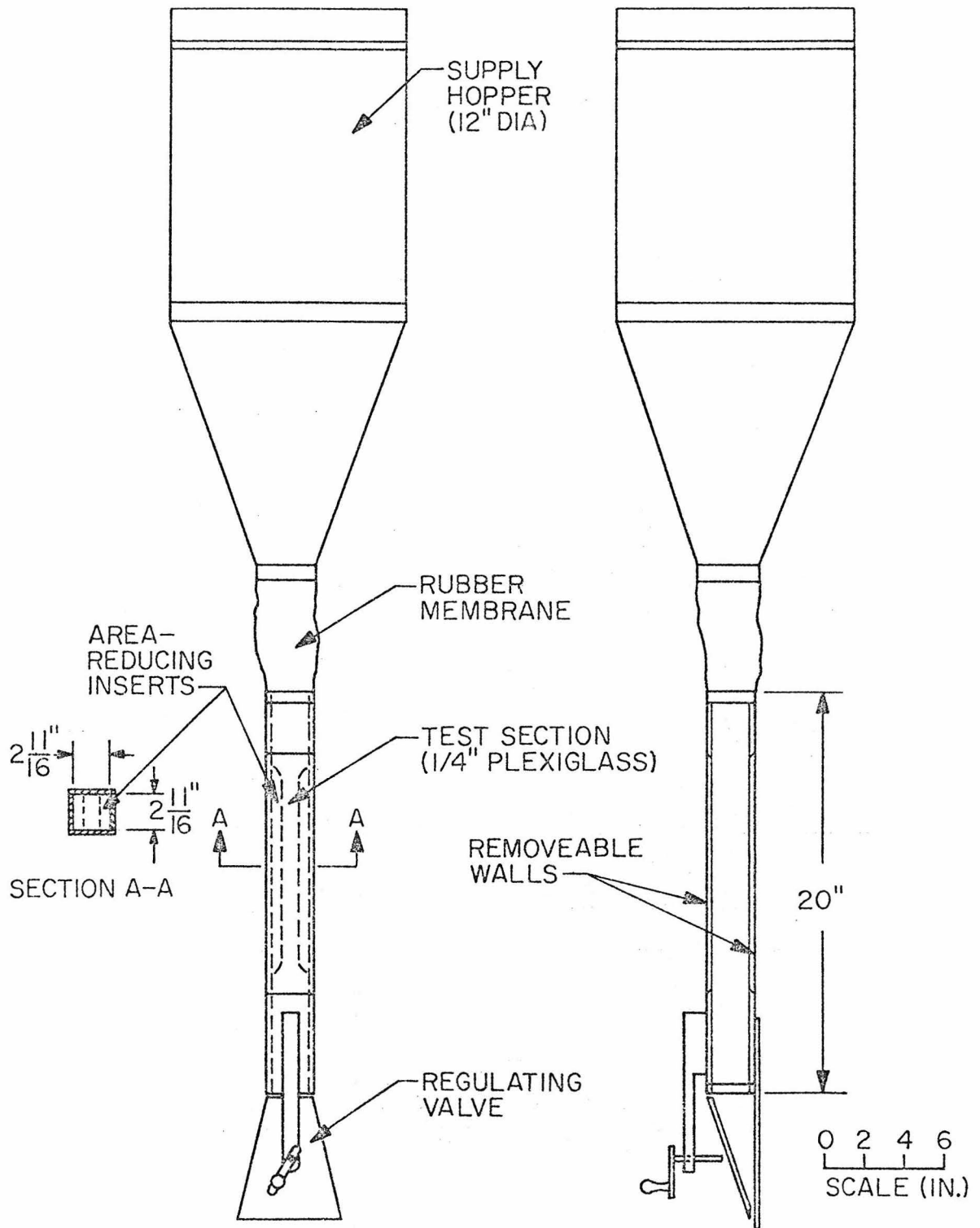
Figure 3.3.1 Schematic diagram of the flow apparatus.
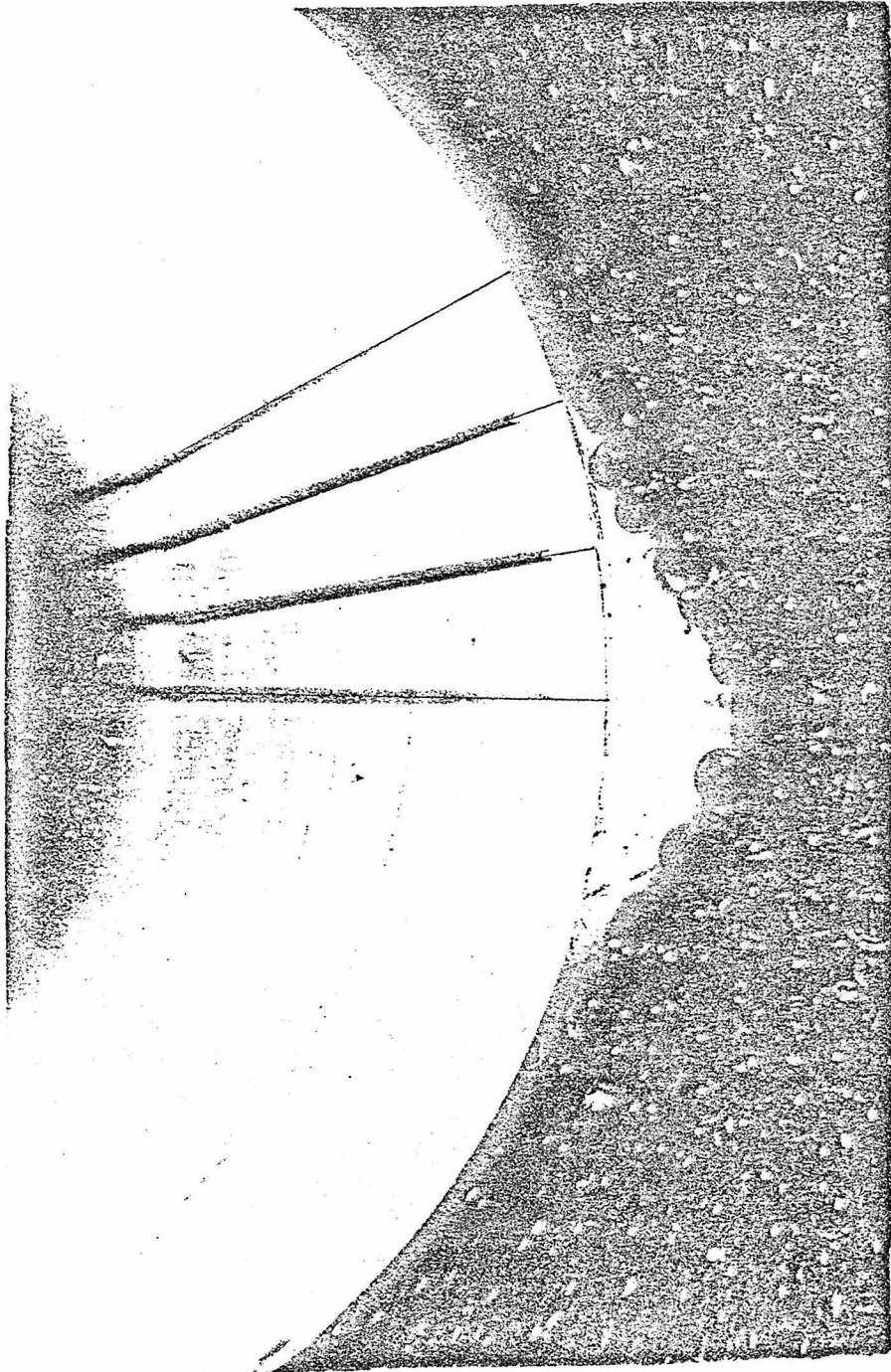
Figure 3.4.1a Cavity below $1\frac{1}{4}$ diameter cylinder in flow of P-0280 glass beads.
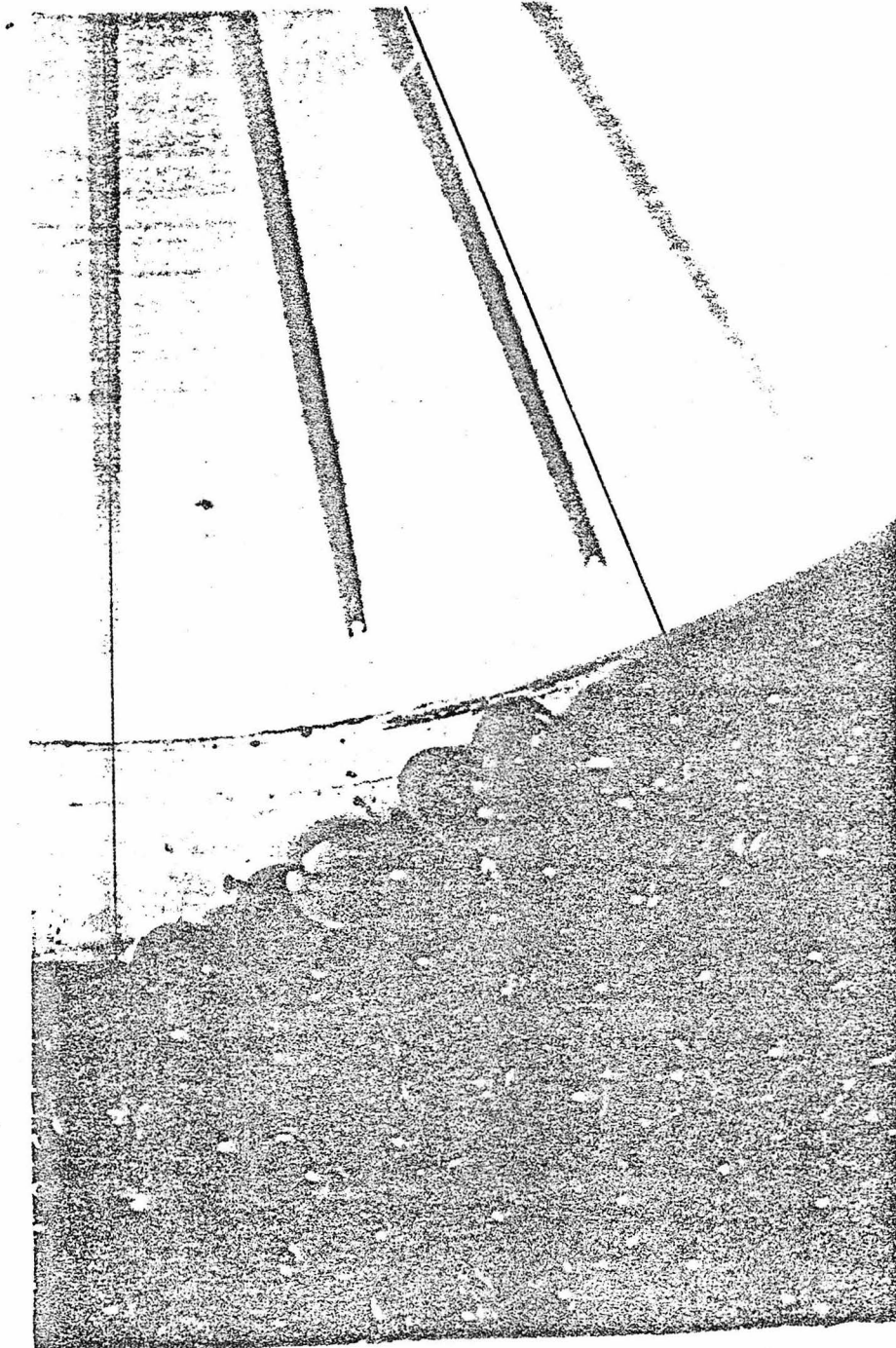
Figure 3. 4. 1b High magnification of separation point.
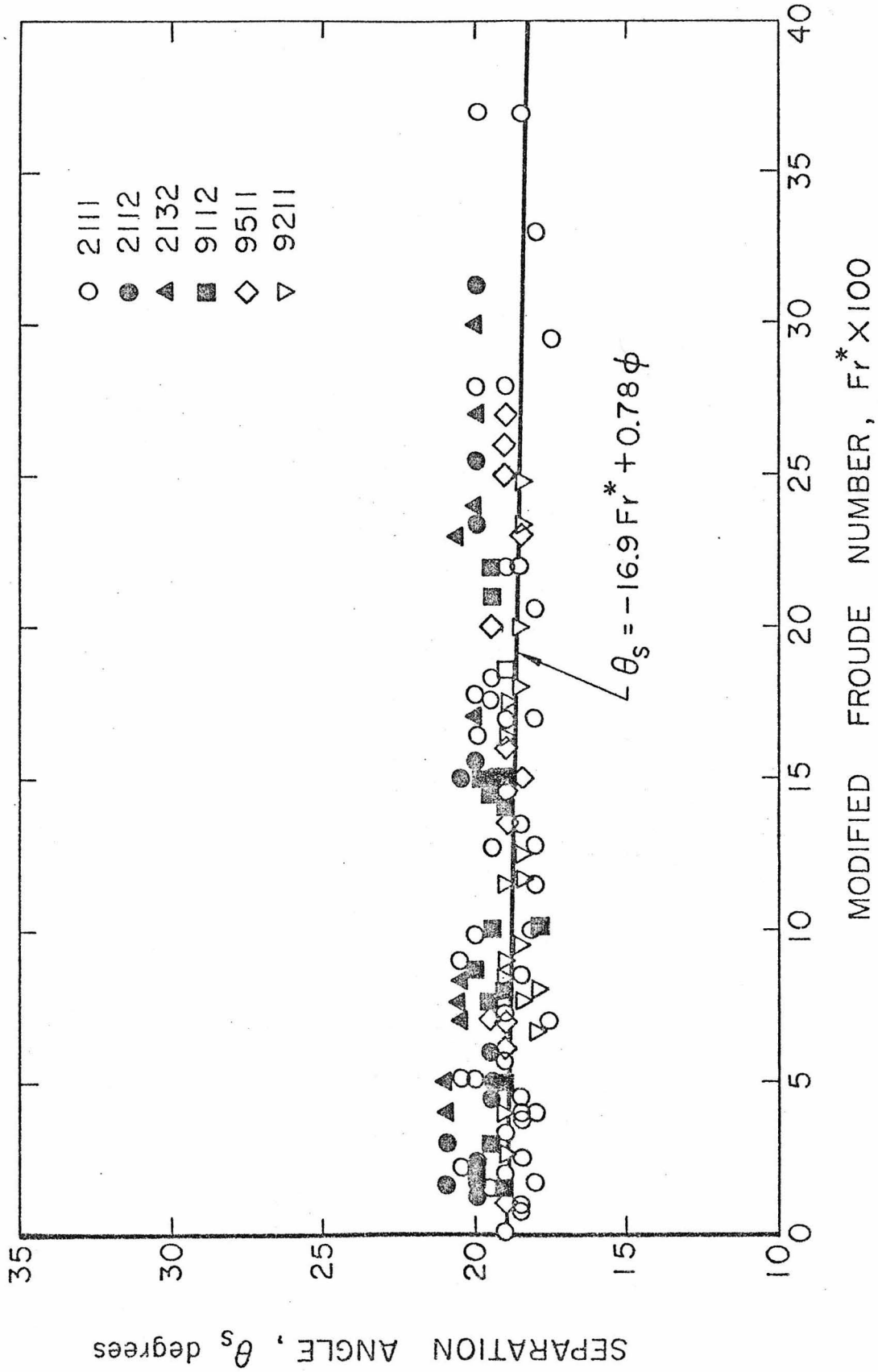
Figure 3.7.1 Separation angle versus modified Froude number for P-0280 glass beads.
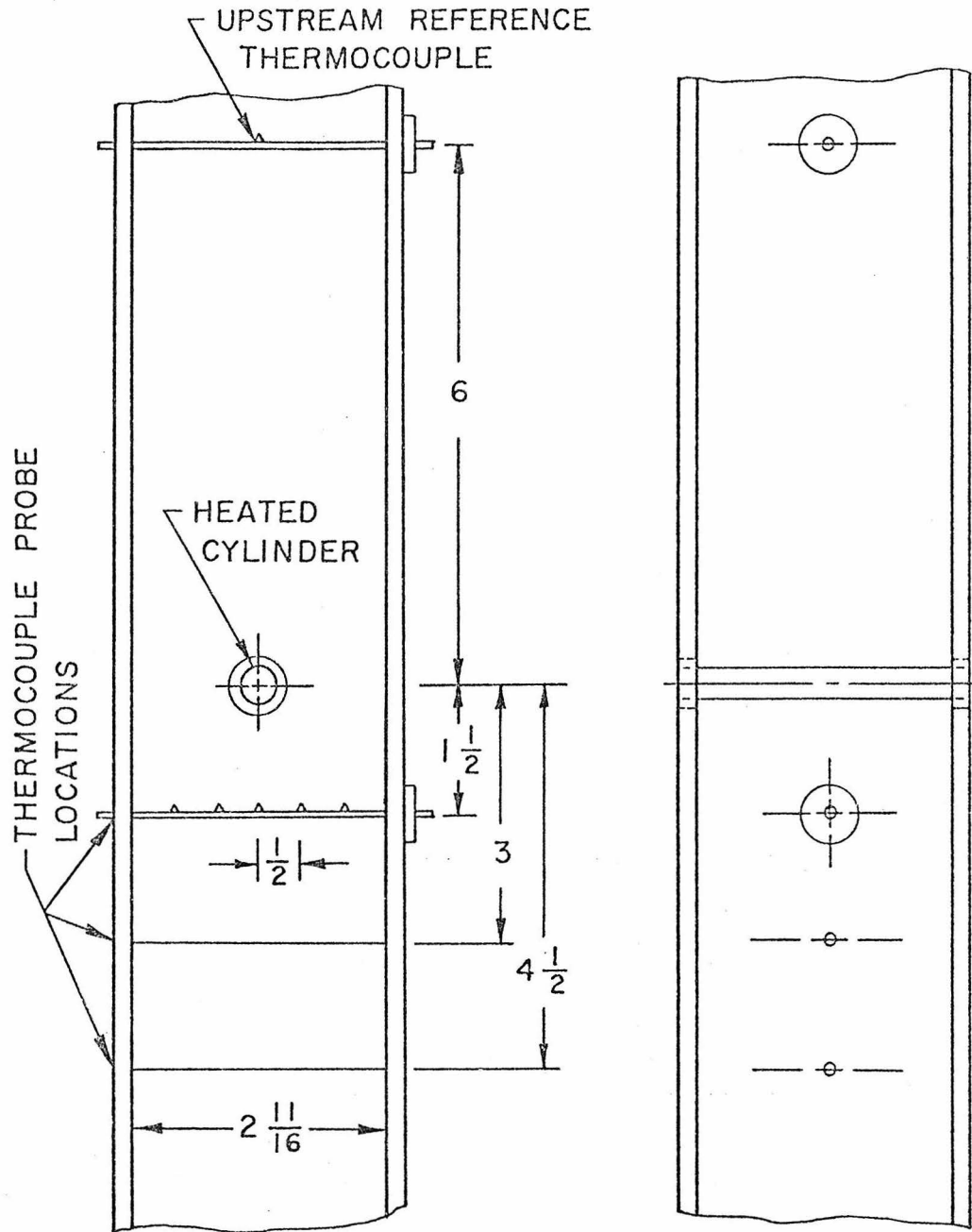
Figure 4.3.1 Schematic diagram of test
section for wake experiments.
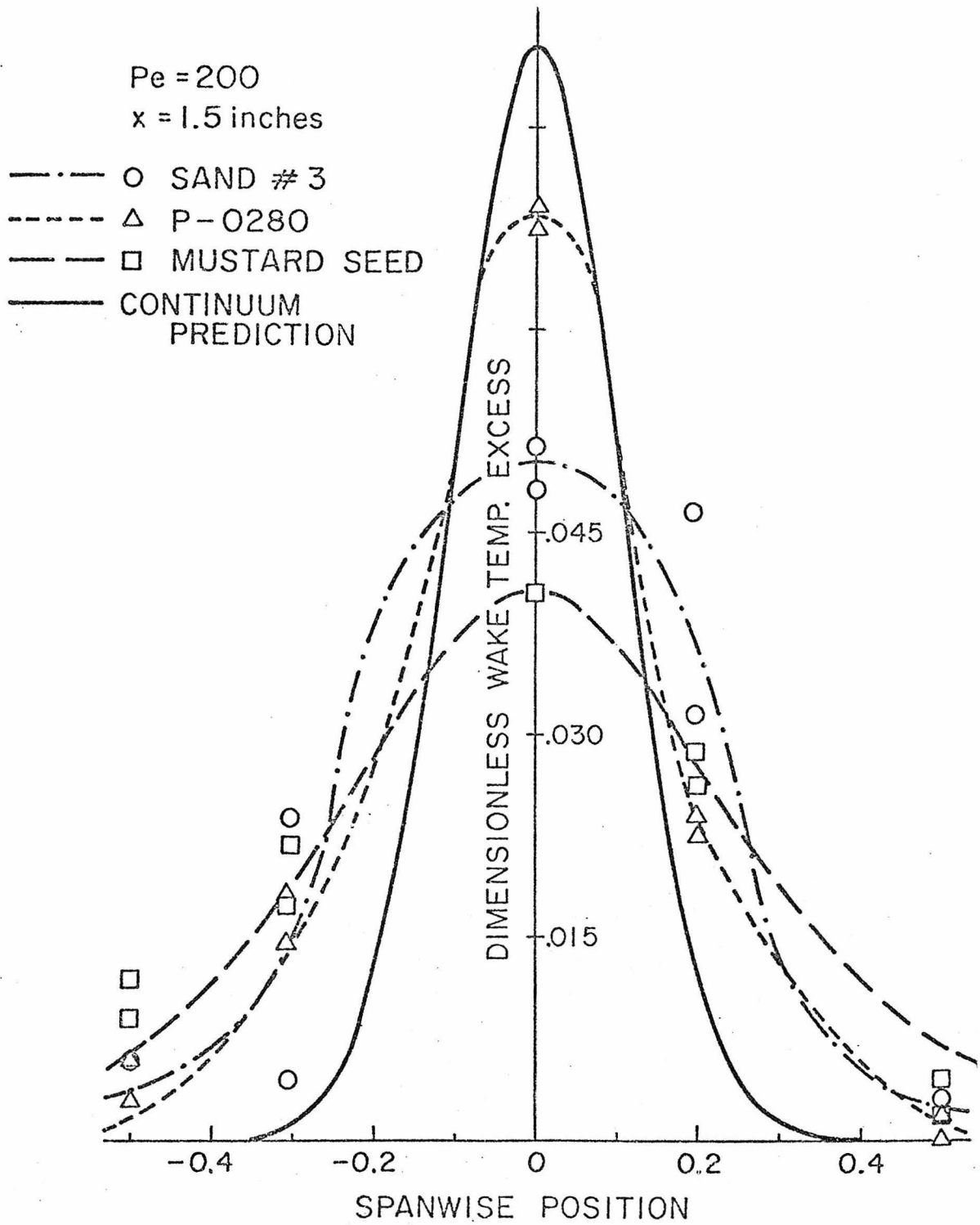
Figure 4.3.2 Dimensionless wake temperature excess versus span-wise location in inches for Pe = 200 and x = 1.5 inches.
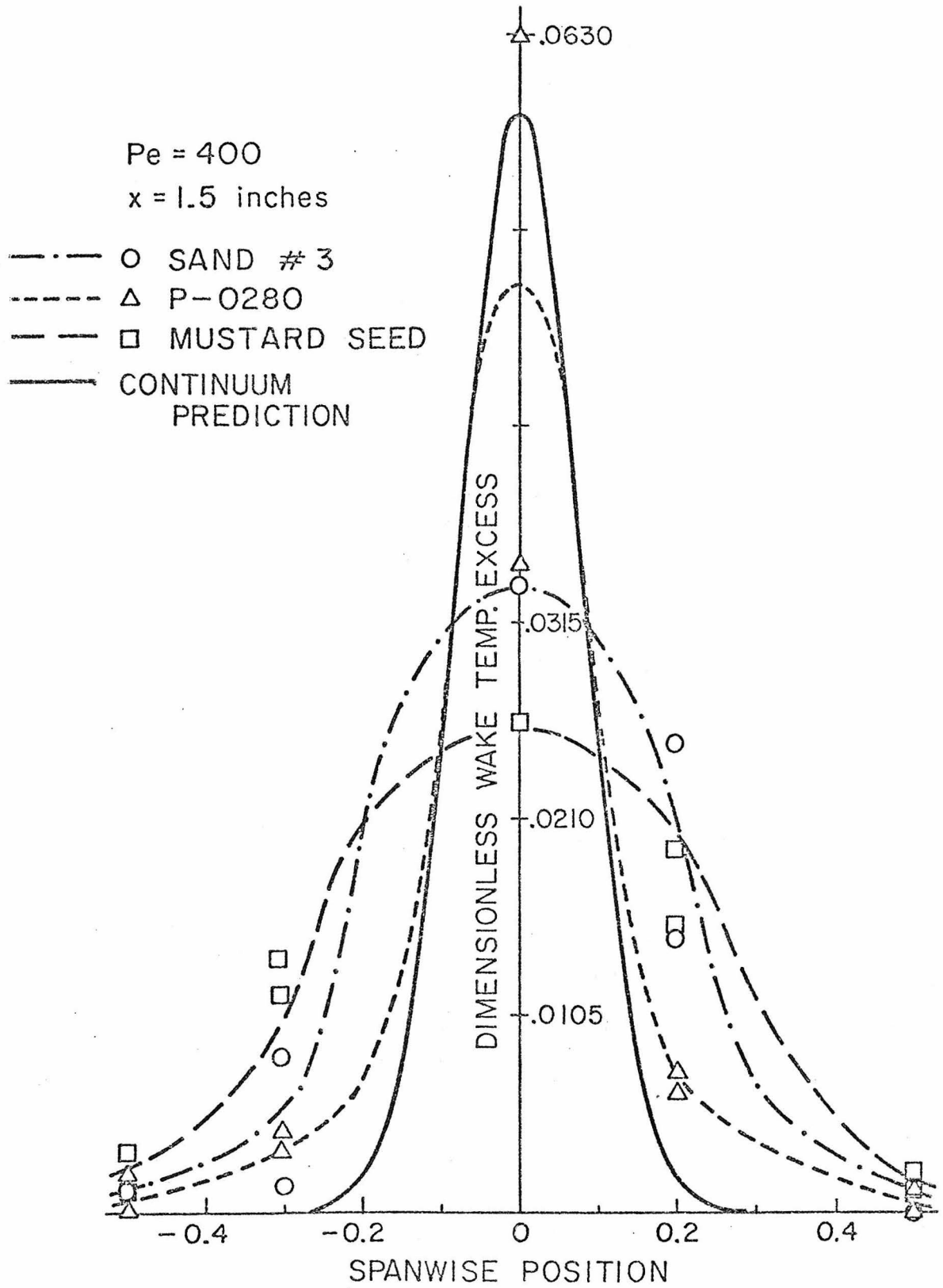
Figure 4.3.3 Dimensionless wake temperature excess versus span-wise location in inches for Pe = 400 and x = 1.5 inches.
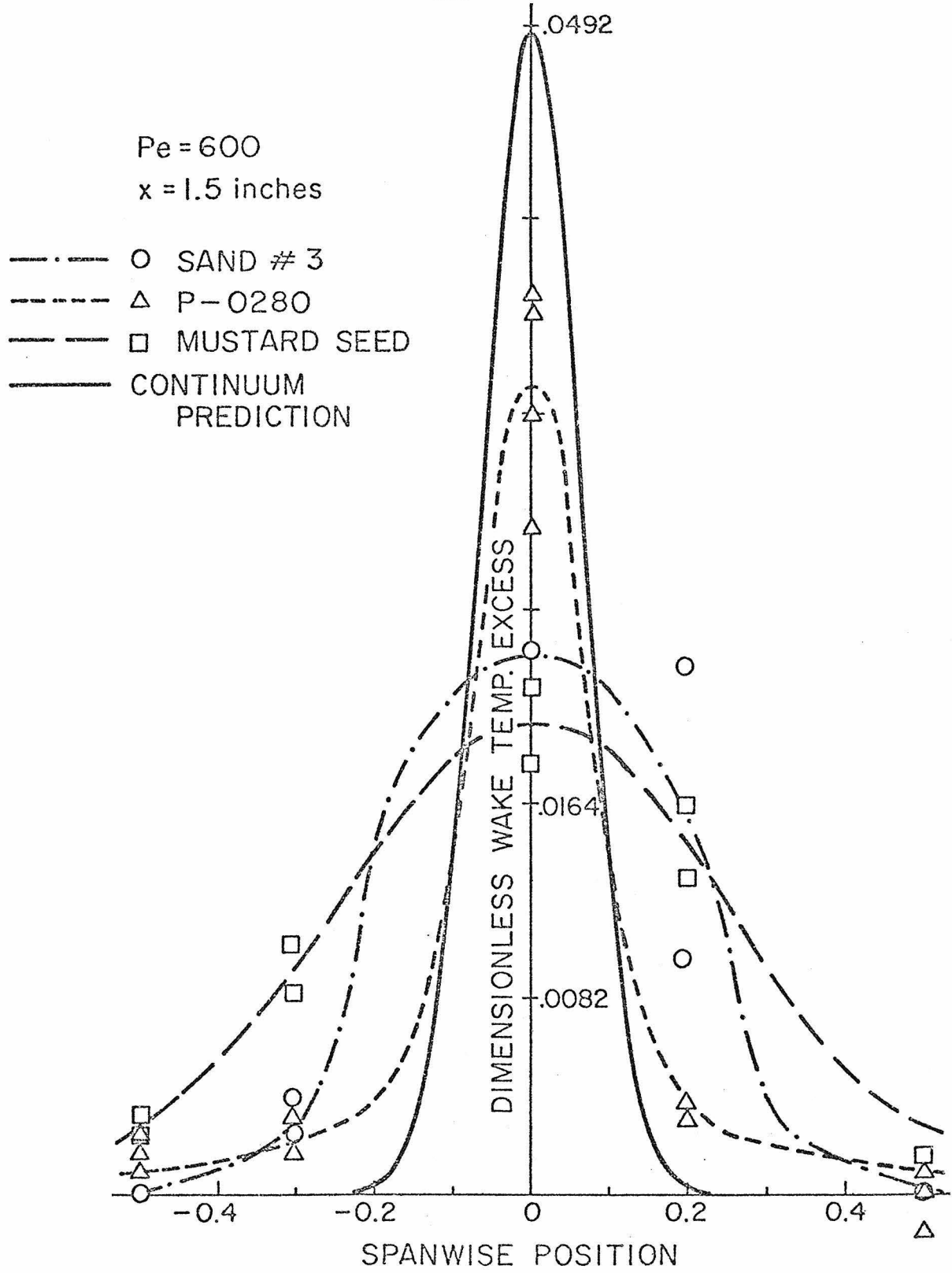
Figure 4.3.4 Dimensionless wake temperature excess versus span-
wise location in inches for Pe = 600 and x = 1.5 inches.
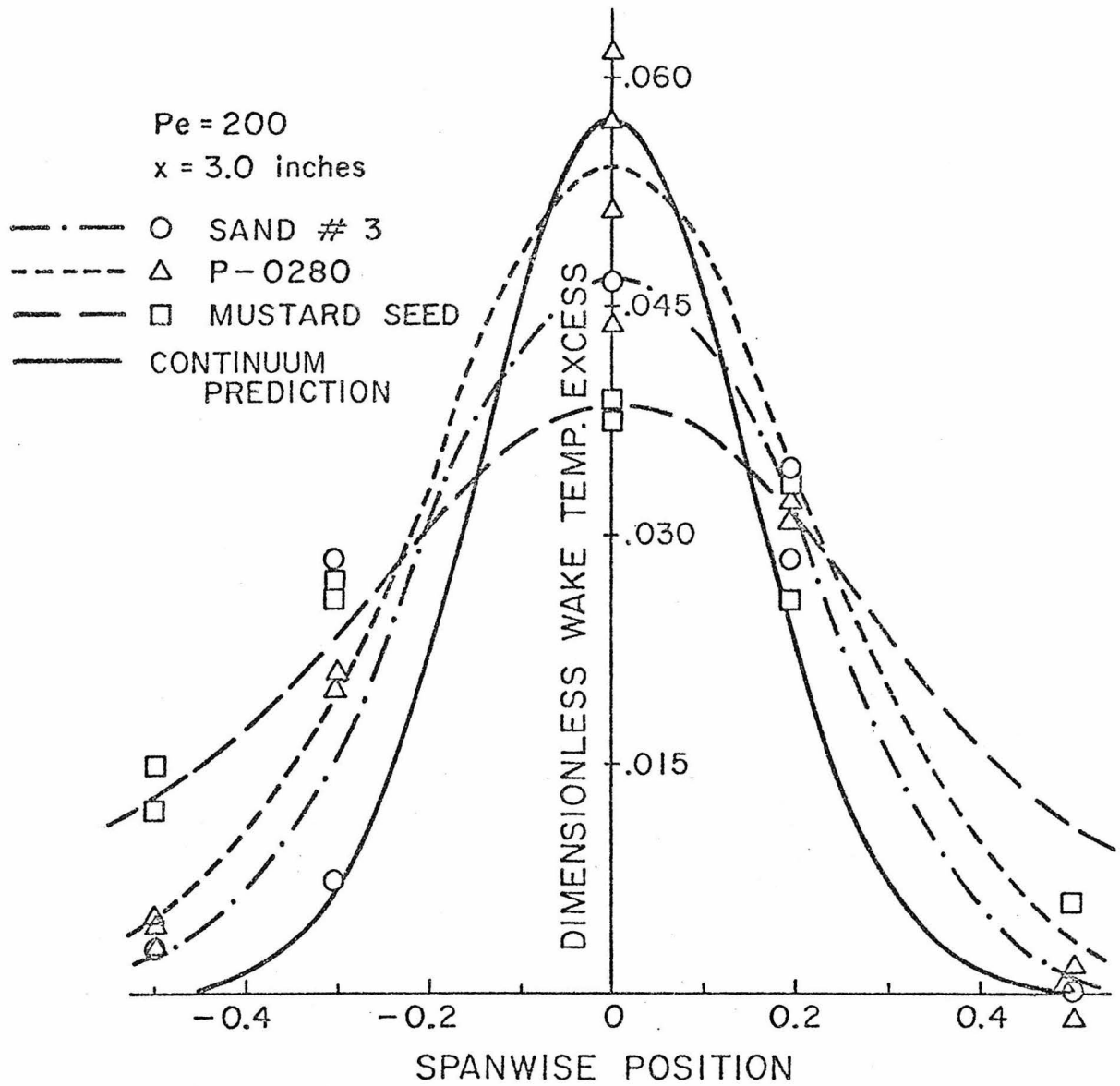
Figure 4.3.5 Dimensionless wake temperature excess versus span-
wise location in inches for Pe = 200 and x = 3.0 inches.
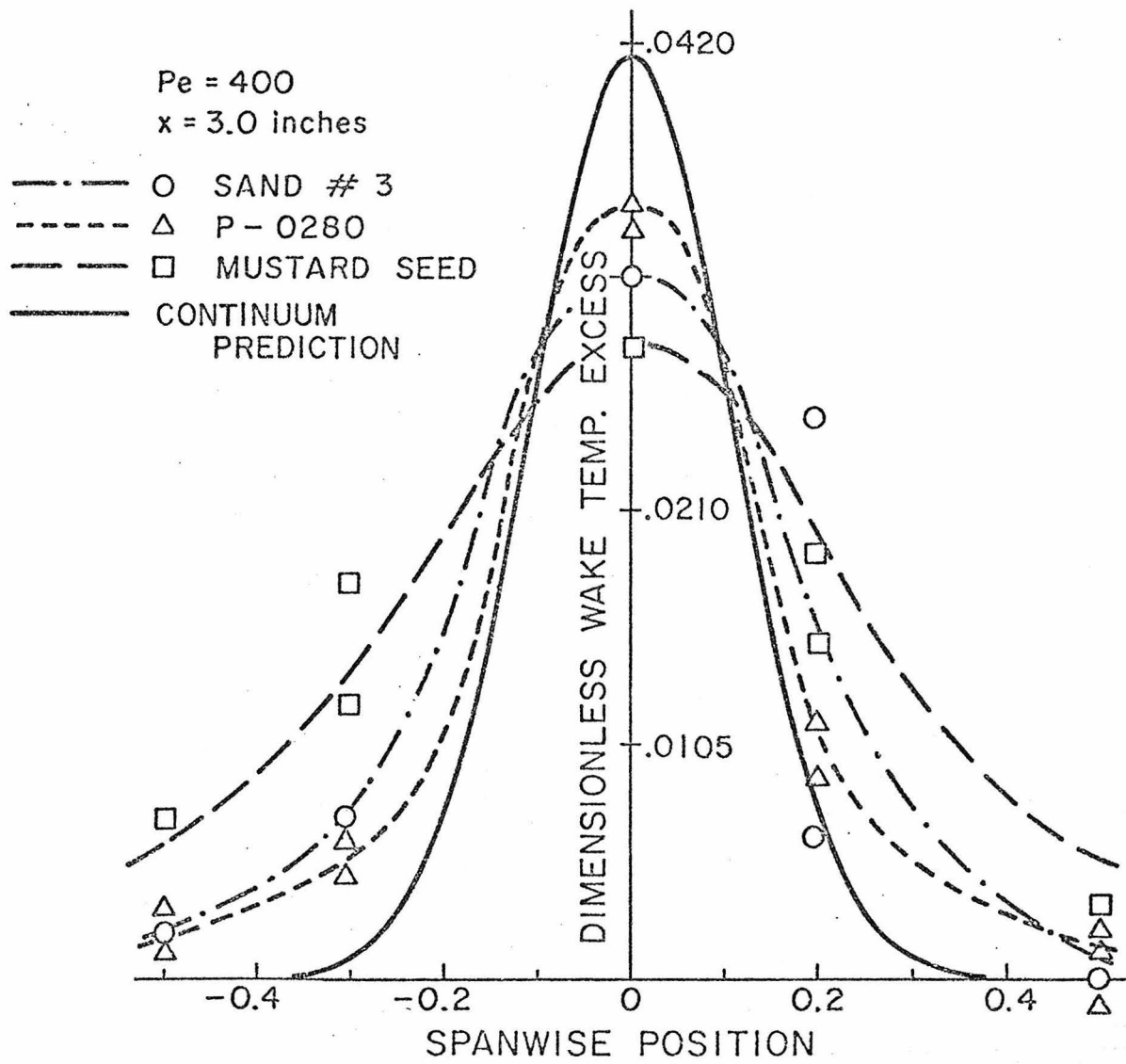
Figure 4.3.6 Dimensionless wake temperature excess versus span-
wise location in inches for Pe = 400 and x = 3.0 inches.
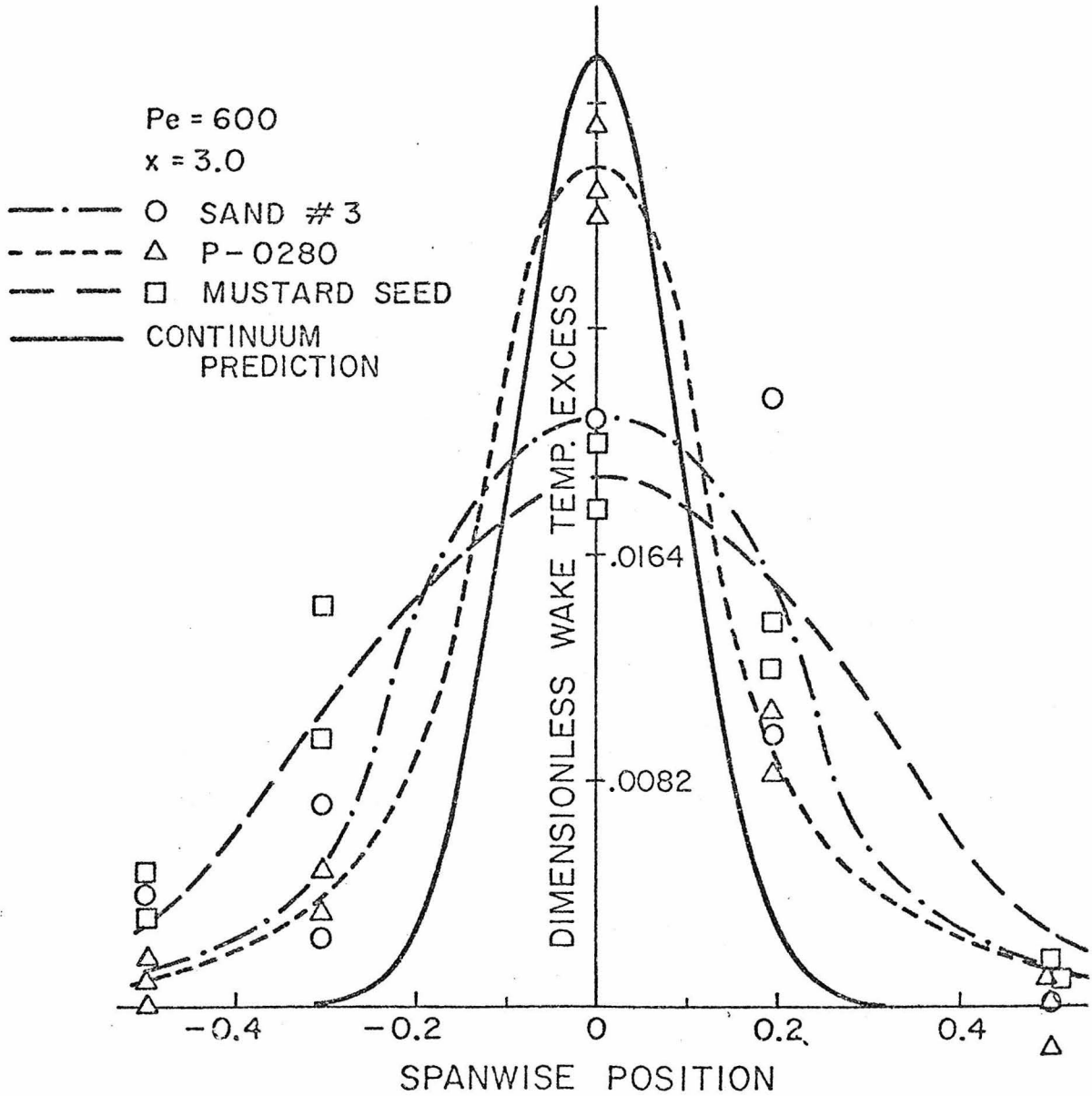
Figure 4.3.7 Dimensionless wake temperature excess versus span-
wise location in inches for Pe = 600 and x = 3.0 inches.
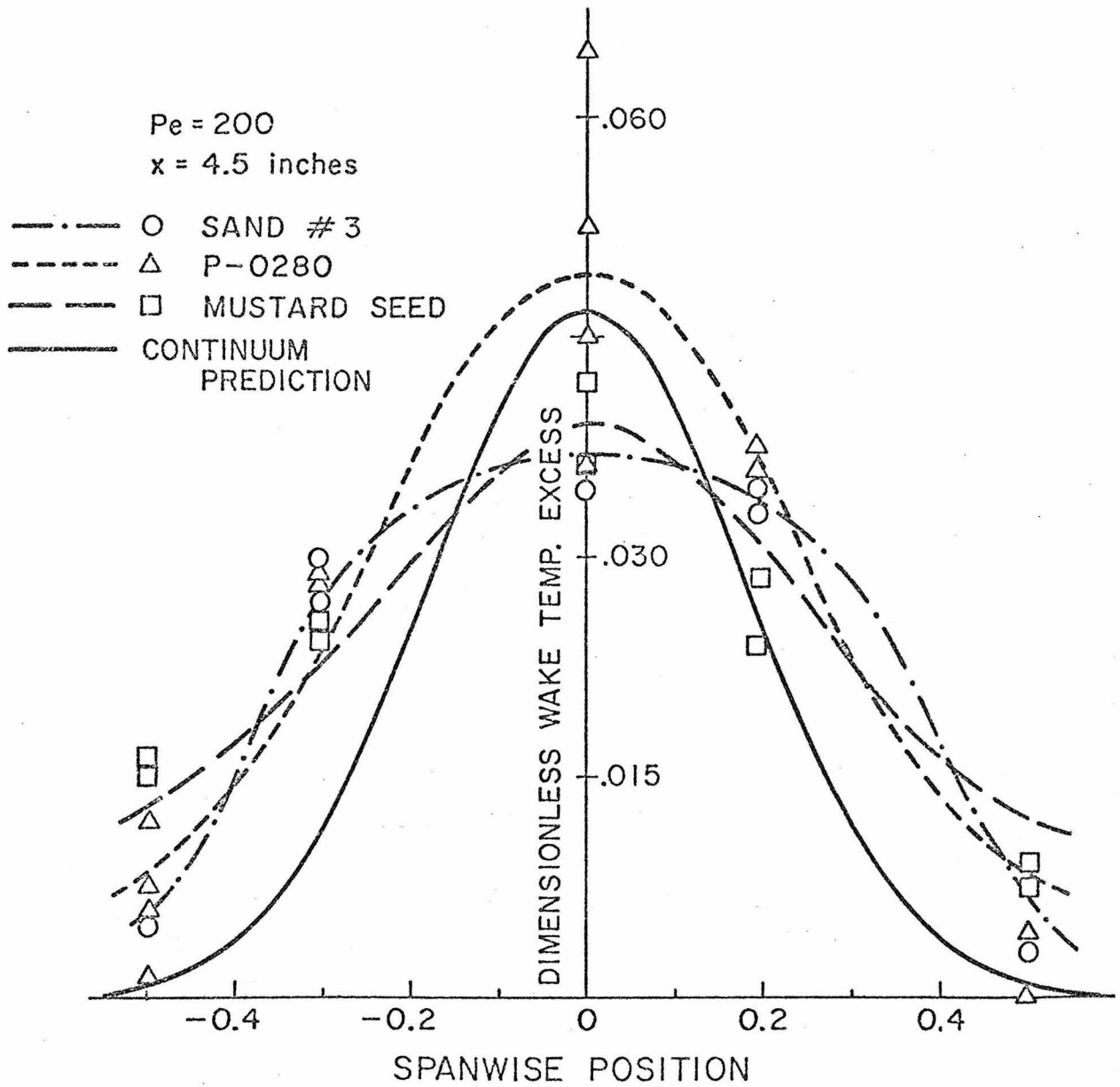
Figure 4.3.8 Dimensionless wake temperature excess versus span-wise location in inches for Pe = 200 and x = 4.5 inches.
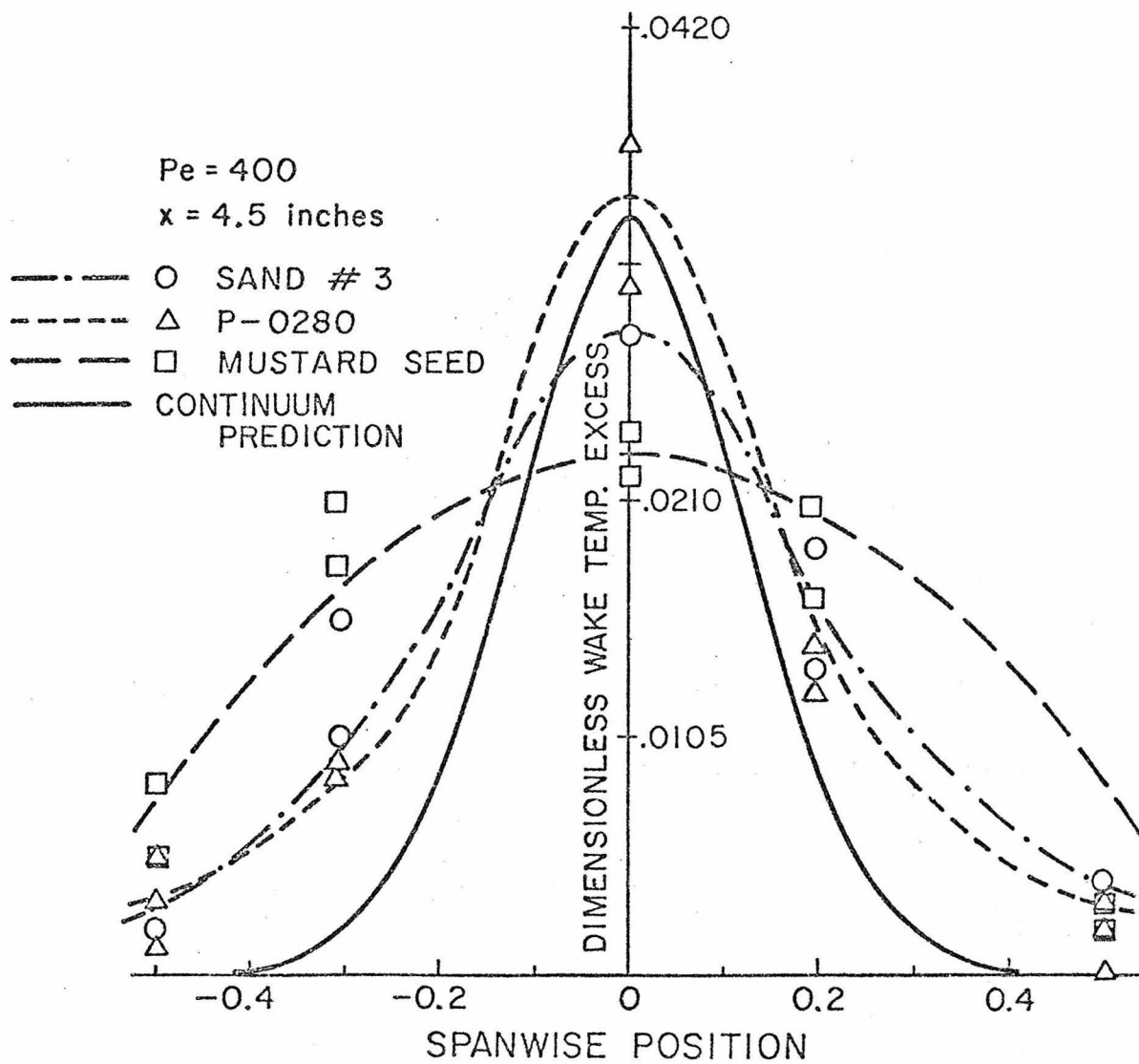
Figure 4.3.9 Dimensionless wake temperature excess versus span-
wise location in inches for Pe = 400 and x = 4.5 inches.
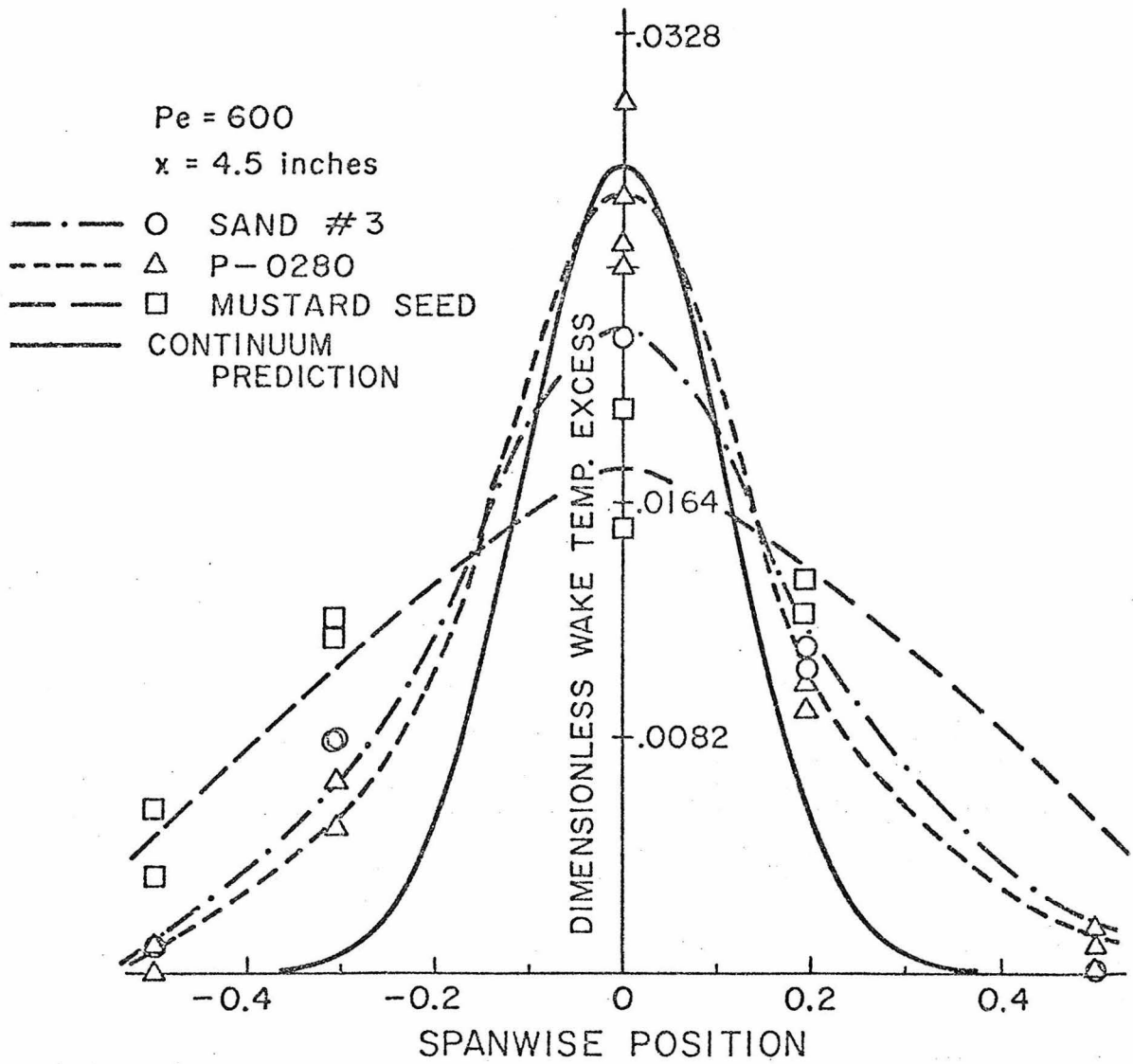
Figure 4.3.10 Dimensionless wake temperature excess versus span-
wise location in inches for Pe = 600 and x = 4.5 inches.
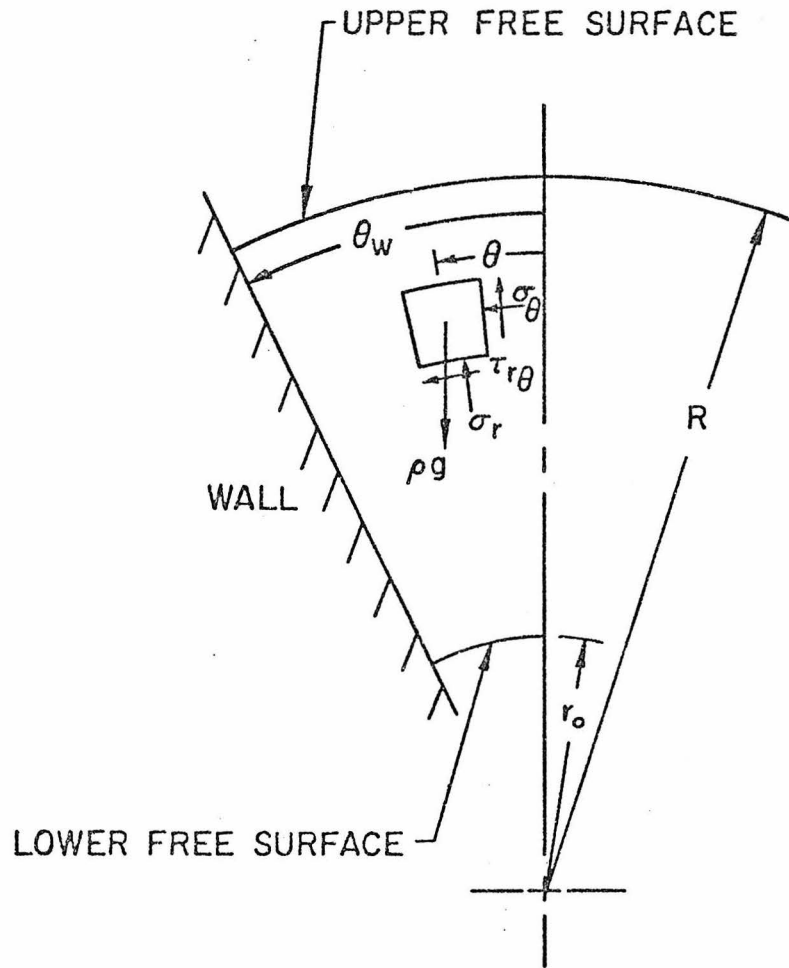
Figure A-1   Plane, symmetric converging channel.
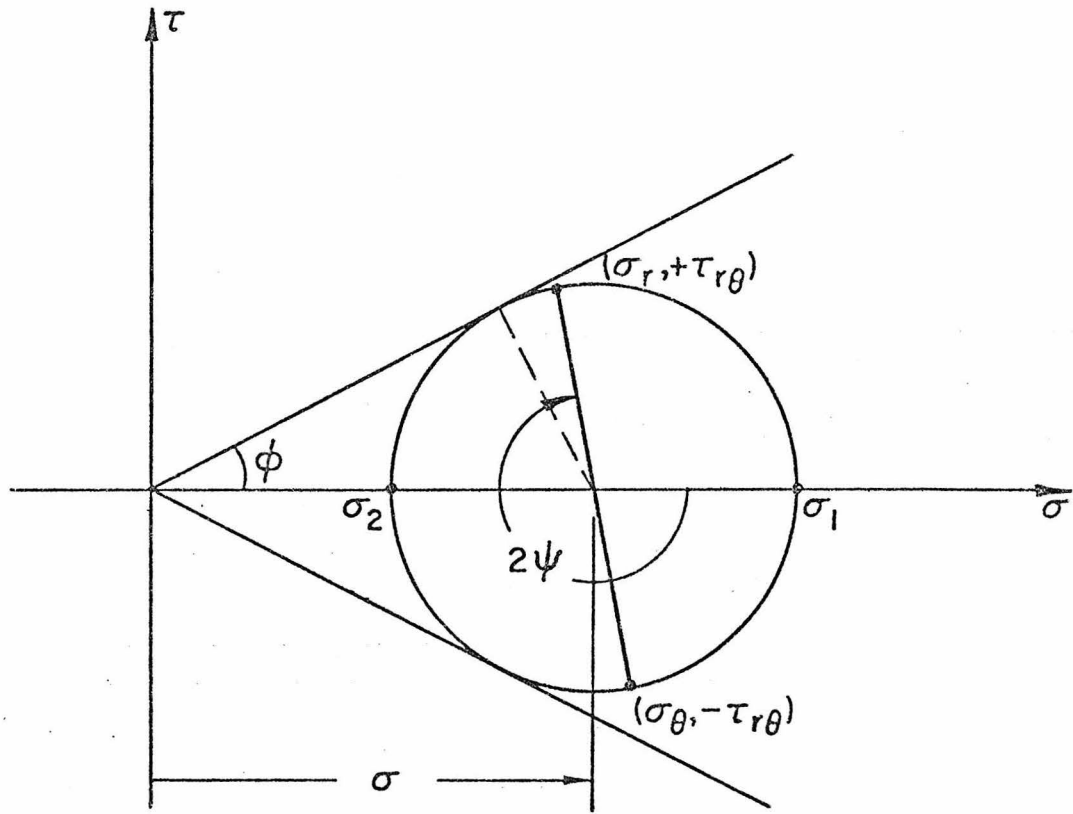
Figure A-2   Mohr diagram and Mohr envelope
with effective friction angle, φ.
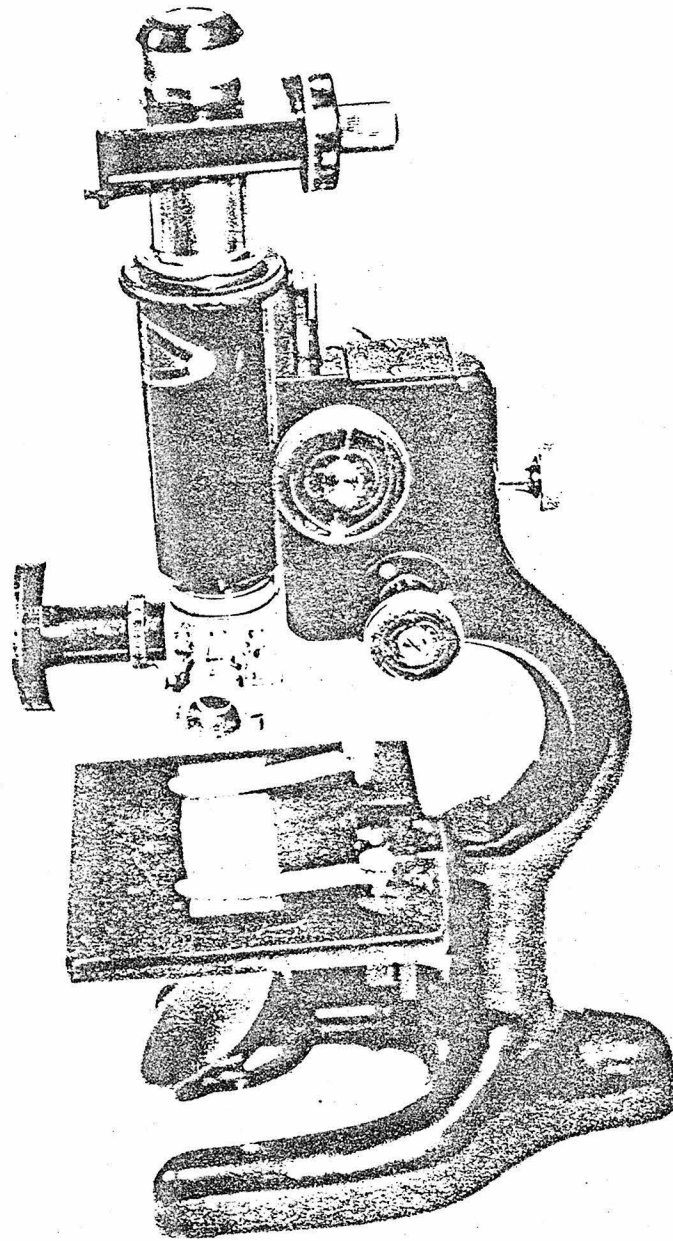
Figure B-1 Microscope used in particle size determination.
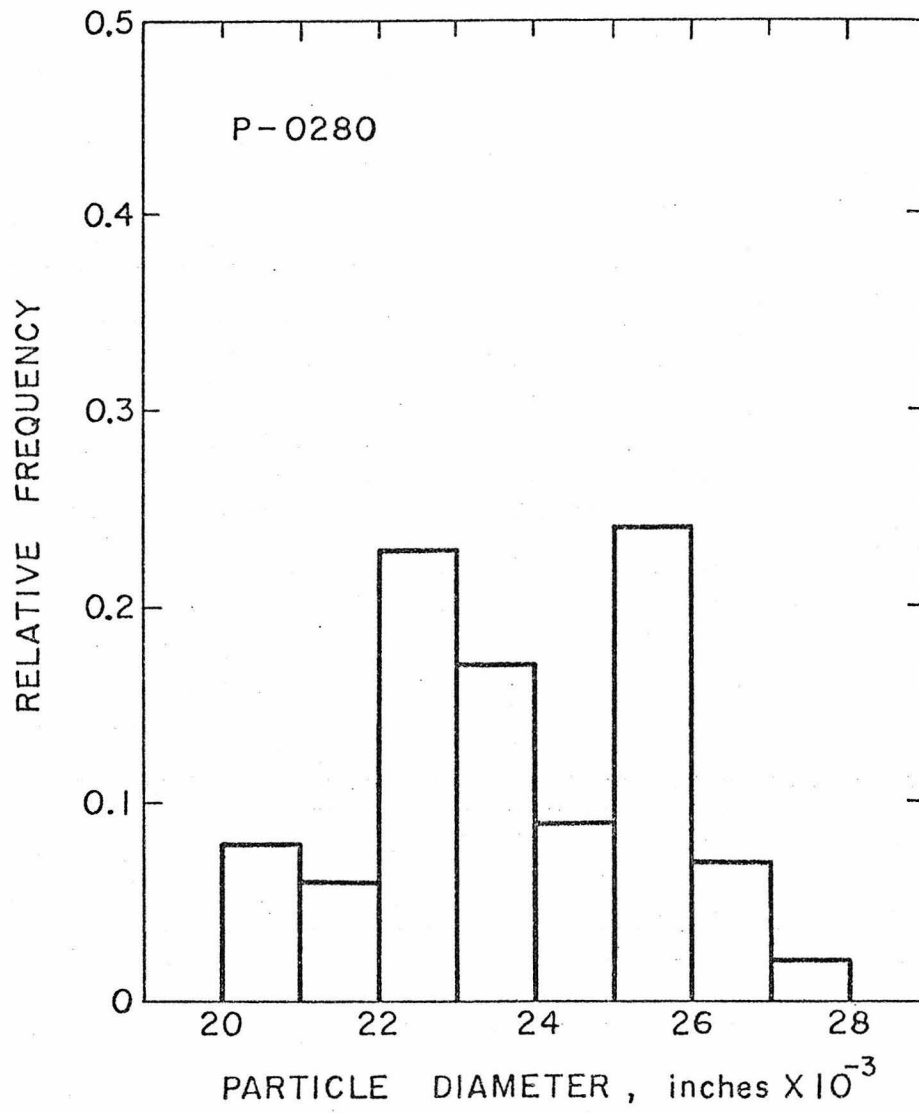
Figure B-2 Typical particle size distribution.
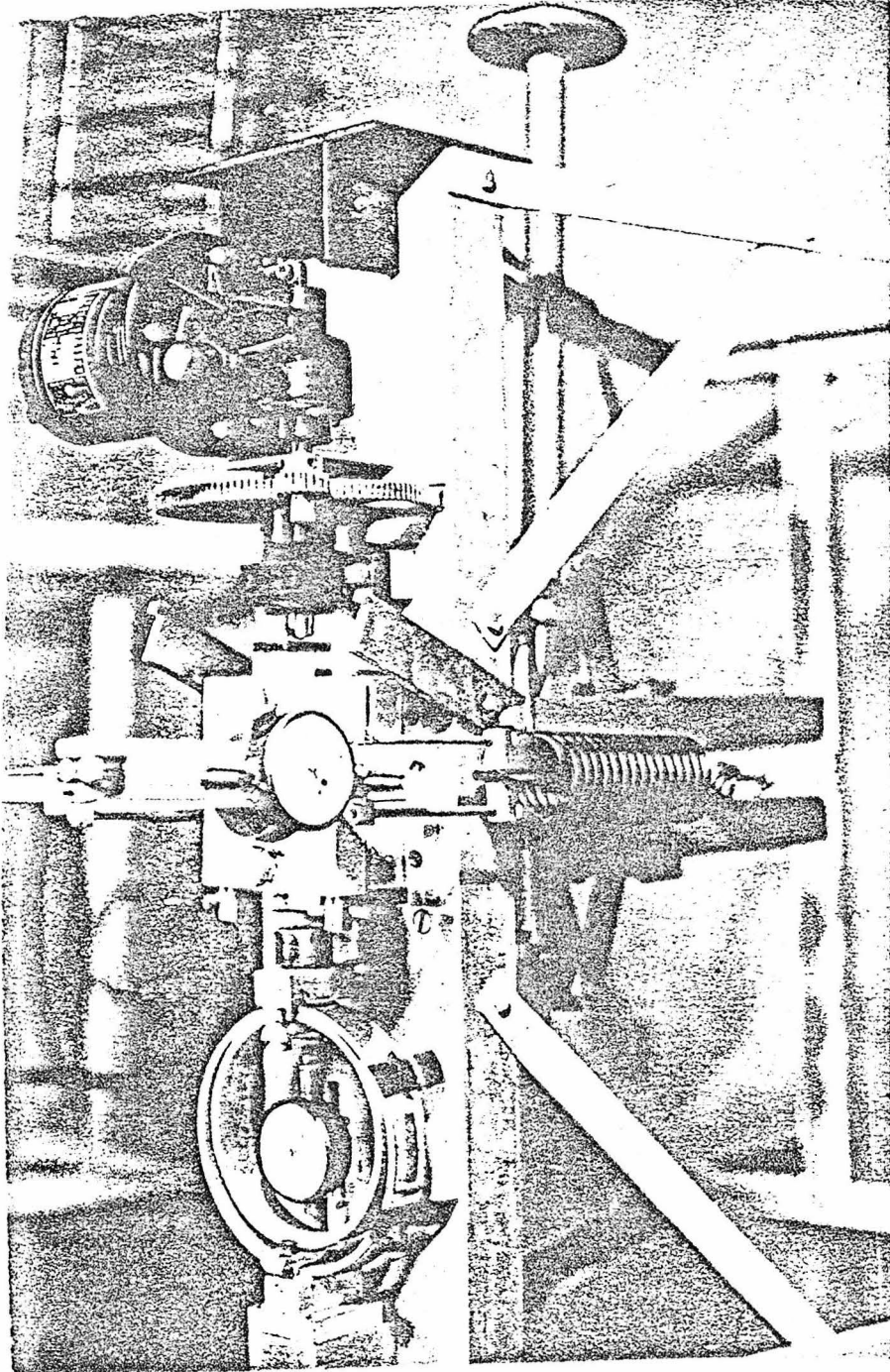
Figure B-3 Direct shear test apparatus.
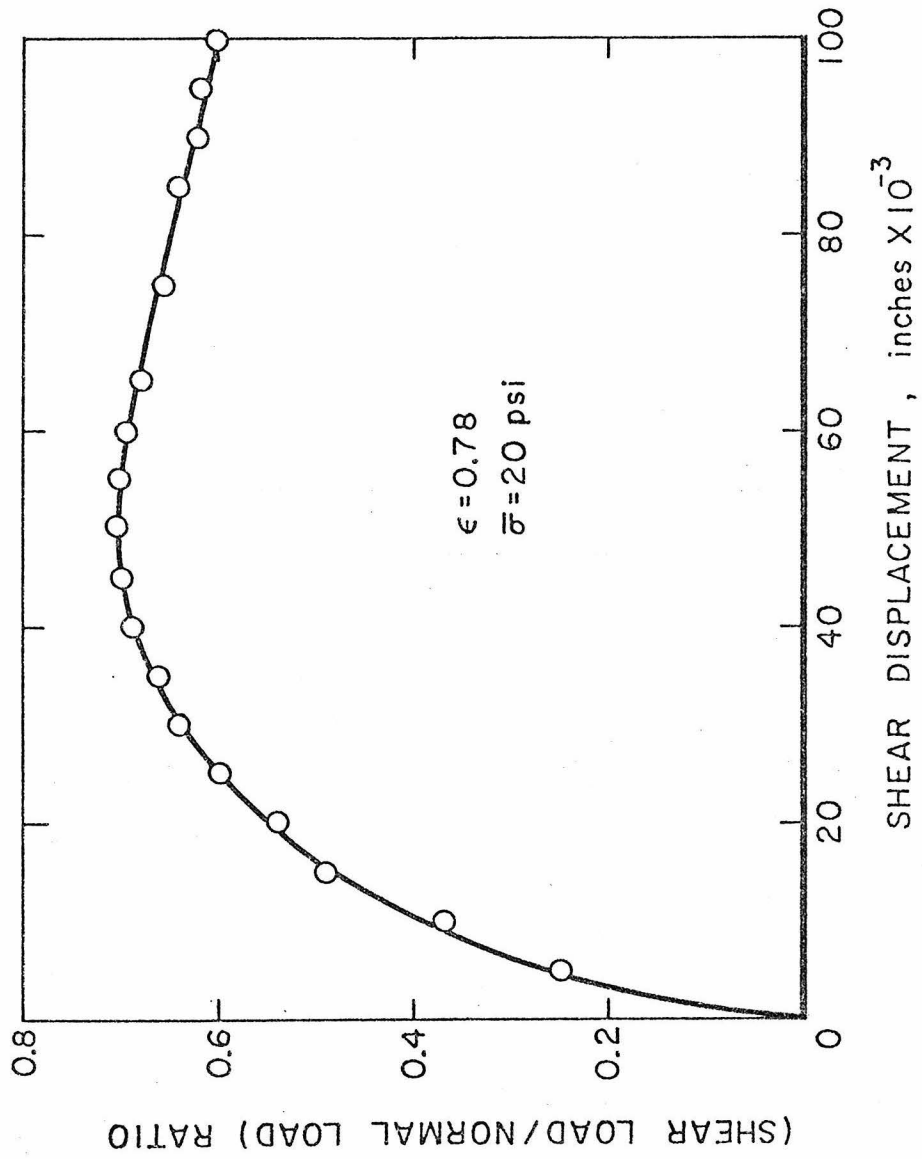
Figure B-4 Typical plot of shear load — normal load
ratio versus shear displacement.
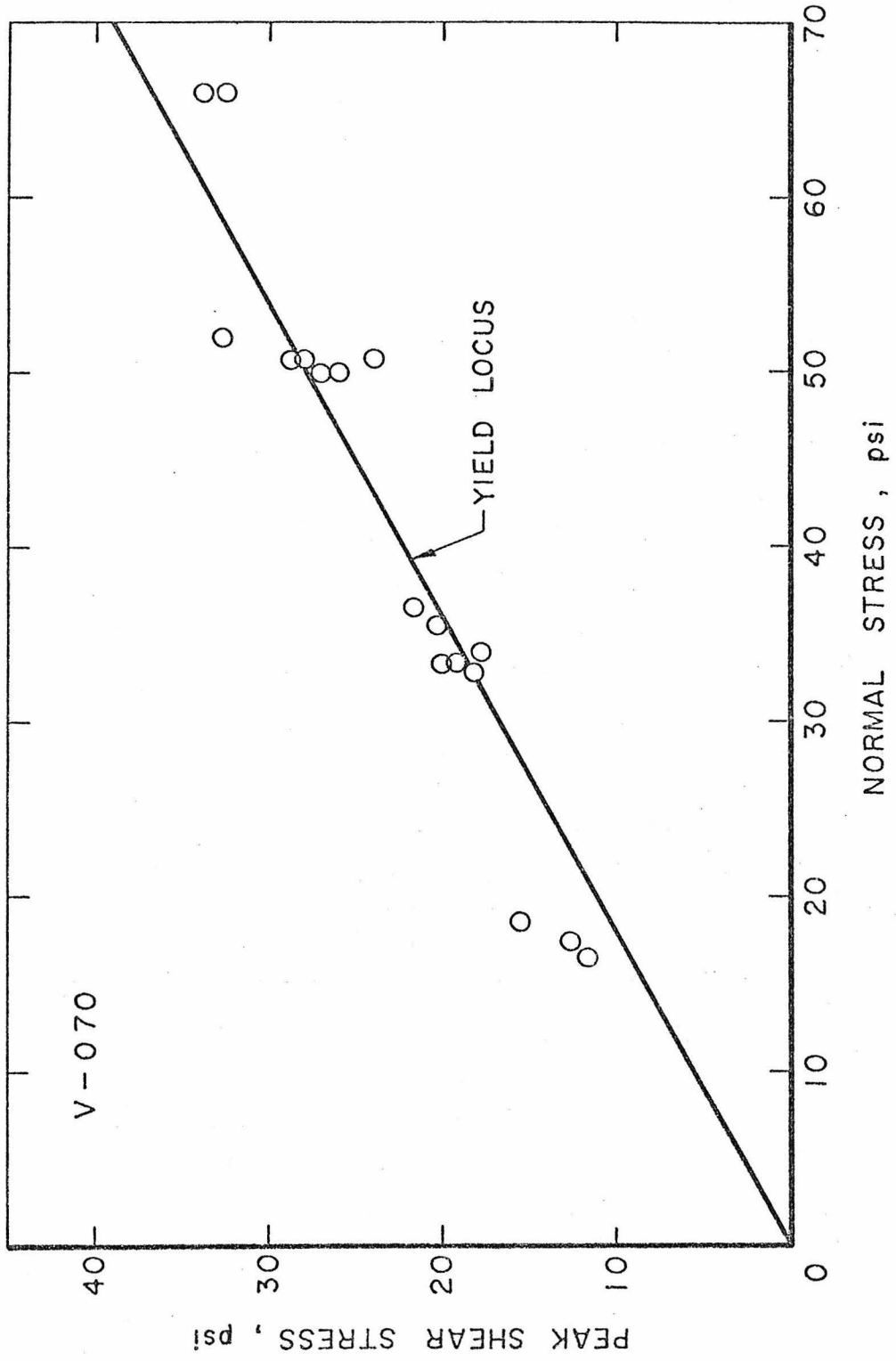
Figure B-5 Typical plot of peak shear load versus normal
load for internal friction angle experiment.
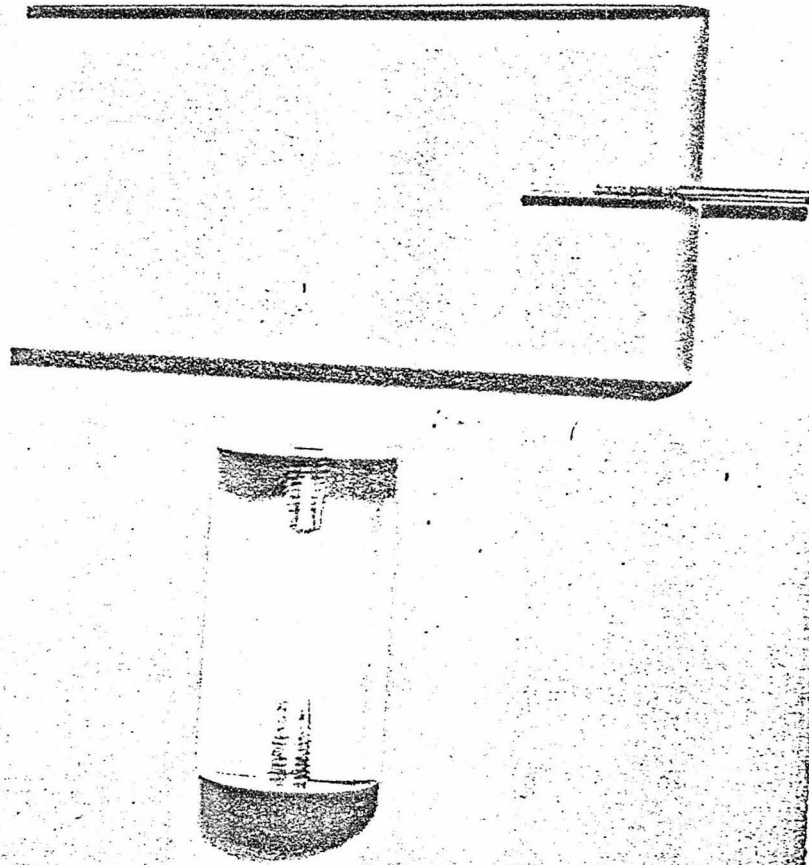
Figure B-6 Lucite test pad and 1.0'' diameter cylinder.
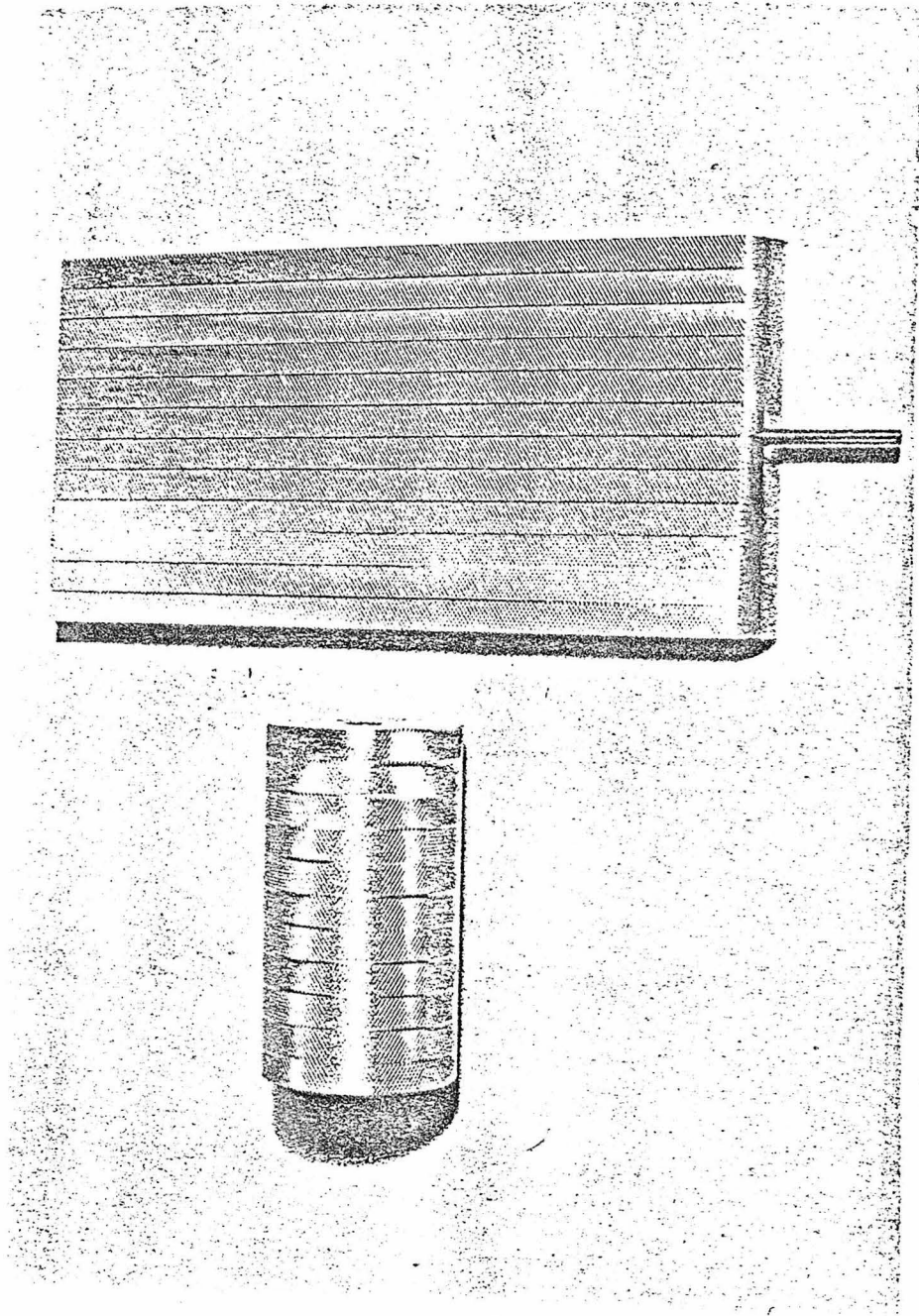
Figure B-7 Aluminum test pad and 1.0" diameter cylinder.
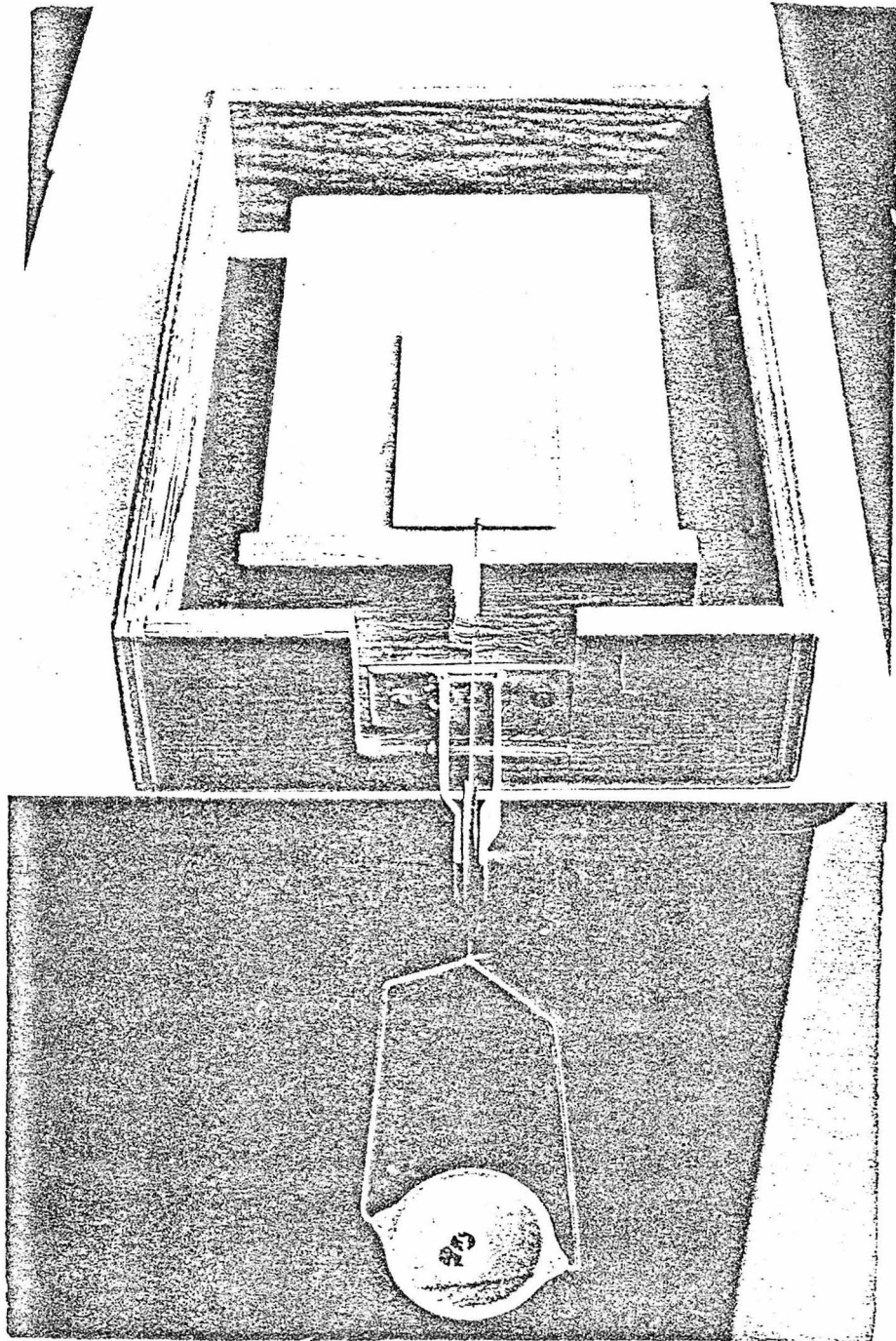
Figure B-8 Surface friction angle test apparatus.
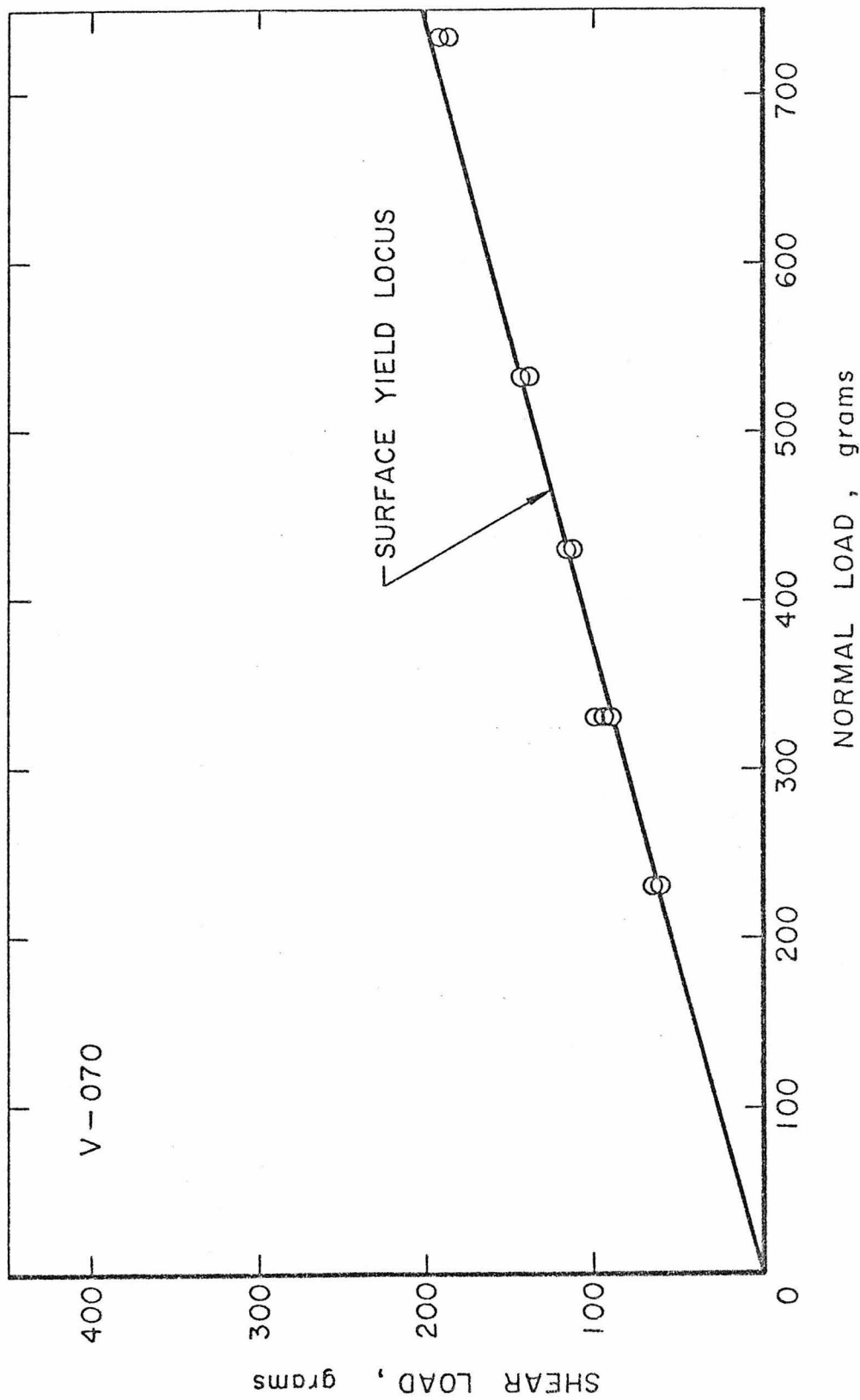
Figure B-9 Typical plot of shear load versus normal load
for surface friction angle experiment.
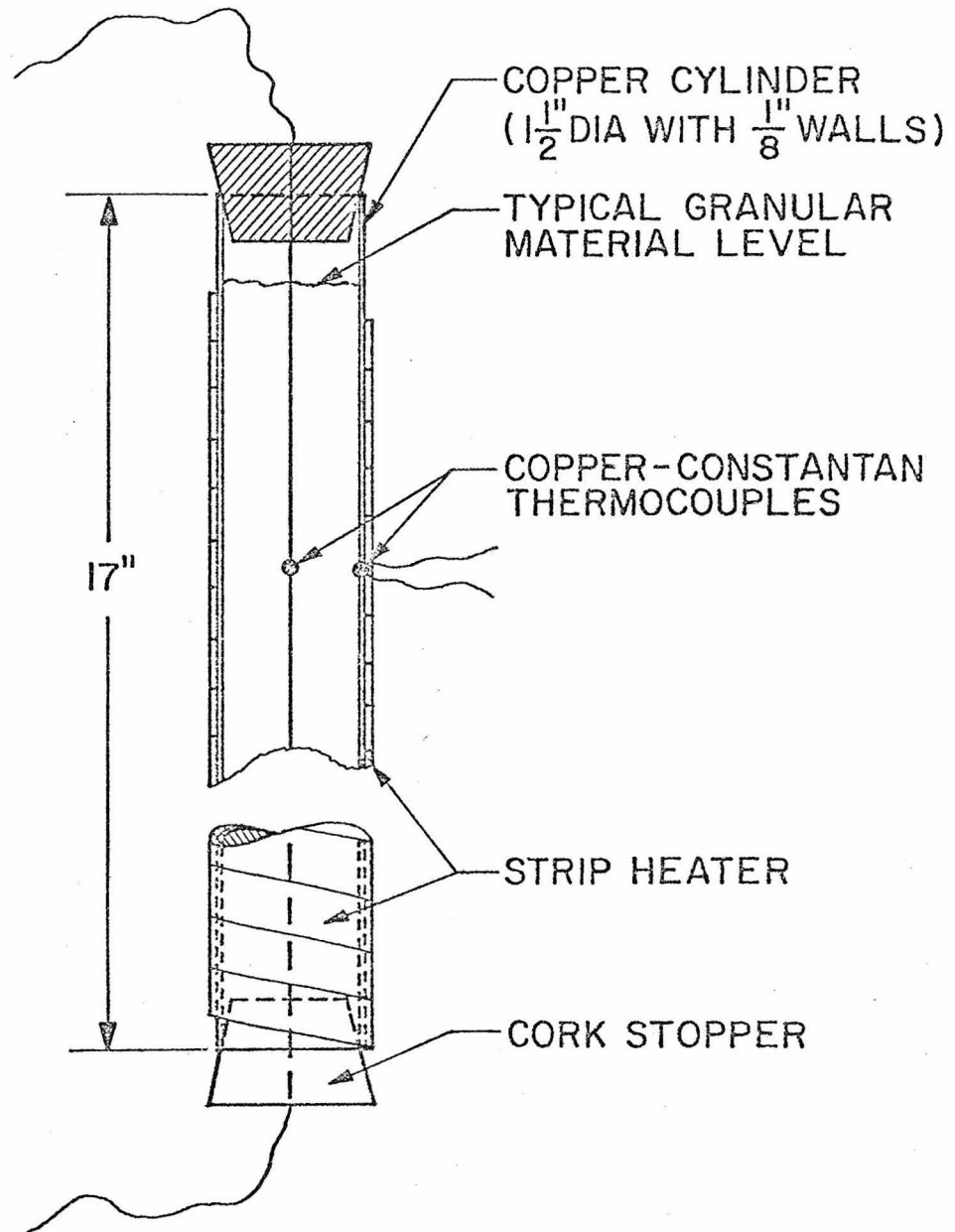
B-10 Schematic diagram of thermal diffusivity test apparatus.
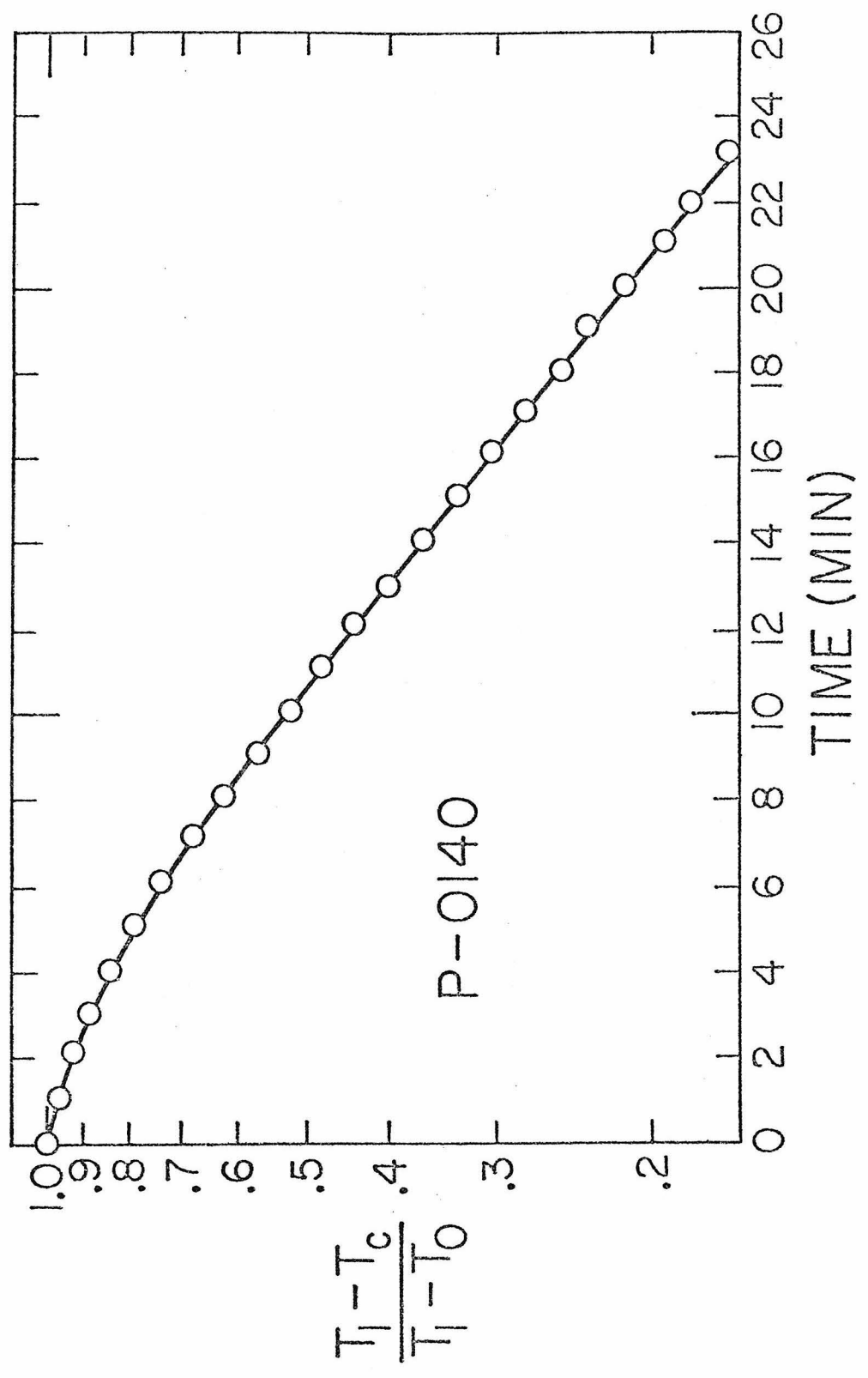
B-11 Typical plot of $\log_{10}\left(\dfrac{T_1 - T_c}{T_1 - T_0}\right)$ versus time for thermal diffusivity experiment.
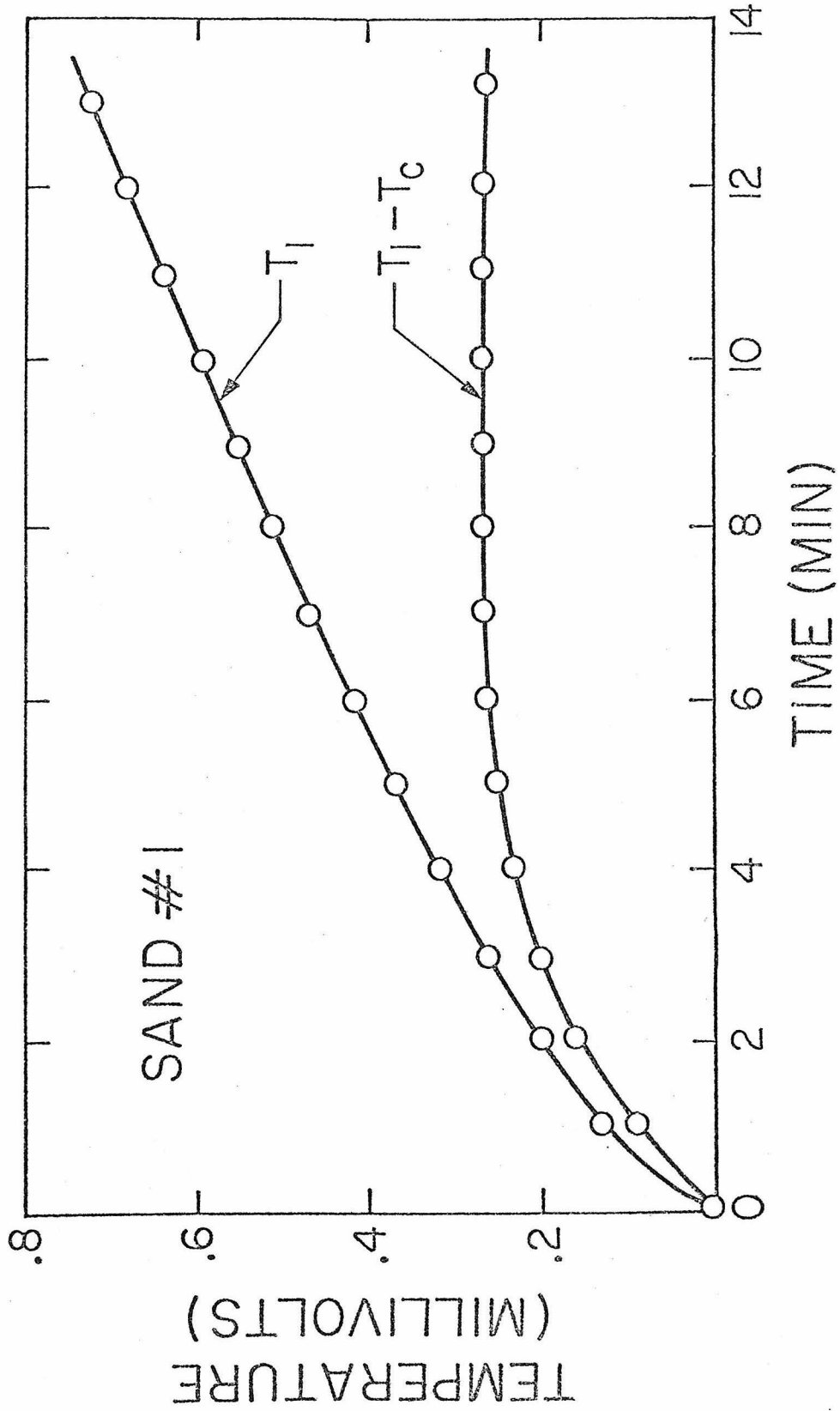
B-12 Typical plot of temperature versus time for specific heat experiment.